Parallel Design Optimization of Multi-Trailer Articulated Heavy Vehicles with Active Safety Systems

by

Md. Manjurul Islam

A thesis
presented in partial fulfillment of
the requirements for the degree of
Doctor of Philosophy
in
Mechanical Engineering

Faculty of Engineering and Applied Science
University of Ontario Institute of Technology
Oshawa, Ontario, Canada, 2013

Dedicated to

my mother Marjina Khanam and my father Md. Nurul Islam

They mean a lot to me!

Abstract

Multi-trailer articulated heavy vehicles (MTAHVs) exhibit unstable motion modes at high speeds, including jack-knifing, trailer swing, and roll-over. These unstable motion modes may lead to fatal accidents. On the other hand, these vehicle combinations have poor maneuverability at low speeds. Of all contradictory design criteria of MTAHVs, the trade-off relationship between the maneuverability at low speeds and the lateral stability at high speeds is the most important and fundamental. This trade-off relationship has not been adequately addressed. The goal of this research is to address this trade-off relationship through the design optimization of MTAHVs with active safety systems. A parallel design optimization (PDO) method is developed and applied to the design of MTAHVs with integrated active safety systems, which involve active trailer steering (ATS) control, anti-roll (AR) control, differential braking (BD) control, and a variety of combinations of these three control strategies. To derive model-based controllers, a single-trailer articulated heavy vehicle (STAHV) model with 5 degrees of freedom (DOF) and a MTAHV model with 7 DOF are generated. The vehicle models are validated with those derived using a commercial software package, TruckSim, in order to examine their applicability for the design optimization of MTAHVs with active safety systems. The PDO method is implemented to perform the concurrent design of the plant (vehicle model) and controllers. To simulate the closed-loop testing maneuvers, a driver model is developed and it is used to drive the virtual vehicle following the prescribed path. Case studies indicate that the PDO method is effective for identifying desired design variables and predicting performance envelopes in the early design stages of MTAHVs with active safety systems.

Acknowledgements

I would like to thank and offer my sincerest gratitude to my thesis supervisor, Dr. Yuping He, for his continuous support and motivation. Financial support of this research by the Natural Science and Engineering Research Council of Canada (NSERC), Canadian Foundation for Innovation (CFI) and Genist Systems Inc. (GSI) is gratefully acknowledged.

Contents

List of Figures

List of Tables

Nomenclature

β_1	tractor's side-slip angle
β_2	1st semitrailer's side-slip angle
β_3	2nd semitrailer's side-slip angle
δ_{1f}	tractor front wheel steering angle
$\dot{\psi}_1$	tractor's yaw rate
$\dot{\psi}_2$	1st semitrailer's yaw rate
$\dot{\psi}_3$	2nd semitrailer's yaw rate
ϕ_1	Roll angle of tractor's sprung mass
ϕ_2	Roll angle of 1st semitrailer's sprung mass
ϕ_2	Roll angle of 2nd semitrailer's sprung mass
ϕ_{1t}	Roll angle of tractor's unsprung mass
ϕ_{2t}	Roll angle of 1st semitrailer's unsprung mass
ϕ_{2t}	Roll angle of 2nd semitrailer's unsprung mass
a_{11}	Longitudinal distance between the tractor sprung mass CG and the front axle
a_2	Longitudinal distance between the 1st articulation joint of 1st trailer and the sprung mass CG

a_3	Longitudinal distance between the 2nd articulation joint of vehicle (articulation joint of the 2nd semitrailer) and the sprung mass CG
a_{peak1}	Maximum peak of lateral acceleration at the tractor CG under the HSLC maneuver
a_{peak2}	Minimum peak of lateral acceleration at the tractor CG under the HSLC maneuver
b_{12}	Longitudinal distance between the tractor sprung mass CG and the axle-2
b_{13}	Longitudinal distance between the tractor sprung mass CG and the axle-3
b_{24}	Longitudinal distance between the 1st semitrailer sprung mass CG and the axle-4
b_{25}	Longitudinal distance between the 1st semitrailer sprung mass CG and the axle-5
b_{26}	Longitudinal distance between the 1st semitrailer sprung mass CG and the axle-6 (MTAHV only)
b_{37}	Longitudinal distance between the 2nd semitrailer sprung mass CG and the axle-7
b_{38}	Longitudinal distance between the 2nd semitrailer sprung mass CG and the axle-8
b_{39}	Longitudinal distance between the 2nd semitrailer sprung mass CG and the axle-9
CDG_1	First cross differential gap
CDG_2	Second cross differential gap
h_{c1}	Hight of the coupling point on tractor, measured upwards from ground

h_{c2}	Hight of the (1st) coupling point on 1st semitrailer, measured upwards from ground
h_{c3}	Hight of the coupling point on 2nd semitrailer, measured upwards from ground
h_{r1}	Hight of roll center of tractor sprung mass, measured upwards from ground
h_{r2}	Hight of roll center of 1st semitrailer sprung mass, measured upwards from ground
h_{r3}	Hight of roll center of 2nd semitrailer sprung mass, measured upwards from ground
h_{rc1}	Hight of the coupling point on tractor, measured upwards from roll center of semi-trailer sprung mass
h_{rc2}	Hight of the (1st) coupling point on 1st semitrailer, measured upwards from roll center of semi-trailer sprung mass
h_{rc3}	Hight of the coupling point on 2nd semitrailer, measured upwards from roll center of semi-trailer sprung mass
h_{s1}	Hight of CG of tractor sprung mass, measured upwards from ground
h_{s2}	Hight of CG of 1st semitrailer sprung mass, measured upwards from ground
h_{s3}	Hight of CG of 2nd semitrailer sprung mass, measured upwards from ground
I_{xx1}	Roll moment of inertia of tractor sprung mass, measured from CG of the sprung mass
I_{xx2}	Roll moment of inertia of 1st semitrailer sprung mass, measured from CG of the sprung mass

I_{xx3}	Roll moment of inertia of 2nd semitrailer sprung mass, measured from CG of the sprung mass
I_{xz1}	Roll/yaw product of inertia of tractor sprung mass, measured from the CG of the sprung mass
I_{xz2}	Roll/yaw product of inertia of 1st semitrailer sprung mass, measured from the CG of the sprung mass
I_{xz3}	Roll/yaw product of inertia of 2nd semitrailer sprung mass, measured from the CG of the sprung mass
I_{zz1}	yaw moment of inertia of whole mass of the tractor
I_{zz2}	yaw moment of inertia of the 1st semitrailer
I_{zz3}	yaw moment of inertia of the 2nd semitrailer
K_{f1}	Roll stiffness of front suspension of the tractor, adjusted with the tire vertical stiffness
K_{r1}	Roll stiffness of rear suspension of the tractor, adjusted with the tire vertical stiffness
K_{r2}	Roll stiffness of rear suspension of 1st semitrailer, adjusted with tire vertical stiffness
K_{r3}	Roll stiffness of rear suspension of 2nd semitrailer, adjusted with tire vertical stiffness
l_{c1}	Longitudinal distance between the whole mass CG of the tractor and the coupling point
l_{c21}	Longitudinal distance between the whole mass CG of the 1st semitrailer and the first coupling point
l_{c22}	Longitudinal distance between the whole mass CG of the 1st semitrailer and the second coupling point

l_{c3}	Longitudinal distance between the whole mass CG of the 2nd semi-trailer and the second coupling point
m_1	Tractor's total mass
m_2	1st semitrailer's total mass
m_3	2nd semitrailer's total mass
m_{s1}	Tractor's sprung mass
m_{s2}	1st semitrailer's sprung mass
m_{s3}	2nd semitrailer's sprung mass
$PFOT$	Path-following off-tracking
R_{CDG}	Cross differential gap ratio
RWA	Rearward amplification ratio
$TROF$	Transient off-tracking
U_1	Tractor's forward speed
U_2	1st semitrailer's forward speed
U_3	2nd semitrailer's forward speed
AHV	Articulated heavy vehicle
AR	Anti-roll
ATS	Active trailer steering
CG	Center of gravity
DB	Differential braking
DOF	Degree of freedom
GA	Genetic algorithm

HSLC	High-speed lane change
LQR	Linear quadratic regulator
LSPF	Low-speed path-following
MTAHV	Multi-trailer articulated heavy vehicle
PDO	Parallel design optimization
STAHV	Single-trailer articulated heavy vehicle

CHAPTER 1

Introduction

1.1 Motivation

Multi-trailer articulated heavy vehicles (MTAHVs) with a tractor/two-trailer combination have been on the roads in Western Canada, Quebec, and more than 20 states in USA for decades. To ensure free movement of MTAHVs between Ontario and Quebec, in the summer of 2009, the Ontario Ministry of Transportation launched a pilot program to allow MTAHVs to travel on designated Ontario highways [71]. However, due to MTAHVs' large sizes and high center of gravity, they have poor maneuverability and low stability. Canada's long and severe winter weather patterns further degrade MTAHVs's safety. Vehicle safety affects all Canadians. In 2004, a total of 2,730 people were killed in road crashes and 212,347 were injured where mostly the articulated heavy vehicles are involved [70].

With more than 1,300 automotive companies, Canada has achieved the position of sixth largest exporter of road motor vehicles in the world. The country has become a global automotive center with the annual revenues of $71 billion from the automotive industry [3]. However, Canada's automotive industry is continuously experiencing challenges with intensive global competition. In 2001, Canada ranked fifth in global vehicle production, but it slipped to eighth place in 2004. To strengthen this position, development of new vehicle safety technologies and, in particular, the design of innovative active safety systems for MTAHVs is critical.

It becomes apparent that the impact of this thesis will be multifold. This thesis will contribute to increasing safety of MTAHVs, and thereby, to increase the usage of such vehicles and eventually, to achieve higher cost-effectiveness and lower greenhouse gas emissions.

1.2 Design problem

An MTAHV consists of a powered unit, namely truck or tractor, and towed unit(s), called trailer(s). Individual units are connected to one another at articulated points by mechanical couplings, including pintle hitches, dollies, and 5th wheels. Due to MTAHVs' complex configurations and large sizes, they have poor low-speed directional performance (maneuverability) [24]. In the Australian performance-based standards (PBS) for articulated heavy vehicles, the low-speed maneuverability performance measures, including swept path, frontal swing, and tail swing, are specified [19]. The MTAHVs' poor maneuverability raises safety concerns for traffic and the damage of road infrastructure [38]. To effectively represent these low-speed performance measures, a unified measure, called path-following off-tracking (PFOT), is utilized in this thesis. The PFOT is defined as the maximum radial offset between the trajectory of the tractor's front axle center and that of the (usually, rearmost) trailer's rear axle center during the low-speed 360-degree roundabout testing maneuvers defined in the United Kingdom's Road Vehicle Regulation [51] or the 90-degree intersection turn testing procedure [9, 24]. An MTAHV with good low-speed maneuverability should have a low PFOT value [5, 32, 42, 44–47].

On the other hand, MTAHVs exhibit unstable motion modes at high speeds, including jack-knifing, trailer swing, and roll-over [21, 41, 43, 49, 86]. These unstable modes may lead to fatal accidents [23]. To ensure acceptable lateral stability level, the PBS also specifies high-speed directional performance measures, involving static roll-over threshold, rearward amplification (RWA) ratio, and yaw damping coefficient [19]. The RWA ratio is defined as the ratio of the peak lateral accel-

eration at the rearmost trailer's center of gravity (CG) to that of the towing unit in an obstacle avoidance lane-change maneuver [24]. Generally, an articulated heavy vehicle (AHV), including a MTAHV, has the tendency for the rearmost trailer to have a higher maximum lateral acceleration than that of the towing unit in quick, evasive maneuvers [22, 72]. Articulated heavy vehicles are quite susceptible to roll-over of the rearmost trailers during highway emergency maneuvering [16, 37, 83]. The maximum RWA ratio accepted by the PBS is tied to the static roll-over threshold [10, 17, 26, 27, 58, 76]. Roll stability is highly dependent on the RWA ratio [21]. The yaw damping coefficient [1, 2] has significant effects on the rearmost trailer swing and the articulation angles between adjacent units of an MTAHV. If the articulation angle exceeds a critical threshold, the jack-knifing phenomenon occurs [14, 63]. This yaw damping coefficient is also related to the RWA ratio. It is commonly accepted that lower values of RWA ratio imply higher lateral stability at high-speeds [51, 75]. In the Australian PBS, the RWA ratio is determined through the single lane-change test maneuver specified in ISO 14791 and SAE J2179 [24, 51].

Of all contradictory design criteria of MTAHVs, the low-speed maneuverability and the high-speed lateral stability are the most fundamental and important [52, 89]. To date, this trade-off has not been adequately addressed. To address the low maneuverability problem at low-speeds, several *passive* trailer steering systems have been developed. These systems improve low-speed performance, but exhibit low stability at high speeds. On the other hand, some active trailer steering (ATS) [15, 54], differential braking (DB) [29], and anit-roll (AR) [18, 81] controls individually have been proposed to improve high-speed stability. However, these systems typically degrade maneuverability when applied at low speeds. This phenomenon matches a rule-of-thumb observation pertaining to the trade-off relationship between MTAHVs' low-speed maneuverability and high-speed stability: *what one does to improve low-speed performance is likely to degrade high-speed performance and vice versa* [24].

1.3 Objectives

To date, there is no systematic design synthesis approach to address the trade-off relationship between the conflicting requirements. To tackle this complex design problem, the thesis will focus on some innovative investigations.

The primary objective of this thesis is to develop an integrated design method for multi-trailer articulated heavy vehicles (MTAHVs) with active safety technologies. A parallel design optimization (PDO) method is to be developed and implemented for the design of MTAHVs with integrated control systems. Different control techniques will be investigated, including active trailer steering (ATS), differential braking (DB), and anti-roll (AR) control, and different combinations of the three. To consider the closed-loop dynamic feature of MTAHVs' realistic operations, the design method incorporates the modeling and simulation of vehicles' subsystems, including the mechanical vehicle assembles, driver, integrated controllers, and typical test maneuvers.

1.4 Methodologies

The framework of the methodology consists of the following main components: development of a multiple degree-of-freedom (DOF) MTAHV model to derive model-based controllers; validation of the multiple DOF vehicle models with a commercial software package TruckSim; generation of a driver model which will be used to *drive* the virtual vehicle tracking the prescribed path to simulate the closed-loop testing maneuvers; investigation of different control techniques; application of a parallel design optimization (PDO) method to perform the concurrent design of the plant (vehicle model) and controllers.

The following control strategies are to be studied to improve both high-speed stability and low-speed maneuverability: active trailer steering (ATS); differential braking (DB) control; anti-roll (AR) control; integrated ATS and DB; integrated

DB and AR; integrated AR and ATS; integrated ATS, DB and AR control. The proposed design methods has been applied in design to the STAHV with a tractor and a single semitrailer combination, and a MTAHV with tractor and two semitrailers (B-train Double) combination.

1.5 Expected Value of the Thesis

The research reported in this thesis is closely related to the automotive industry and market requirements: the new vehicles must be greener and safer in order to be accepted by the modern consumer. MTAHVs with active safety systems provide both features: by using less fuel to carry goods, MTAHVs reduce the greenhouse gas emissions by about one-third. The thesis will lead to the following accomplishments:

1.5.1 A systematic design method

It is expected that the proposed design method can be used for identifying the desired design variables and predicting optimal performance envelopes in the early design stages of MTAHVs with active safety systems. This design tool will provide MTAHV manufacturers with the following advantages: flexibility for parameter study, cost efficiency, development time reduction, and safety.

1.5.2 An innovative integrated control

The active vehicle system will effectively improve low-speed maneuverability and high-speed stability of MTAHVs. The integrated control systems derived from the proposed design method will have optimal performance, reducing system complexity and costs by avoiding unnecessary duplication of components and sharing information between sensors.

It is expected that the thesis has developed valuable techniques and guidances

that MTAHV manufacturers can use to design, test and validate their designs for improving vehicle safety.

1.6 Thesis Organization

The thesis is organized as follows. In Chapter 2, a literature review on the articulated heavy vehicles has been offered; Chapter 3 describes the modeling of the AHVs to be designed, in this thesis, including a 3 degree of freedom (DOF) yaw plane model and 5 DOF yaw/roll model of a tractor/semitrailer combination, and a 5 DOF yaw plane model and a 7 DOF yaw/roll model of tractor/two semitrailer (B-train Double) combination; in Chapter 4, extensive validation of the linear vehicle models, introduced in Chapter 3, is presented; Chapter 5 presents a developed driver model to *drive* the vehicle in the prescribed path during the simulation and corresponding validations; in Chapter 6, various control strategies, including active trailer steering (ATS), differential braking (DB), anti-roll (AR), and their combinations are presented for an AHV with a tractor/semitrailer and a MTAHV with tractor/two-semitrailers combination; Chapter 7 demonstrates the proposed parallel design optimization (PDO) method for the MTAHV with active safety systems; in Chapter 8, the high performance computing systems is introduced and a system performance analysis will be presented; the proposed PDO is implemented to design a tractor/semitrailer combination with active safety systems in Chapter A; the proposed method is utilized, in Chapter 10, to design a MTAHV with a tractor/two semitrailer (B-train Double) combination with active safety systems; finally Chapter 11 presents the conclusions drawn from the research and also provides some important future recommendations.

CHAPTER 2

Literature Review

2.1 Introduction

To address the problem of articulated heavy vehicles' (AHVs) large path-following offtracking (PFOT), several passive trailer steering systems, including self-steering axles, have been developed. A number of active trailer steering (ATS) systems have also been proposed for attenuating the problem. It is found that these passive and active trailer steering systems can decrease the low-speed PFOT. However, the high-speed rearward amplification (RWA) ratio of the corresponding AHV is inherently high.

2.2 Articulated Heavy Vehicles and their Models

Articulated heavy vehicles (AHVs) can be classified into two general categories: (i) tractor and single trailer combinations, namely, single trailer articulated heavy vehicles (STAHVs) and (ii) tractor and multi-trailer combinations, called multi-trailer articulated heavy vehicles (MTAHVs). In Canada, the MTAHVs with two trailers combinations are named as long combination vehicles (LCVs), if the overall vehicle length of the combinations exceed 25 meters [85]. The LCV can be further classified into three groups, namely, Rocky Mountain Double (a tractor, a 12.2-16.2 m semi-trailer, and a shorter 7.3-8.5 m semitrailer combination), Turnpike Double (a tractor

with two equal length semitrailers, of each 12.2 to 16.2 m long, combination), and Triple Trailer Combination (a tractor with three equal length, approximately 12.2-16.2 meters, semitrailers combination).

All these vehicles are often responsible for severe highway accidents, causing life and many economic losses. It is very important to design the control systems for the vehicle to improve safety and handling of these vehicles. The high centers of gravity and their complex configurations make the dynamic behaviors of these AHVs very difficult for a designer to predict. Computer modeling and simulation provides an effective approach to the design optimization of MTAHVs with active safety systems. The computer simulations and controller designing for these vehicles require vehicle modeling. The AHV system is highly nonlinear; the more complex and nonlinear the mathematical model is, the closer the dynamics of the model to the real systems becomes. However, if the model is simpler, for example, as in a linear state-space form, it becomes easier for the designer to design the controller. But the necessary precaution should be made to ensure that the important dynamic features are not lost.

A highly nonlinear vehicle model with many degrees of freedom can be generated using commercial multibody software packages, namely, CarSim, TruckSim, ADAMS, DADS, etc. These models are comprehensive, reliable, and are able to predict actual dynamics very closely. Automotive manufactures and many other users are very interested in these models due to the inclusion of many moving parts [56]. One of the most important benefit is that the users, especially development engineers in industries, can fine-tune the component level details of the design [84].

2.3 Active Safety Systems

The low speed path-following off-tracking (PFOT) measure is shown in Figure 2.1. An example of rollover unstable motion mode, due to higher value of RWA ratio,

of an AHV in a sudden single lane change maneuver at high speeds is presented in Figure 2.2. To improve the compatibility between the low-speed PFOT value and the high-speed RWA ratio, researchers have investigated a variety of potential solutions. It is reported that the location of steerable axles and the types of steering mechanism have significant effects on the dynamic stability of a tractor/trailer systems [8]. The RWA ratio has been used as a control criterion in the design of active yaw controllers for a tractor/full-trailer combination [21]. Compared with the baseline vehicle, the one with the active trailer yaw controller can reduce the RWA ratio without significant change of the baseline vehicle's PFOT at low speeds. Recently, the linear quadratic regulator (LQR) technique has been applied to the controller design of ATS systems for AHVs [77, 78]. The researchers intended to identify the correlation between the RWA ratio and the PFOT value in order to reduce the latter through minimizing the former. Another solution accepted to date is to use a passive and an active trailer steering system alternatively [8, 67, 78]. At low speeds, the passive steering systems are employed in order to effectively decrease PFOT values. From medium to high speeds, ATS systems are applied to ensure that AHVs have high stability. This solution provides a good way to coordinate the conflicting design criteria at low and high speeds, but it increases the complexity of trailer configurations since the *dual* steering systems co-exist.

Few studies also report that the differential braking (DB) technique improves the high-speeds stability of MTAHVs [21, 25]. The anti-roll (AR) control systems consisting of anti-roll bars also improve dynamic behavior at high-speeds[13, 62, 82]. However, these active systems usually degrade the MTAHVs' maneuverability in low-speed cases. Hence, designers frequently face difficulties to find suitable control techniques for simultaneously improving both the low-speed and the high-speed performance measures MTAHVs. Some other studies strongly support that, for a single unit vehicle, integration of different control strategies shows drastic improvement of both maneuverability and stability [12, 30, 50, 53, 61]. However, no such integrated control system has been investigated in designing MTAHVs.

Past studies mainly focused on investigating the effects of key design variables

and influence of either passive [57] or active trailer steering systems [16, 67, 77] on the contradictory design goals based on dynamic simulation and analysis. This is a *trial-and-error* approach, where designers iteratively change the values of design variables and reanalyze until acceptable performance criteria are achieved. For example, in the LQR controller design for ATS systems, this approach is commonly used to determine desired weighting factors for the cost function. This manual design process is tedious and time-consuming. With the stringent conflicting performance requirements, the design of AHVs should switch from pure simulation analysis to extensive design synthesis. In the conventional dynamic analysis of AHVs with ATS systems, it is commonly assumed that the passive system is designed first and then the ATS systems developed are added onto the vehicle originally designed from a purely mechanical viewpoint. The resultant design based on this sequential method may be less *optimally* overall due to the mechanical and control parameters not being simultaneously considered as design variables [34].

To tackle the design synthesis of AHVs with ATS systems, He et al. have recommended a method in which the optimal active and passive design variables are identified in two design loops (TDL) [34]. In the first design loop, with all the passive system parameters taking their nominal values, the weighting factors of the LQR controller's cost function for the ATS system is automatically identified using an optimization technique. Then, with the weighting factors obtained, the optimal passive design variables and the LQR control gain matrices for the ATS system are determined in the second design loop. The ATS controller resulting from this approach has two operational modes, one for improving stability at high speeds and the other for enhancing maneuverability at low speeds. In this two design loop (TDL) method, the weighting factors of the LQR controller's cost function for the ATS system and the passive trailer design variables are optimized in two independent design optimization loops. Thus, the TDL method cannot adequately address the interactions among the passive and active design variables. The TDL method is based on the open-loop dynamic simulations to emulate both the low- and high-speed test measures:

1. to determine the low-speed PFOT value, the 360-degree roundabout path-

following test maneuver specified in the United Kingdom's Road Vehicle Regulation is emulated with a predefined step steer input for the truck (or tractor) [51]; and

2. to determine the high-speed RWA ratio, a single lane-change test maneuver is simulated with a prescribed single sinusoidal wave steer input for the truck (or tractor).

Numerous numerical experiments indicate that open-loop dynamic simulations have difficulty emulating to emulate the well-defined test maneuvers, such as the single lane-change maneuver defined by SAE J2179 [68] or ISO 14791 [69] for evaluating the RWA ratio, with high fidelity [34]. In order to evaluate and validate an AHVs' directional performance and the corresponding ATS functions, it is essential to have a driver model [31, 55, 60, 64, 73, 74, 79, 80, 90] that can *drive* a virtual AHV to follow a prescribed route at a given speed without predefined steering inputs. In the closed-loop dynamic simulation, the driver model functions as a *virtual test driver* [74].

2.4 Objectives of the Proposed Research

Built upon the TDL method, in this thesis, a parallel design optimization (PDO) approach based on closed-loop dynamic simulations will be proposed and implemented to design a STAHV and a MTAHV. This new method has the following distinguished features: all the optimal active design variables of the active systems including active trailer steering (ATS), differential braking (DB), and anti-roll (AR) control and the optimal passive design variables of the trailer are determined in a single design loop; in the design process, to evaluate the vehicle performance measures, a driver model is introduced and it *drives* the vehicle model based on the well-defined testing specifications.

The vehicle models for a STAHV and the corresponding control strategies developed will be extended and improved for the design of MTAHVs with integrated

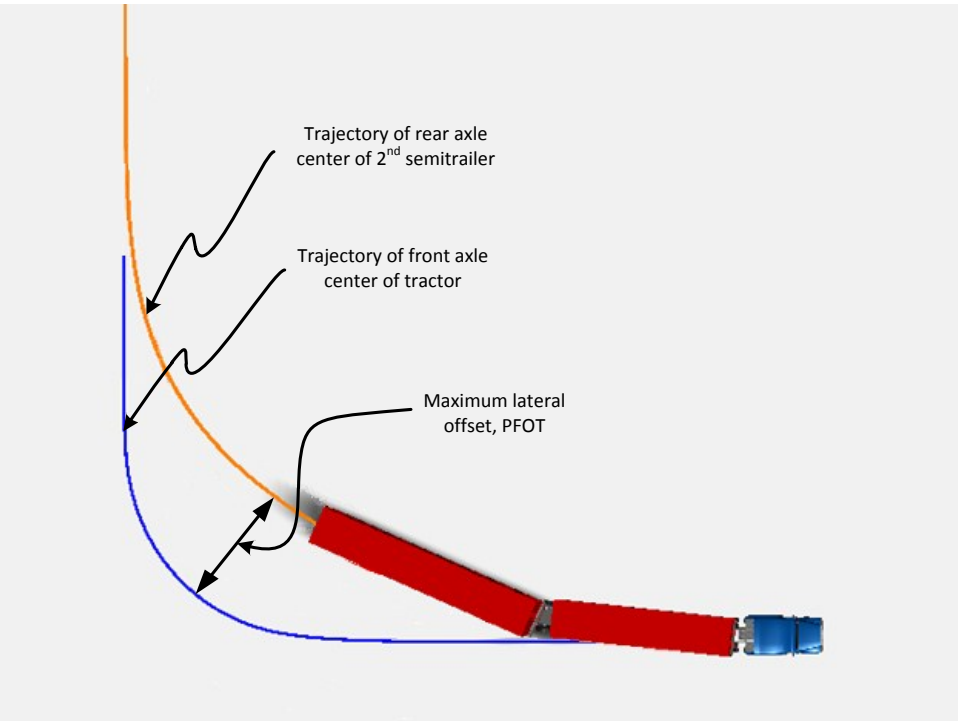

Figure 2.1: The path-following off-tracking: maximum lateral offset between the path of the center of the tractor's steering axle and that of rearmost trailer's rear axle

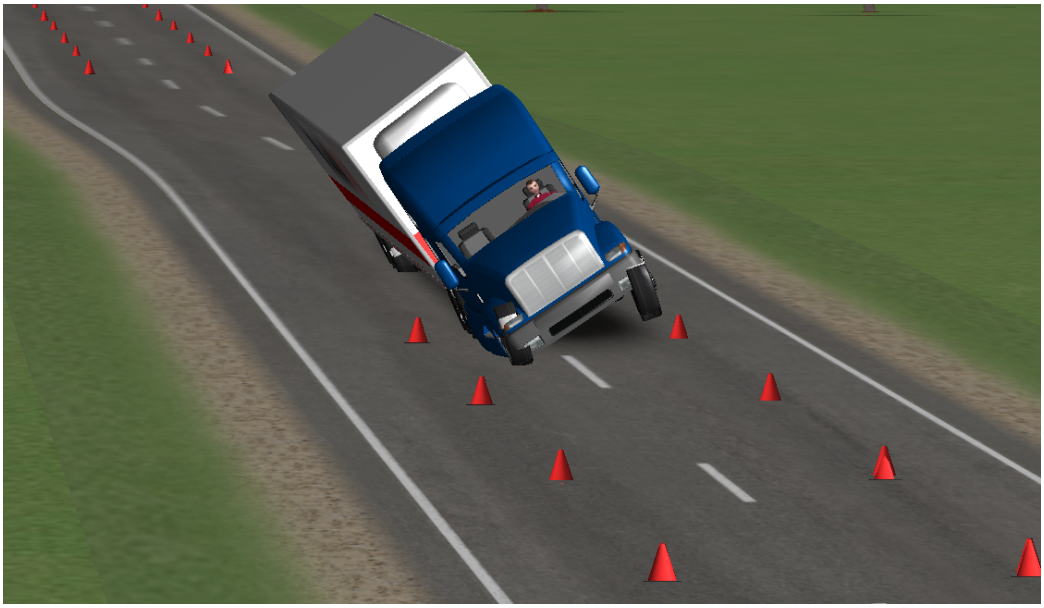

Figure 2.2: An example of an AHV rollover during a single lane change of a tractor and semitrailer combination

control systems. In this thesis, two vehicle combinations of AHVs are chosen: one is a tractor and a semitrailer combination, and the other is a tractor and two semitrailers combination. The 3 degree of freedom (DOF) linear yaw model and the 5 DOF 3D linear yaw-roll model are generated for the STAHV. The other AHV, considered in this research, is a MTAHV with both trailers having equal length of wheelbase. For the MTAHV, a 4 DOF linear yaw model and a 7 DOF linear yaw-roll model are generated.

Generally, a linear model is used to design the controller and the simulation has been performed of a nonlinear vehicle model coupled with the designed controller to estimate the behavior of the controlled vehicle. For automated design synthesis of these vehicles, multidisciplinary design optimization technique involves numerous computer simulations. Compared to the linear model, the nonlinear model is more complicated to design and costs longer computation time [84]. The optimization of such a nonlinear model could be highly time consuming even with a high-performance computing systems [40, 46]. Hence, for design optimization, it is more beneficial to utilize the linear models of the plant instead of nonlinear

models. It is possible to well-represent the dynamic behaviors of such vehicles with simplified lower DOF model [6].

In this research, a validation of the linear models for the two vehicle combinations using highly nonlinear models generated using TruckSim, a commercial software package, is performed. It is expected that the validated models can be utilized for the parallel design optimization (PDO) of active safety systems where extensive numerical simulations [33, 34, 39] are needed to be performed. Previous studies claim that the lateral tire forces are in linear region if the lateral acceleration is below 0.3 g in any specified maneuver [4, 87, 88]. That is, it is suitable to use a linear model for a simulation of the high-speed maneuvers, such as SAE [68] or ISO [69] lane change, if the lateral acceleration does not exceed 0.3 g.

During low-speed turn maneuvers, the tire lateral slip angles also stay within the linear region. The widely used low-speed turn maneuvers are 90-degree intersection turn and 360-degree roundabout turn maneuvers. This thesis also presents an eigenvalue analysis of the models to indicate the unstable motion modes. From the state-space form of linear equations of motion, the resistance of the heavy articulated vehicles to disturbances can be indicated in straight-line driving with low levels of lateral acceleration [54]. This analysis also determines the decay or growth rate of free response which eventually indicates how the vehicle responses with the disturbance.

2.5 Summary

This chapter describes a review of the state-of-the-art related to design synthesis of MTAHV with active safety systems. From the review of the literatures, it is evident that the introduction of a systematic design optimization method using a high performance computing system can facilitate the design synthesis process of MTAHV and ensure improved trade-off performances at high and low speeds.

CHAPTER 3

Linear AHV Models

3.1 Introduction

In this chapter, the vehicle models of an STAHV with a tractor and single semitrailer combination and a MTAHV with a tractor and two semitrailers (B-train Double) combination are presented. A linear 3 degree-of-fredom (DOF) yaw-plane model, a linear 5 DOF yaw-roll model, and corresponding TruckSim model of tractor/semitrailer are to be introduced; and a linear 4 DOF yaw-plane model, a linear 7 DOF yaw-roll model, and the respective TruckSim model of B-train Double longer combination vehicle (LCV) will be described. The yaw-roll models of both vehicles, to be introduced in this chapter, are installed with relevant active components of active trailer steering (ATS), differential braking (DB), and anti-roll (AR) systems.

In summary, this chapter describes the following six AHV models: models for a tractor/semitrailer combination, namely, 1) a linear 3 DOF yaw plane model, 2) a linear 5 DOF yaw/roll model, and 3) a nonlinear TruckSim model; and models for a B-train Double LCV, namely, 4) a linear 4 DOF yaw plane model, 5) a linear 7 DOF yaw/roll model, and 6) a nonlinear TruckSim model.

3.2 STAHV Modeling

The STAHV to be designed in this thesis consists of a tractor and a semitrailer, which are connected by a 5th wheel. As shown in figure 3.1, each axle is represented by a single wheel. Based on the body fixed coordinate systems, $x_1 - y_1 - z_1$ and $x_2 - y_2 - z_2$, for the tractor and semitrailer, respectively, the governing equations of motion can be derived.

In the vehicle modeling, it is assumed that the forward speed U_1 of the vehicle and the tractor front wheel steering angle δ_{1f} are given. The pitch or bounce motion of both the tractor and semitrailer, braking forces, and aerodynamic forces are ignored. The tire model used is a linear model that specifies the linear relationship between the tire lateral force and tire side-slip angle. The articulation angle between the tractor and the semitrailer is assumed to be small. The roll stiffness and damping coefficients of the vehicle suspension systems are constant in the case of roll motions involved. The motions considered in the 5 DOF yaw/roll model are tractor side-slip angle β_1, tractor yaw rate $\dot{\psi}_1$ and roll angle ϕ_1, and semitrailer yaw rate $\dot{\psi}_2$ and roll angle ϕ_2. From Newton's law of dynamics, the equations of motion for the tractor and semitrailer can be derived.

3.2.1 Linear 5 DOF Yaw-Roll Model

The STAHV with a tractor/semitrailer combination is represented by Model-1. The equations of motion of the tractor, governed by Newton's second law, are shown

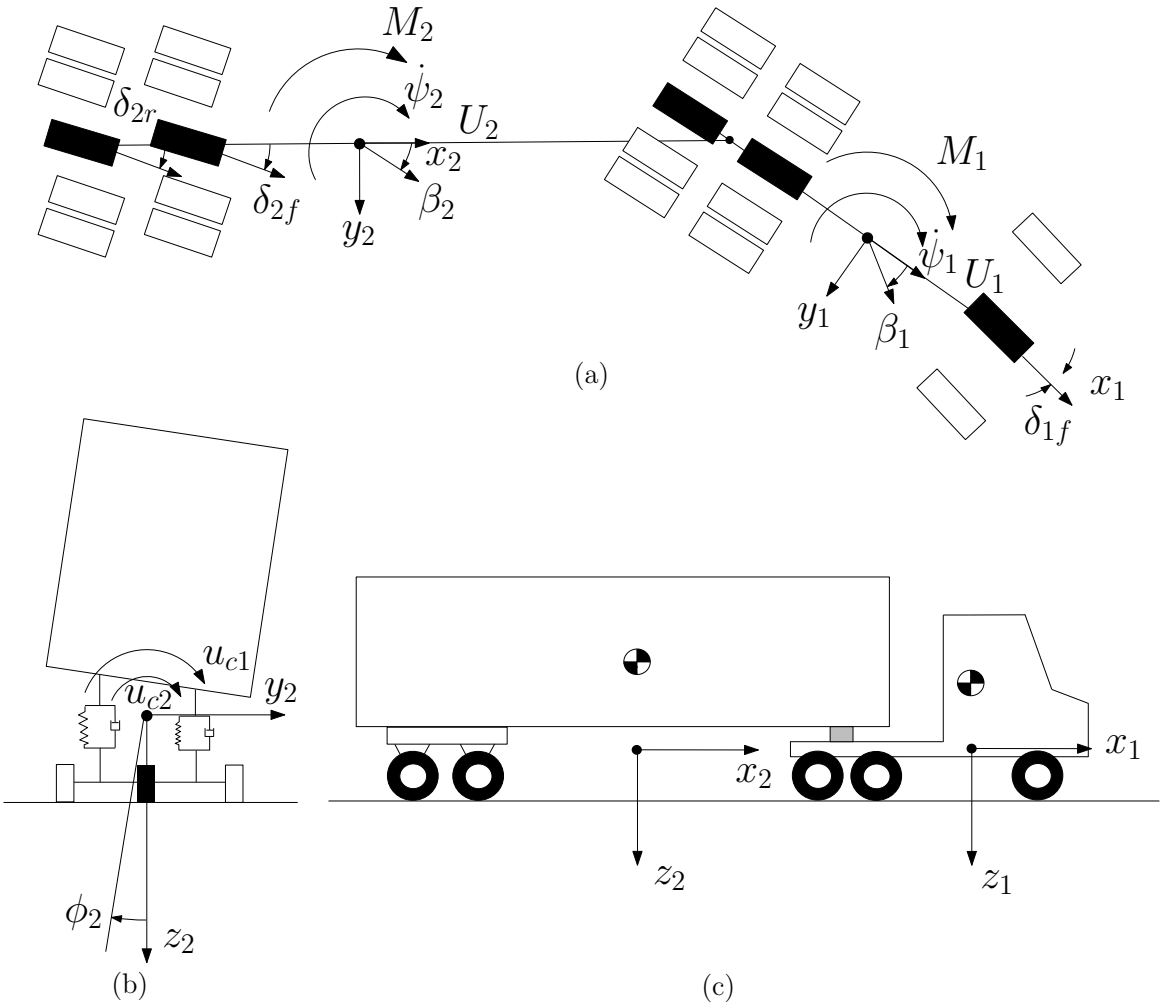

Figure 3.1: The 5 DOF yaw/roll model: (a) top view, (b) rear view, and (c) side view

as

$$m_1 U_1 \left(\dot{\beta}_1 + \dot{\psi}_1\right) - m_{s1}\left(h_{s1} - h_{r1}\right)\ddot{\phi}_1 = Y_{\beta_1}\beta_1 + Y_{\dot{\psi}_1}\dot{\psi}_1 + Y_{\delta 1f}\delta_{1f} + F_{y1} \tag{3.2.1a}$$

$$-I_{xz1}\ddot{\phi}_1 + I_{zz1}\ddot{\psi}_1 = N_{\beta 1}\beta_1 + N_{\dot{\psi}_1}\dot{\psi}_1 + N_{\delta 1f}\delta_{1f} - l_{c1}F_{y1} \tag{3.2.1b}$$

$$\begin{aligned} I_{xx1}\dot{\phi}_1 + m_{s1}\left(h_{s1} - h_{r1}\right)^2\dot{\phi}_1 - I_{xz1}\ddot{\psi}_1 &= m_{s1}g\left(h_{s1} - h_{r1}\right)\phi_1 \\ &+ m_{s1}U_1\left(h_{s1} - h_{r1}\right)\left(\dot{\beta}_1 + \dot{\psi}_1\right) - m_{s1}\left(h_{s1} - h_{r1}\right)^2\ddot{\phi}_1 - \left(K_{f1} + K_{r1}\right)\left(\phi_1 - \phi_{t1}\right) \\ &- \left(L_{f1} + L_{r1}\right)\left(\dot{\phi}_1 - \dot{\phi}_{t1}\right) + K_{12}\left(\phi_2 - \phi_1\right) - F_{y1}h_{cr1} + u_{c1} \end{aligned} \tag{3.2.1c}$$

$$\begin{aligned} \left(L_{f1} + L_{r1}\right)\dot{\phi}_1 - \left(L_{f1} + L_{r1}\right)\dot{\phi}_{t1} + \left(K_{f1} + K_{r1}\right)\phi_1 \\ - \left(K_{f1}K_{tr1} + K_{r1} + K_{tf1}\right)\phi_{t1} = u_{c1} \end{aligned} \tag{3.2.1d}$$

and the equations of motion for the semitrailer are cast as

$$\begin{aligned} m_2 U_2\left(\dot{\beta}_2 + \dot{\psi}_2\right) - m_{s2}\left(h_{s2} - h_{r2}\right)\ddot{\phi}_2 &= Y_{\beta_2}\beta_2 + Y_{\dot{\psi}_2}\dot{\psi}_2 + Y_{\delta 2f}\delta_{2f} \\ &+ Y_{\delta 2r}\delta_{2r} - F_{y1} \end{aligned} \tag{3.2.2a}$$

$$\begin{aligned} -I_{xz2}\ddot{\phi}_2 + I_{zz2}\ddot{\psi}_2 &= N_{\beta 2}\beta_2 + N_{\dot{\psi}_2}\dot{\psi}_2 + N_{\delta 2f}\delta_{2f} \\ &+ N_{\delta 2r}\delta_{2r} - l_{c2}F_{y1} + M_2 \end{aligned} \tag{3.2.2b}$$

$$\begin{aligned} I_{xx2}\dot{\phi}_2 + m_{s2}\left(h_{s2} - h_{r2}\right)^2\dot{\phi}_2 - I_{xz2}\ddot{\psi}_2 &= m_{s2}g\left(h_{s2} - h_{r2}\right)\phi_2 \\ &+ m_{s2}U_2\left(h_{s2} - h_{r2}\right)\left(\dot{\beta}_2 + \dot{\psi}_2\right) - m_{s2}\left(h_{s2} - h_{r2}\right)^2\ddot{\phi}_2 - K_{r2}\left(\phi_2 - \phi_{t2}\right) \\ &- L_{r2}\left(\dot{\phi}_2 - \dot{\phi}_{t2}\right) + K_{12}\left(\phi_2 - \phi_1\right) - F_{y1}h_{cr2} + u_{c2} \end{aligned} \tag{3.2.2c}$$

$$L_{r2}\dot{\phi}_1 - L_{r1}\dot{\phi_{t2}} + K_{r2}\phi_2 - \left(K_{r2} + K_{tf2}\right)\phi_{t1} = u_{c2} \tag{3.2.2d}$$

The velocities of the 5th wheel described in either of the coordinate systems should be comparable. Eliminating the reaction force F_{y1}, from the equations motion of both the tractor and the semitrailer leads to the linear 5 DOF model expressed in the following state-space form

$$\dot{\mathbf{x}} = \mathbf{A}\mathbf{x} + \mathbf{B}_\mathbf{u}\mathbf{u} + \mathbf{B}\delta_{1f} \tag{3.2.3}$$

where, system matrices $\mathbf{A}$ and $\mathbf{B}$ are described in Appendix. The system matrix $\mathbf{B}_\mathbf{u}$ and control variables $\mathbf{u}$ are described in Chapter 6; and the state variables $\mathbf{x}$ can be

expressed as

$$\mathbf{x} = \begin{bmatrix} \phi_1 & \dot{\phi}_1 & \beta_1 & \dot{\psi}_1 & \phi_2 & \dot{\phi}_2 & \beta_2 & \dot{\psi}_2 & \phi_{1t} & \phi_{2t} \end{bmatrix}^T, \tag{3.2.4}$$

3.2.2 Linear Yaw-Plane Model with 3 DOF

For the linear yaw-plane model with 3 DOF (hereafter called 3 DOF model), the roll motion is neglected. All the other assumptions of the 5 DOF model are valid for this linear model. The governing equations of motion can be generated if equations (3.2.1c) and (3.2.1d) for the tractor and equations (3.2.2c) and (3.2.2d) for the semitrailer are neglected.

3.2.3 Nonlinear TruckSim Model of the Tractor/Semitrailer Combination

In this research, to validate the 3 DOF and 5 DOF models, a nonlinear model of the tractor/semitrailer combination with multiple DOF is generated. In this model the motions are considered as follows. Each of the sprung masses is considered as a rigid body with five DOF, namely lateral, vertical, pitch, roll and yaw. The forward velocity of the tractor is assumed to remain constant under any maneuverer. Thus, the longitudinal DOF is not included. The fifth wheel is modeled as a ball-joint, about which roll, yaw, and pitch motions are allowed. Each axle is treated as a beam axle that can roll and bounce with respect to the sprung mass to which it is attached.

3.3 MTAHV Modeling

The MTAVH to be designed consists of a tractor and two semitrailers and the adjacent units are connected by the respective 5th wheel. The 7 DOF yaw-roll model is generated to represent the MTAVH. As shown in Figure 3.2, each axle is represented by a single wheel. Based on the body fixed coordinate systems, i.e.,

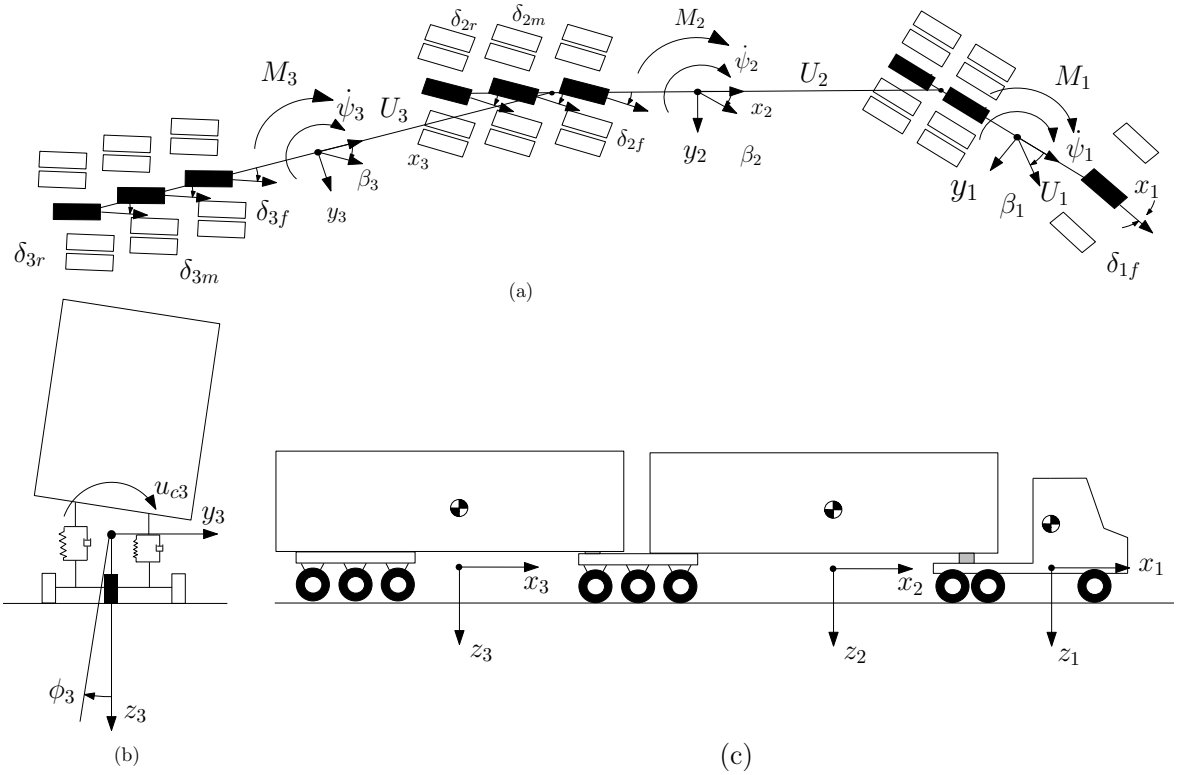

Figure 3.2: The 7 DOF yaw-roll model: (a) top view, (b) rear view, and (c) side view

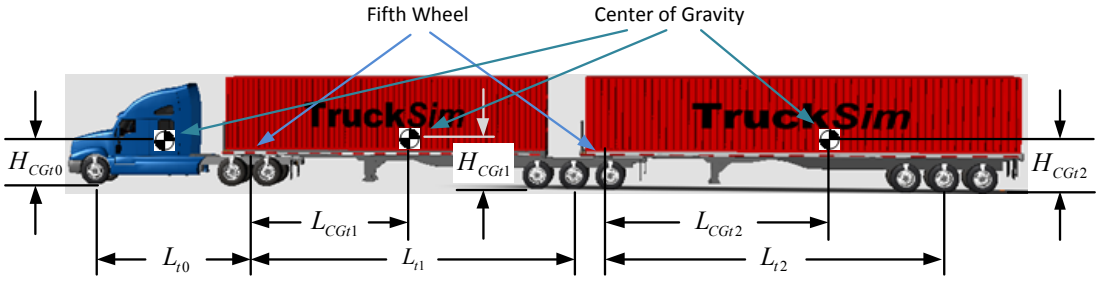

Figure 3.3: Configuration and dimensions of the MTAHV

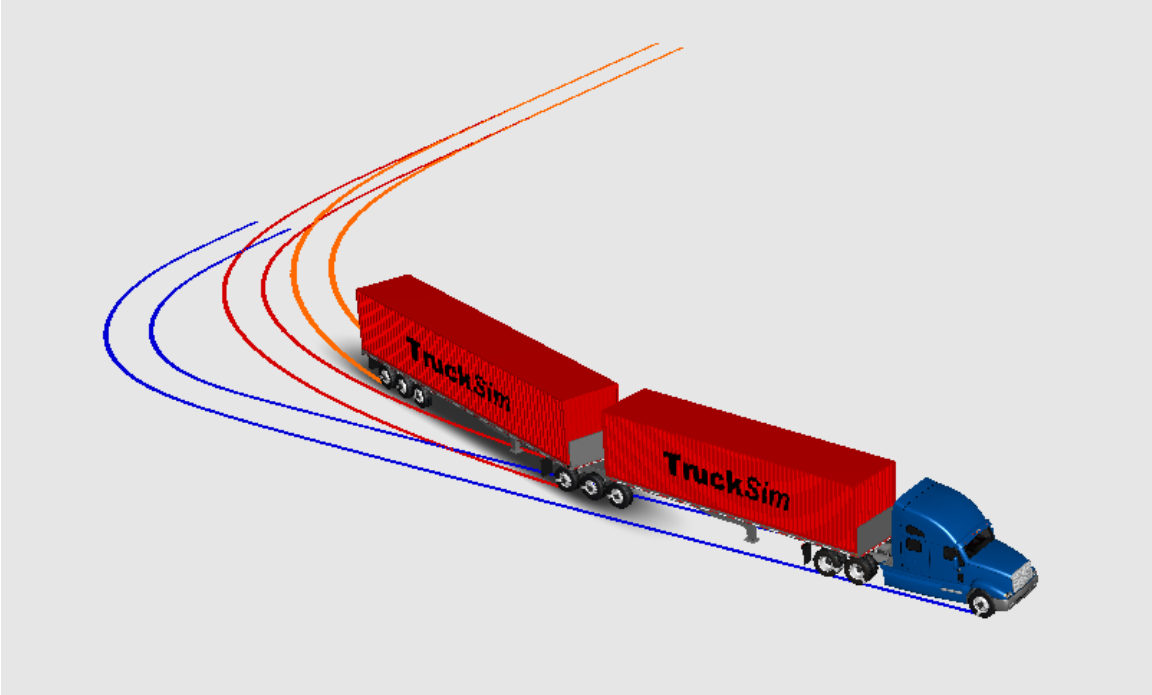

Figure 3.4: Diagram of the MTAHV model with the configuration of a tractor and two semitrailers

$x_1 - y_1 - z_1$, $x_2 - y_2 - z_2$ and $x_3 - y_3 - z_3$ for the tractor, 1st semitrailer and 2nd semitrailer, respectively, the governing equations of motion can be generated.

In the vehicle modeling, it is assumed that the forward speed U_1 of the vehicle and the tractor front wheel steering angle δ_{1f} are given. The pitch and bounce motions, braking and aerodynamic forces are ignored. The tire model used is a linear model that specifies the linear relationship between the tire lateral force and tire side-slip angle. Both the articulation angles between tractor and 1st semitrailer, and between 1st and 2nd semitrailer are assumed to be small. The roll stiffness and damping coefficients of the vehicle suspension systems are constant in the range of roll motions involved. The motion considered in this model are tractor side-slip angle β_1, tractor yaw rate $\dot{\psi}_1$, tractor roll angle ϕ_1, 1st semitrailer yaw rate $\dot{\psi}_2$, 1st semitrailer roll angel ϕ_2, 2nd semitrailer yaw rate $\dot{\psi}_3$, and 2nd semitrailer roll angle ϕ_3.

The linear 7 DOF MTAHV model can be expressed in the following state-space

form

$$\dot{\mathbf{x}} = \mathbf{A}\mathbf{x} + \mathbf{B_u}\mathbf{u} + \mathbf{B}\delta_{1f} \tag{3.3.1}$$

In the equation (3.3.1), the state variables $\mathbf{x}$ can be expressed as,

$$\mathbf{x} = \begin{bmatrix} \mathbf{x}_1 & \mathbf{x}_2 & \mathbf{x}_3 & \mathbf{x}_t \end{bmatrix}^T, \tag{3.3.2}$$

where $\mathbf{x}_1 = \begin{bmatrix} \phi_1 & \dot{\phi}_1 & \beta_1 & \dot{\psi}_1 \end{bmatrix}$, $\mathbf{x}_2 = \begin{bmatrix} \phi_2 & \dot{\phi}_2 & \beta_2 & \dot{\psi}_2 \end{bmatrix}$, $\mathbf{x}_3 = \begin{bmatrix} \phi_3 & \dot{\phi}_3 & \beta_3 & \dot{\psi}_3 \end{bmatrix}$, and $\mathbf{x}_t = \begin{bmatrix} \phi_{1t} & \phi_{2t} & \phi_{3t} \end{bmatrix}$. The control vector $\mathbf{u}$ can be cast as,

$$\mathbf{u} = \begin{bmatrix} \mathbf{u}_{\delta 1} & \mathbf{u}_{\delta 2} & \mathbf{u}_c & \mathbf{M} \end{bmatrix}^T. \tag{3.3.3}$$

where, $\mathbf{u}_{\delta 1} = \begin{bmatrix} \delta_{2f} & \delta_{2m} & \delta_{2r} \end{bmatrix}$, $\mathbf{u}_{\delta 2} = \begin{bmatrix} \delta_{3f} & \delta_{3m} & \delta_{3r} \end{bmatrix}$, $\mathbf{u}_c = \begin{bmatrix} u_{c1} & u_{c2} & u_{c3} \end{bmatrix}$, and $\mathbf{M} = \begin{bmatrix} M_1 & M_2 & M_3 \end{bmatrix}$. $\mathbf{A}$, $\mathbf{B}$, and $\mathbf{C}$ are the system, control and disturbance matrices, respectively and are presented in Appendix.

3.3.1 Linear Yaw-Plane Model with 4 DOF

The linear yaw-plane model with 4 DOF for the B-train Double LCV is generated following similar approach of the yaw-plane model with 3 DOF described in section 3.2.2.

3.3.2 Nonlinear TruckSim Model of B-train Double LCV

A nonlinear model of TruckSim is generated, in this research, with multiple DOF for the B-train Double long combination vehicle to validate the 5 DOF and 7 DOF models. Note that the tractor has three axles and each semitrailer has three rear axle sets. The tractor front axle has two wheels and the rest of the axles has four wheels. The degree of freedom can be calculated following the procedure described in section 3.2.3.

3.4 Summary

This chapter has introduced a linear 3 degree-of-fredom (DOF) yaw-plane model and a linear 5 DOF yaw-roll model for the tractor/semitrailer combination, and the corresponding TruckSim model. This chapter also presents a linear 4 DOF yaw-plane model, a linear 7 DOF yaw-roll model, and the nonlinear TruckSim model for the B-train Double longer combination vehicle (LCV). In the design optimization processes, only the yaw-roll models will be incorporated.

CHAPTER 4

Model Validation

4.1 Introduction

This chapter presents the validation of the yaw-plane and the yaw-roll models for the tractor/semitrailer combination and the B-train Double long combination vehicle (LCV) with the corresponding nonlinear models generated using TruckSim software package. A linear 3 DOF yaw-plane model and the linear 5 DOF yaw-roll model are generated to represent the tractor/semitrailer; the linear 4 DOF yaw-plane model and the linear 7 DOF yaw-roll model are designed to described the longer combination vehicle (LCV). These linear models are compared against with the corresponding nonlinear TruckSim models. This chapter also investigates the applicability of these vehicle models. Models of both of the STAHV and MTAHV yield excellent simulation results which are validated using the simulation results obtained from TruckSim models. The chapter also presents the eigenvalue analysis of the models to estimate their unstable motion modes. Benchmark comparison of the models has been performed to investigate the fidelity, complexity and applicability.

4.2 Eigenvalue Analysis

To identify the unstable motion modes and to estimate the critical speed, above which the vehicle loses its stability, eigenvalue analysis is widely used. Above critical forward speed the vehicle loses its stability. For the linear state-space models expressed in equation (3.2.3) and (3.3.1), the system matrix A is utilized for the eigenvalue analysis. Each pair of complex eigenvalues takes the following form,

$$S_{1,2} = R_e + j\omega_d \tag{4.2.1}$$

where R_e and ω_d represents the real and imaginary part of an eigenvalue, respectively. From this eigenvalue the damping ratio ζ is defined using the following equation.

$$\zeta = \frac{-R_e}{\sqrt{R_e^2 + \omega_d^2}} \tag{4.2.2}$$

The damping ratio is expressed as a function of vehicle forward speed to identify the unstable motion modes of the vehicle. The vehicle becomes unstable if any damping ratio takes a negative value. Figure 4.1 and 4.2 shows the relationship between the damping ratios and the forward speed for the 3 DOF and the 5 DOF models of the tractor/semitrailer combination, respectively. Each curve of damping ratios corresponds to a motion mode of the vehicle. If a curve enters the negative region, the vehicle becomes unstable. The closer the curve to the value of zero, the closer the vehicle is to the instability. It is clear from both the figures that the stability of the vehicles is decreased with the increase of forward speed.

4.2.1 Eigenvalue Analysis of the STAHV

Figure 4.1 shows that damping ratio curves for mode-1 and mode-2 decreases with increase of forward speed and mode-1 is more responsible for the instability. With this planner model based eigenvalue analysis, although limited information regarding instability is available, it is very difficult to identify whether the unstable motion mode is related to yaw or roll motion. However, the eigenvalue analysis of the 5 DOF yaw-roll model is very useful to estimate the instability with the help of

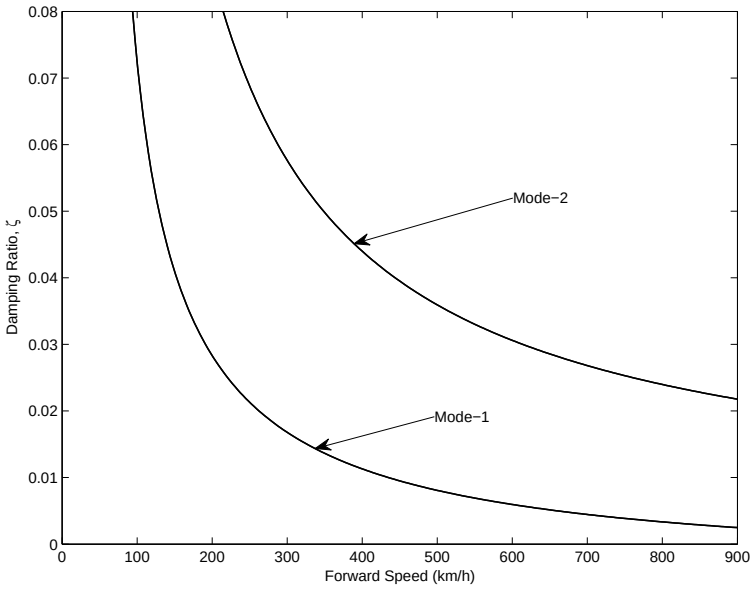

Figure 4.1: Damping ratio versus forward speed of the 3 DOF model

TruckSim simulations at different forward speeds. Among all the damping ratio curves, four important curves (mode-1, 2, 3 and 4) are shown in Figure 4.2, as they becomes comparatively closer to zero damping line with increase of the forward speed.

4.2.2 Eigenvalue Analysis for the MTAHV

Figures 4.3 and 4.4 show the damping ratio versus forward speed plots of the 4 DOF and the 7 DOF model of the MTAHV. It is clear from the figures that three dominating damping ratio curves of the 7 DOF model are very close to zero. Figure 4.5 represents the zoomed view of the plot. Since roll motion is absent in the 4 DOF model, the three dominating modes, i.e., modes 4, 5, and 6 shown in Figure 4.5 are absent in Figure 4.3. An evidence of the roll-over unstable motion is presented in the TruckSim animation as shown in Figure 4.6. In the simulation, the steering input is a single sine wave input of magnitude of 0.14 rad as shown in Figure 4.7 and the forward speed is 120 km/h. Although the eigenvalue analysis

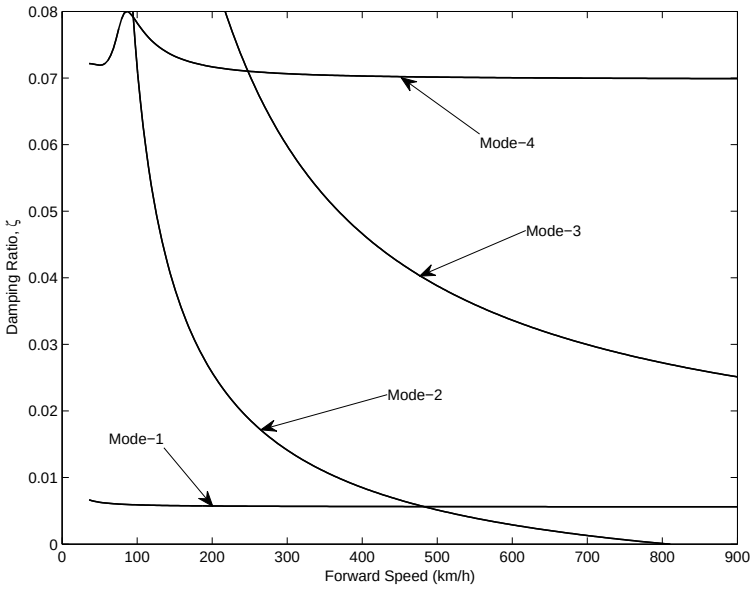

Figure 4.2: Damping ratio versus forward speed of the 5 DOF model

predicts the unstable motion modes, it is interesting that the simulation of the linear 7 DOF model is not capable of estimating this instability as shown in Figure 4.8. This is due to the fact that the linear model is not very accurate when used to determine the dynamic behavior at high lateral acceleration maneuvers, which will be discussed in detail later in Section 4.4. Note that during the TruckSim simulation, the lateral acceleration reaches up to 0.9g as shown in Figure 4.9.

4.3 Simulation Results under Low Lateral Acceleration Maneuver

To validate the generated vehicle models with those from the TruckSim, it is necessary to examine the dynamic behaviors of all the models under the same steering inputs and forward speed. In this section, a typical evasive lane change maneuver with low lateral acceleration (low-g) will be discussed for both the STAHV and MTAHV. For all the simulations of both the vehicle combinations described in this section, the forward speed is kept constant at the value of 88.0 km/h.

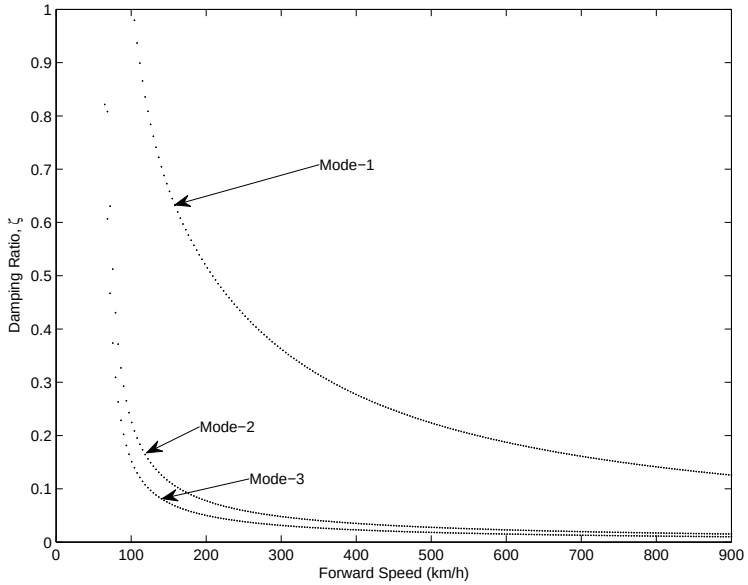

Figure 4.3: Damping ratio versus forward speed of the 4 DOF model

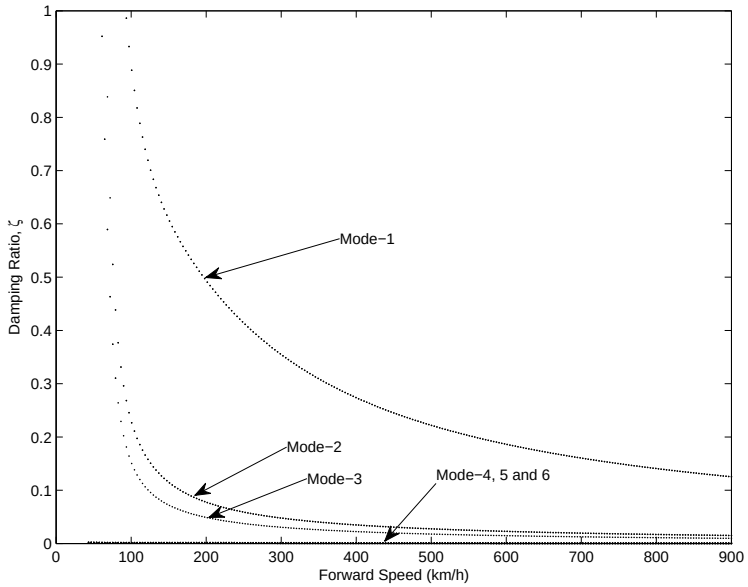

Figure 4.4: Damping ratio versus forward speed of the 7 DOF model

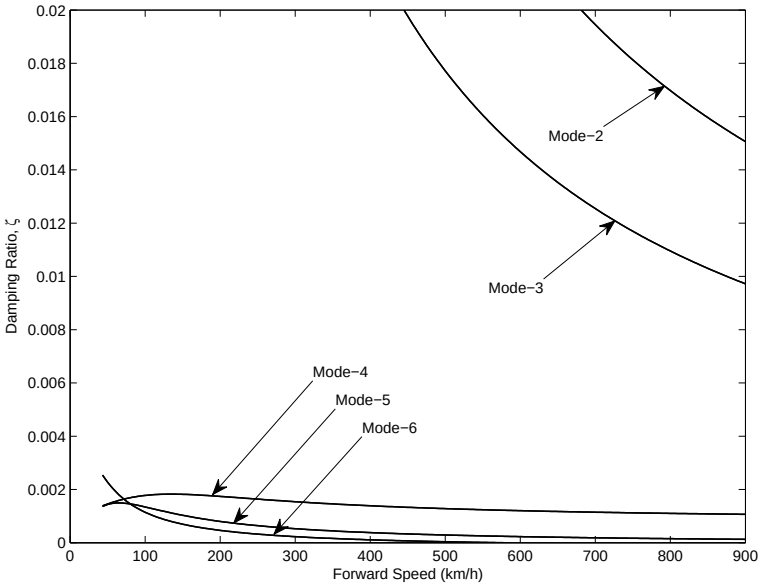

Figure 4.5: Dominating damping ratio versus forward speed of the 7 DOF model

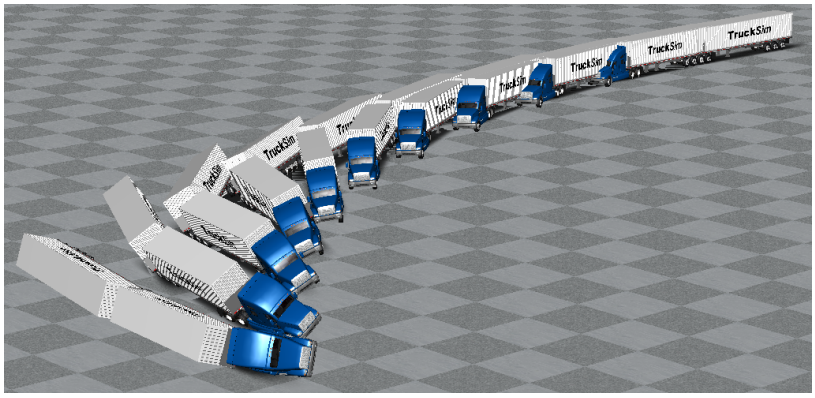

Figure 4.6: TruckSim animation of rollover motion of the MTAHV at a forward speed of 120 km/h

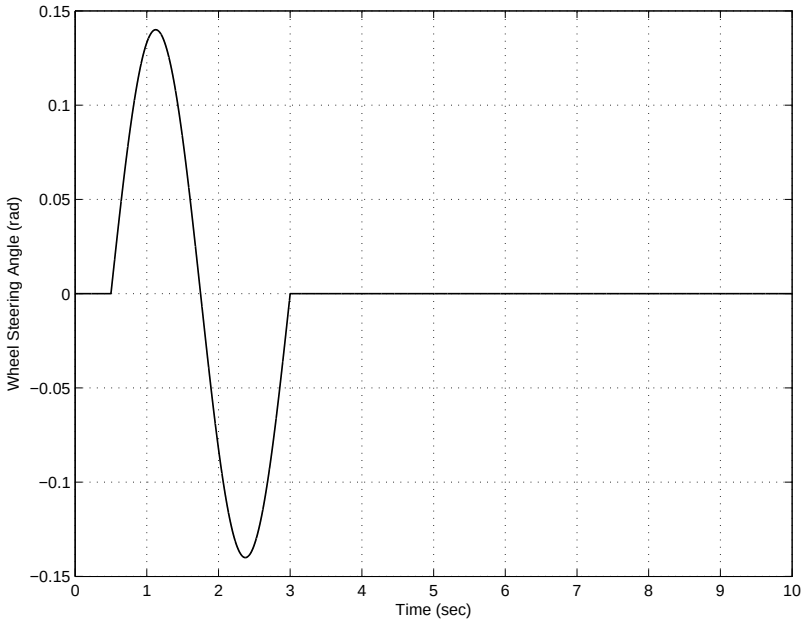

Figure 4.7: Tractor front axle wheel steering angle input time history of single lane-change maneuver to predict the unstable motion modes

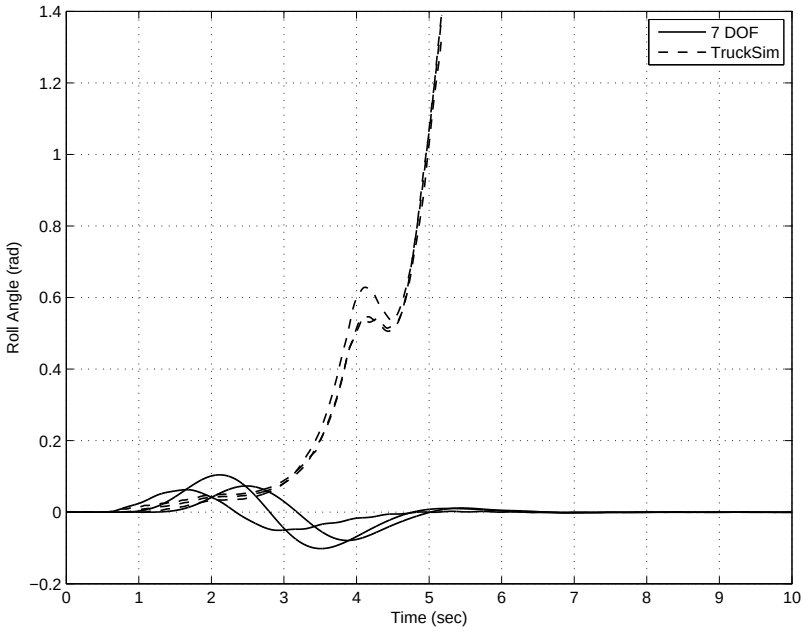

Figure 4.8: Roll angle time history of 7 DOF and TruckSim model of B-train Double at a forward speed of 120 km/h

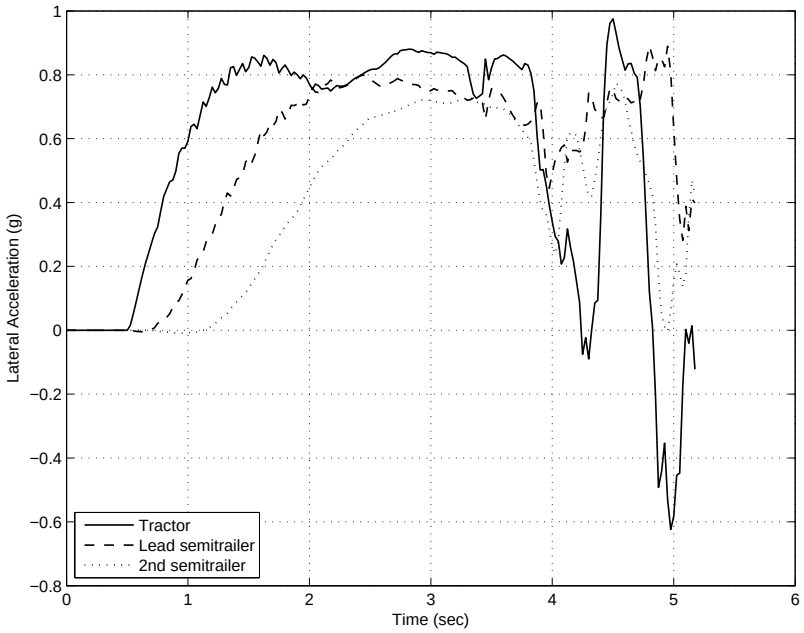

Figure 4.9: Acceleration time history of the TruckSim simulation at 120 km/h with single sine wave steering input of amplitude 0.14 rad

4.3.1 Simulation Results for STAHV

For the low-g simulation of the STAHV, the tractor front wheel steering input of the single sine wave with the amplitude of 0.0185 rad and frequency of 0.4 Hz is used as shown in Figure 4.10. The simulation results of this single lane change maneuver are shown in Figures 4.11 to 4.15. In Figure 4.11, the time history of the lateral accelerations at the center of gravity (CG) of tractor and that of semitrailer of the 3 DOF, the 5 DOF, and the TruckSim models are presented. Under the same steering input, the dynamic responses of the lateral accelerations of the tractor and semitrailer for all the three models are in good agreement. As shown in the figure, the peak lateral accelerations at the tractor center of gravity of all the models reach approximately 0.15g. The rearward amplification (RWA) ratios of lateral acceleration take the value of 1.1434, 1.1521, and 1.1641 for the 3 DOF, the 5 DOF, and the TruckSim models, respectively. It is clear from both the figure and the RWA ratios that the dynamic response of the 5 DOF model is closer to the TruckSim model compared to that of the 3 DOF model.

Figure 4.12 shows the time history of yaw rate of the tractor and the semitrailer under the low-g lane change maneuver for all the three models. It is clear from the figure that they are in very good agreement and the settling time is almost the same for all the three models. A close observation of the figure reveals that the rearward amplification of the way rate is higher than unity. The articulation angle versus time during the maneuver is described for the 3 DOF, the 5 DOF, and the TruckSim models in Figure 4.13. The peak value of the angle of articulation joint reaches up to the value of 0.03 rad, approximately.

The roll angle time history of the sprung masses of the tractor and the semitrailer for the 3 DOF, the 5 DOF and the TruckSim models under the single lane change maneuver is presented in Figure 4.14. The peak value of the roll angle of the tractor sprung mass reaches around 0.005 rad and that of the semitrailer sprung mass around 0.012 rad. Unlike the linear models, in the case of TruckSim model, the roll angle of the tractor sprung mass before the sine wave steering input and that of semitrailer after the sine wave steering input take slightly non-zero values due to the model nonlinearity.

To investigate the effect of tire lateral forces, an analysis is performed for each axle. The tire lateral force on each tire of an axle is added together. Note that the STAHV has five axles. The tractor has one front axle (two tires) and two rear axles (four tires in each axle); and the semitrailer has two rear axles (four tires in each axle). The total tire forces in each axle versus time are presented in Figure 4.15 for the three models. The solid line denotes the 3 DOF, the dashed line the 5 DOF, and the dashed dot line the TruckSim model as before. Also note that in the figure the topmost plot of this figure corresponds to axle-1 (the front axle of tractor); the plot just below it represents axle-2 (the tractor first driving axle) and so on. The close agreement among the three models in axle lateral tire forces validates the 3 DOF and the 5 DOF linear models under the low-g lateral acceleration maneuver.

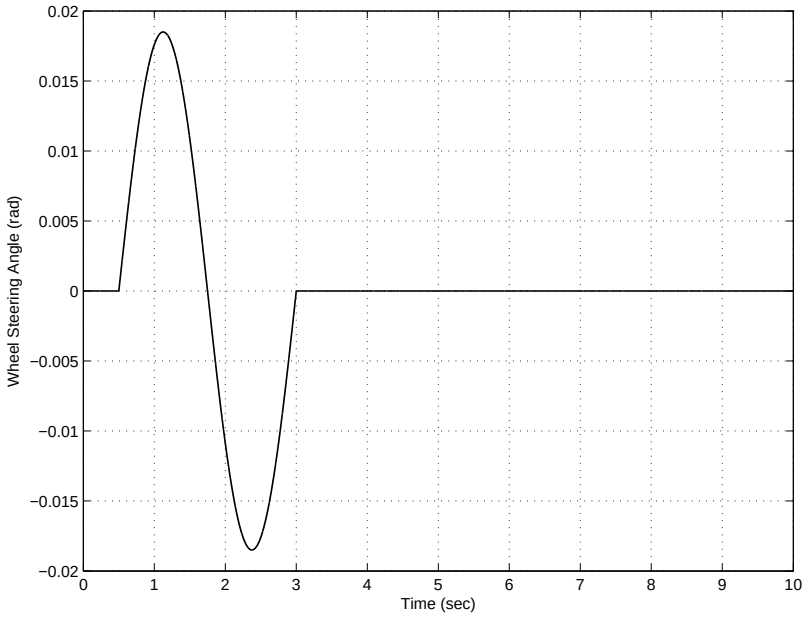

Figure 4.10: Front wheel steering angle input time history of the STAHV for the single lane-change maneuver at low lateral acceleration

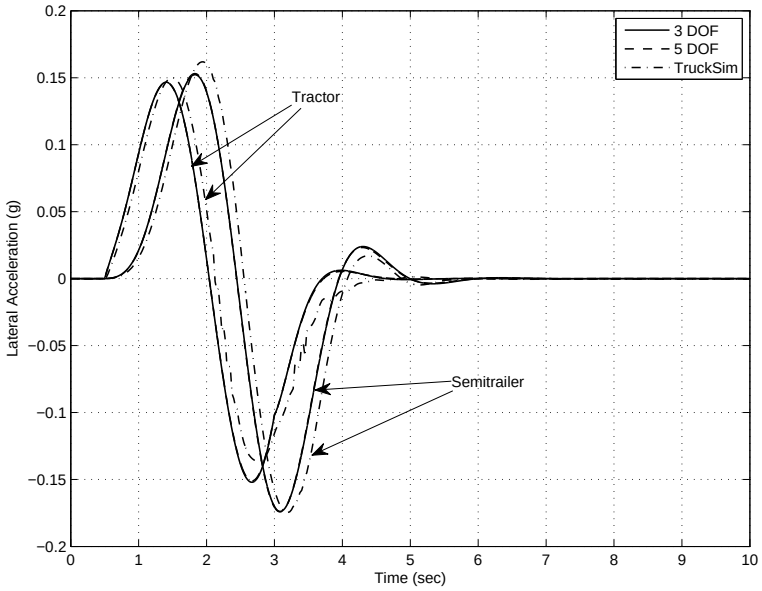

Figure 4.11: Lateral acceleration time history under the single sine-wave steering input at a forward speed of 88.0 km/h

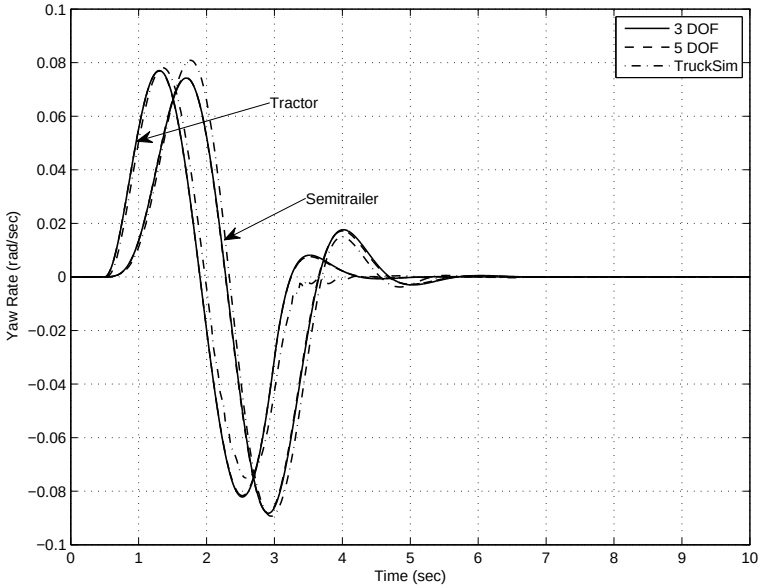

Figure 4.12: Yaw rate time history of the STAHV under the single sine-wave steering input at a forward speed of 88.0 km/h

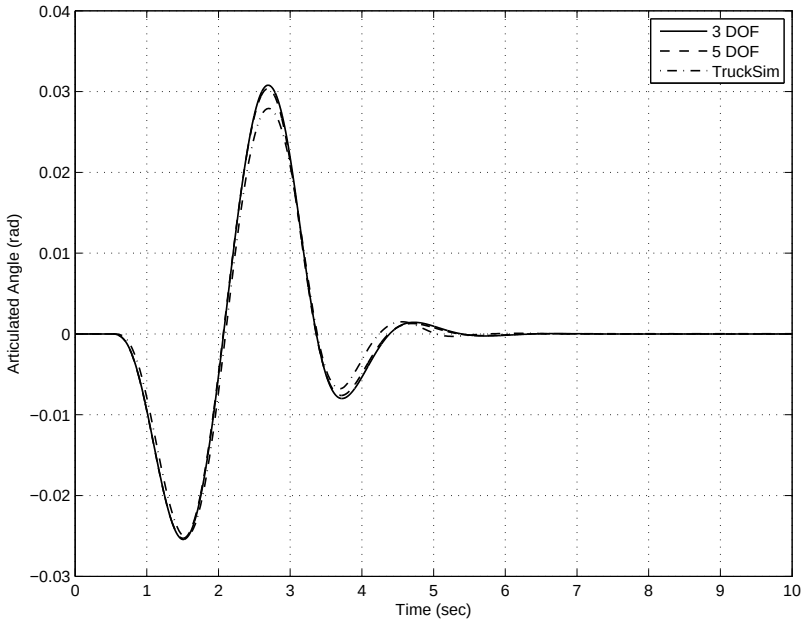

Figure 4.13: Articulated angle time history of the STAHV at low lateral acceleration condition under the single sine-wave steering input at a forward speed of 88.0 km/h

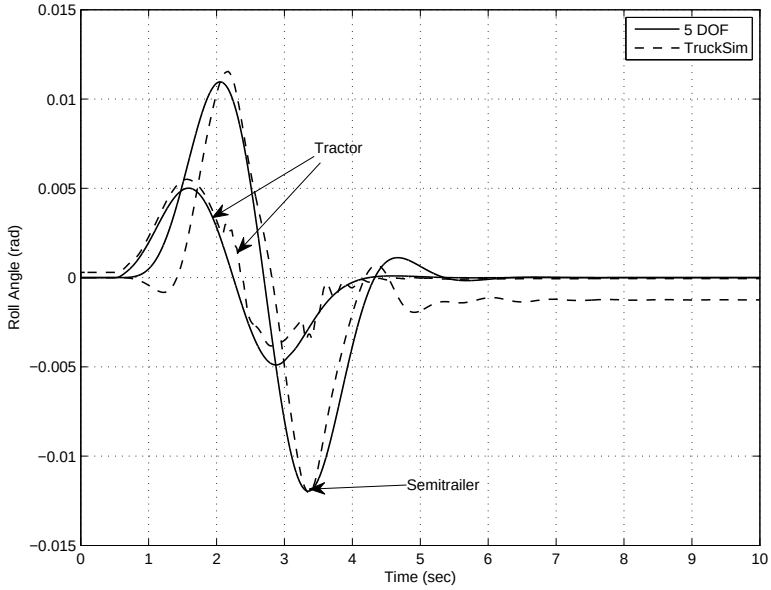

Figure 4.14: Time history of the roll angle of sprung mass of the STAHV at the low lateral acceleration condition under the single sine-wave steering input at a forward speed of 88.0 km/h

4.3.2 Simulation Results for the MTAHV

To investigate the dynamic responses of the 4 DOF, the 7 DOF, and the TruckSim models of the MTAHV, a similar single lane change maneuver is simulated under a low lateral acceleration (low-g) with the same driving condition. In this case, the front axle wheel steering input is a single sine wave of the amplitude of 0.0248 rad and the frequency of 0.4 Hz as shown in Figure 4.16. The vehicle forward speed is constant at 88.0 km/h.

Figure 4.16 shows the lateral accelerations of the 4 DOF, the 7 DOF and the TruckSim models at the center of gravity (CG) of the tractor, the first-semitrailer, and second semitrailer of the MTAHV versus time. For all the three cases, the peak lateral accelerations of the tractor are 0.15g approximately. A close observation of the figure reveals that the dynamic responses of the three models are very close until the front wheel steering input reaches the negative peak value of -0.0248 rad. Despite of slight deviation of lateral acceleration curves of the 4 DOF and the 7

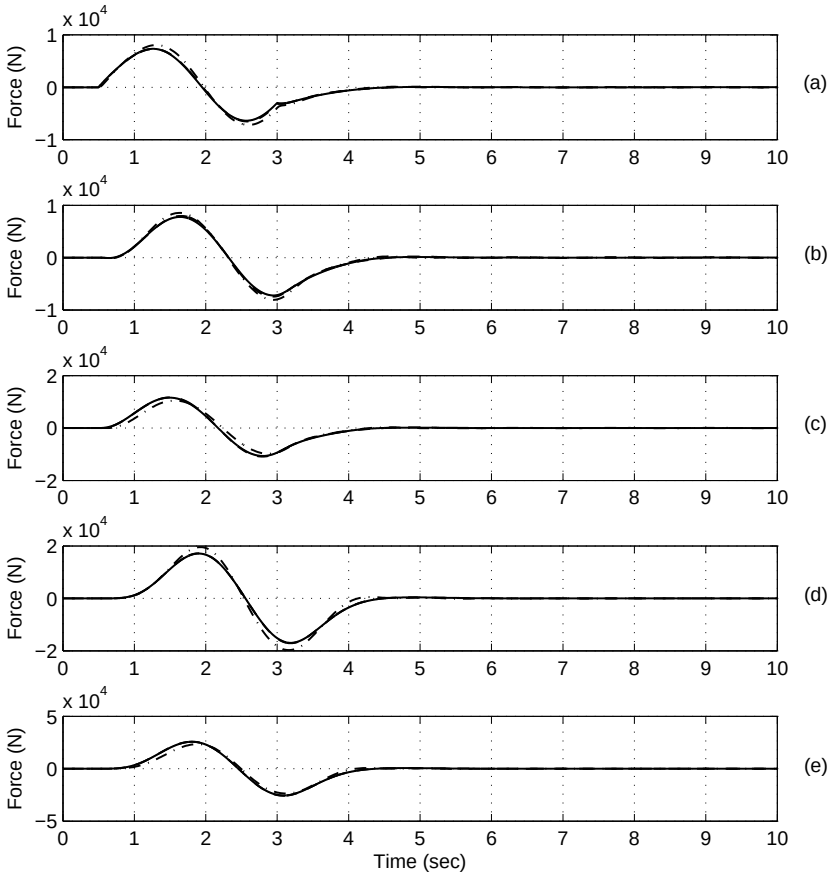

Figure 4.15: Time history of the total tire forces in each axle of the STAHV at the low lateral acceleration condition under the single sine-wave steering input at the forward speed of 88.0 km/h: 3 DOF (solid line), 5 DOF (dashed line), TruckSim (dashed dot line); (a) axle-1, (b) axle-2 and so on

DOF models from the TruckSim model after this point, most of the important dynamic information is preserved. The RWA ratios of the 4 DOF, the 7 DOF, and the TruckSim model are 0.8803, 0.8908, and 0.8901, respectively. Compared to the 4 DOF planner model, the 7 DOF yaw-roll model estimates much closer the value of the RWA ratio of lateral acceleration to the TruckSim model.

The time history of yaw rate of each vehicle units of MTAHV models are presented in Figure 4.18. The tractor and 1st semitrailer yaw rates of the three models are in very good agreement. A slight deviation of the 2nd semitrailer yaw rate time history of the linear models from the TruckSim model is observed. The first and second articulation angle time history of the 4 DOF, the 7 DOF, and the TruckSim model is shown in Figure 4.19. The roll angle of the sprung masses of the tractor, the 1st-semitrailer, and the 2nd semitrailer versus time of the three models are compared in Figure 4.20. Following the similar method, described in Subsection 4.3.1, the lateral tire force in each axle is calculated and plotted in Figure 4.21. Like Figure 4.15, the topmost plot of Figure 4.21 represents the lateral tire force of tractor front axle and so on. Note that, in the MTAHV, the tractor has one front axle (two tires) and two rear axles (four tire in each axle); the 1st semitrailer has three axles (two tires in each axle); and the 2nd semitrailer also has three axles (two tires in each axle). The line style in Figure 4.21 is the same as in Figure 4.15 (see Subsection 4.3.1). The lateral tire force time history in each axle is in good agreement for the three models.

The amount of lateral load transfer in the tractor under the lane change maneuver is also investigated for the 7 DOF and the MTAHV model as shown in Figure 4.22 and the corresponding load transfer ratio time history is presented in Figure 4.23. The total amount of lateral load transfer of the front axle and the rear axle group (two rear axles together) of tractor are calculated separately. The slight differences in the lateral load transfer cures, in Figure 4.22, between the two models are due to the variation of roll angles of sprung mass of tractor as shown in Figure 4.20. The trajectory of front axle center of tractor and the rearmost axle of the 2nd semitrailer of both the 7 DOF and the TruckSim model is presented in Figure 4.24.

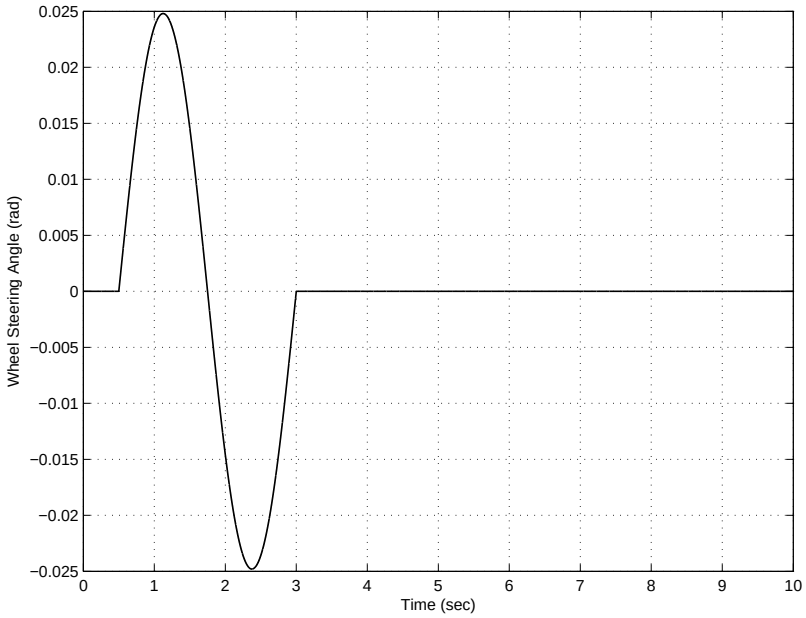

Figure 4.16: Front wheel steering angle input time history of MTAHV for the single lane-change maneuver at low lateral acceleration

It is clear from the figure that the lateral displacement of the 7 DOF model is little bigger than the TruckSim model. This difference can be understood by further investigating the lateral acceleration time history presented in Figure 4.17. The TuckSim model has a little more lateral acceleration in the negative side to finish the lane change earlier than in the case of the 7 DOF model. The time history of all these vehicle responses are in close agreement and validates the 4 DOF and the 7 DOF linear models with the TruckSim model under the low-g maneuvers.

4.4 Simulation Results under a High Lateral Acceleration Maneuver

The previous section indicates that the linear models are valid under the low lateral acceleration maneuvers. With this finding it can also be concluded that the linear models are also valid in low speed turn maneuvers, for example, 90-degree intersection turn or circular roundabout turn maneuver. Note that at the low speed maneuvers, both the lateral acceleration and the lateral velocity are low. Hence, the

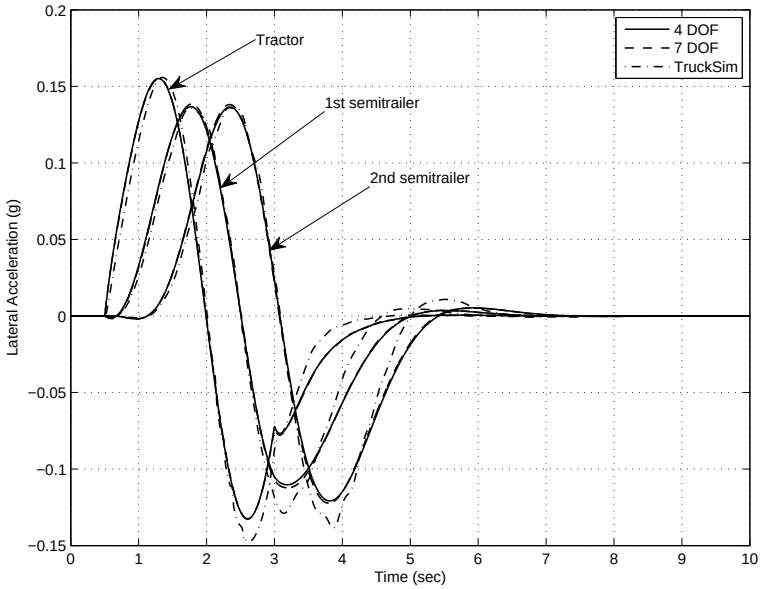

Figure 4.17: Lateral acceleration time history under the single sine-wave steering input at a forward speed of 88.0 km/h

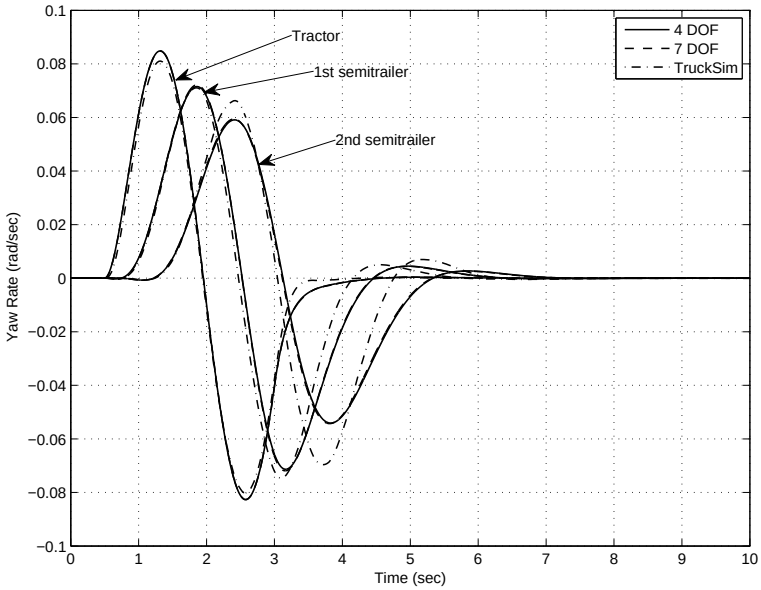

Figure 4.18: Yaw rate time history of the MTAHV under the single sine-wave steering input at a forward speed of 88.0 km/h

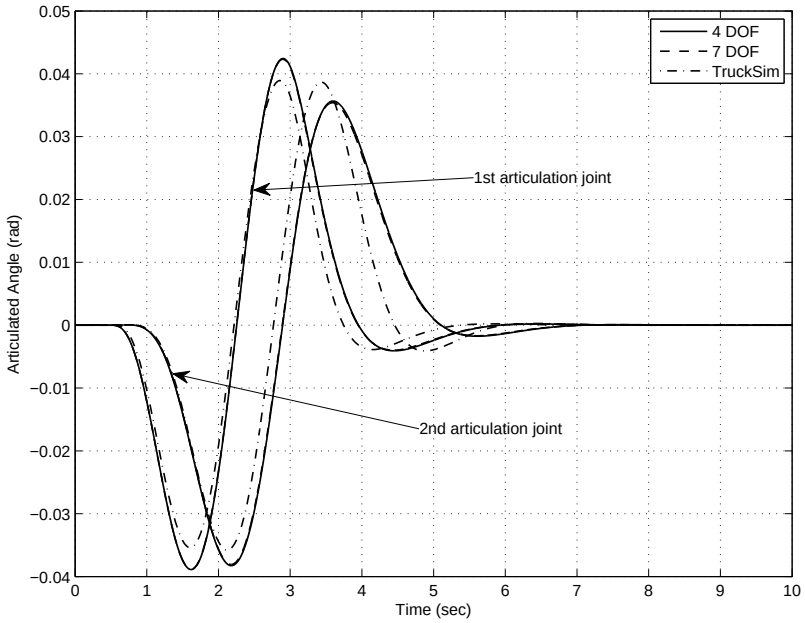

Figure 4.19: Articulated angle time history of MTAHV at low lateral acceleration condition under the single sine-wave steering input at a forward speed of 88.0 km/h

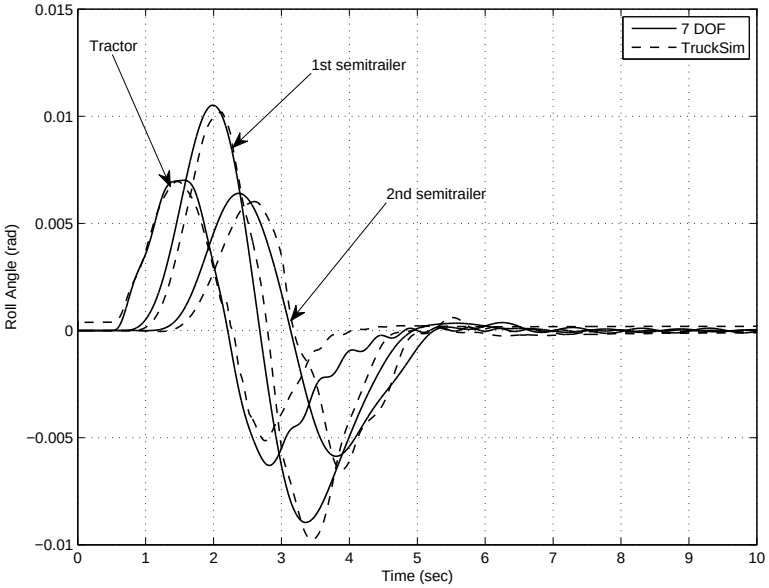

Figure 4.20: Time history of the roll of the sprung mass of the MTAHV at the low lateral acceleration condition under the single sine-wave steering input at a forward speed of 88.0 km/h

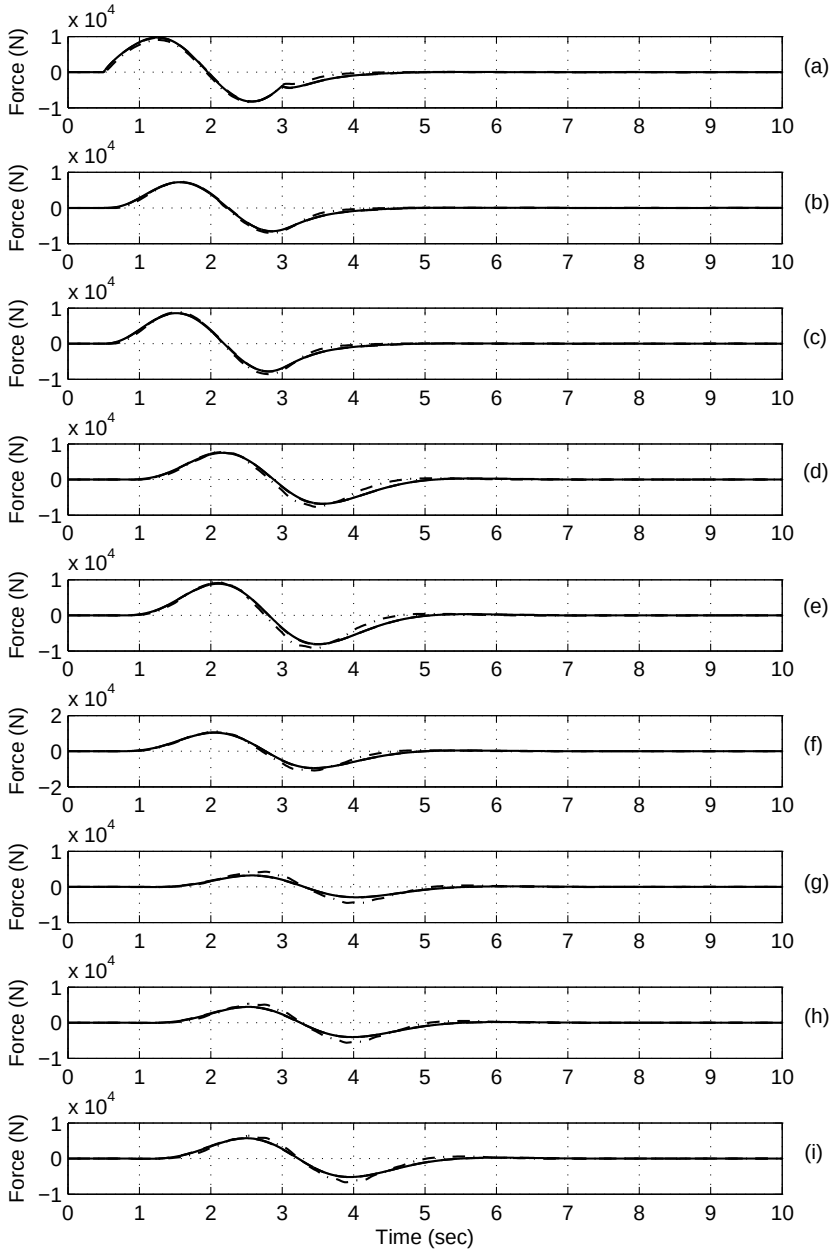

Figure 4.21: Time history of the total tire forces in each axle of the MTAHV at low lateral acceleration condition under the single sine-wave steering input at a forward speed of 88.0 km/h: 4 DOF (solid line), 7 DOF (dashed line), TruckSim (dashed dot line); (a) axle-1, (b) axle-2 and so on

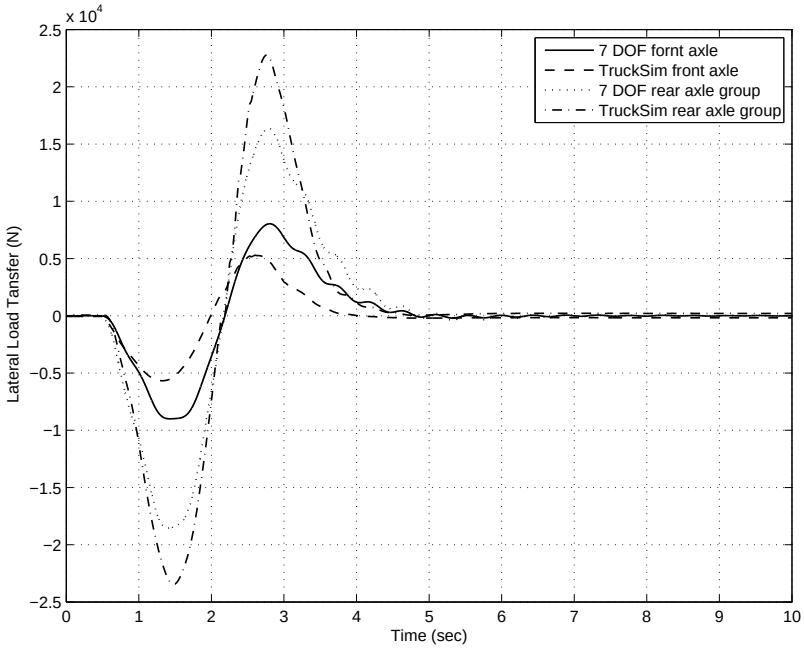

Figure 4.22: Time history of lateral load transfer in each axle of the MTAHV at the low lateral acceleration condition under the single sine-wave steering input at a forward speed of 88.0 km/h

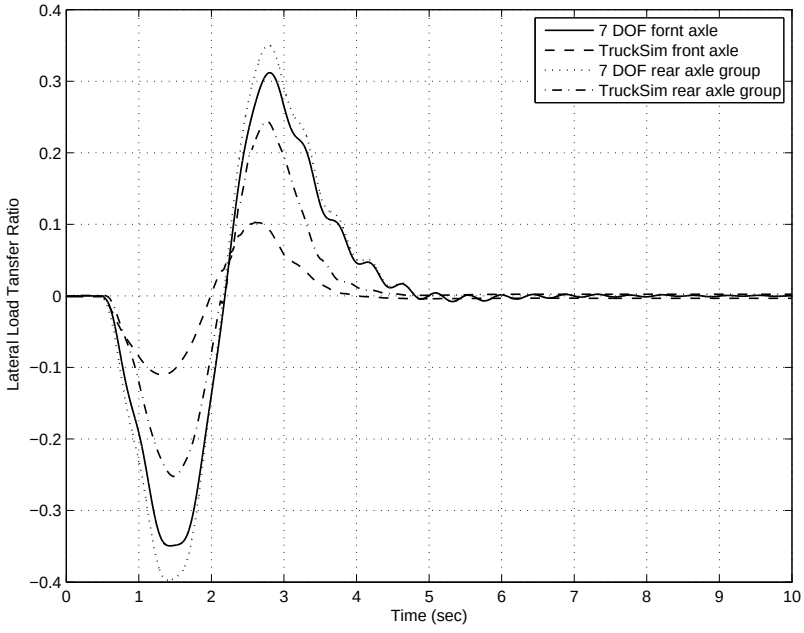

Figure 4.23: Time history of lateral load transfer ratio in each axle of the MTAHV at the low lateral acceleration condition under the single sine-wave steering input at a forward speed of 88.0 km/h

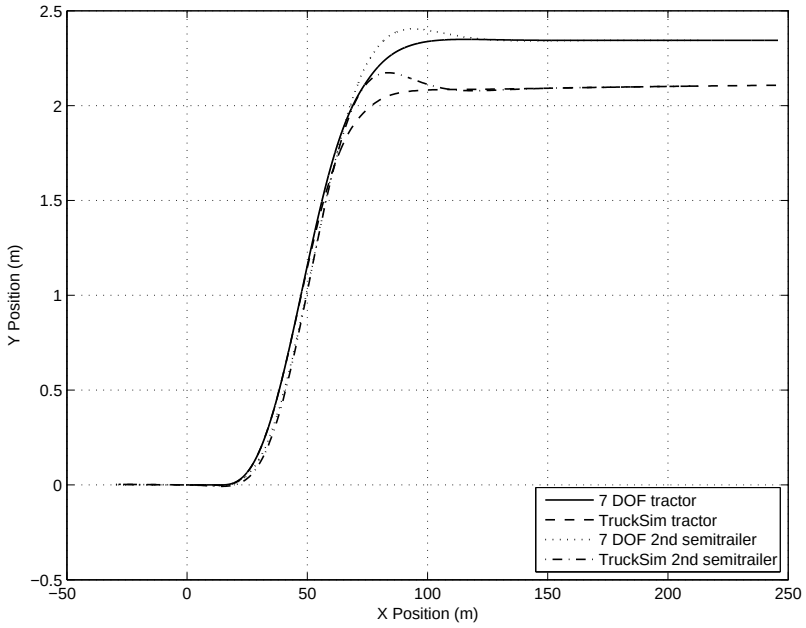

Figure 4.24: Trajectory of the front axle center and that of the rearmost axle of the MTAHV at low lateral acceleration condition under the single sine-wave steering input at a forward speed of 88.0 km/h

tire lateral slip angle remains small enough to lie in the linear range.

In this section, the dynamic behaviors of both the STAHV and the MTAHV models are investigated under a high lateral acceleration (high-g) evasive lane change maneuver. In this case, the front axle wheel steering input used to simulate the maneuver of both the vehicle combinations is shown in Figure 4.7. The single sine wave steering input, in the figure, has an amplitude of 0.14 rad with the frequency of 0.4 Hz. The vehicle forward speed is constant at 88.0 km/h during the lane change maneuver.

4.4.1 STAHV Simulation Results for High-g Case

Under the evasive lane change maneuver, the lateral acceleration time history at the center of gravity (CG) of the tractor and the semitrailer are presented in Figure 4.25. It is clear from the figure that although the lateral acceleration response of the 3 DOF and the 5 DOF model are in good agreement, they are far away from the

response of the TruckSim model. This difference is a clear indication that the linear models are no longer valid at the high lateral acceleration maneuver. In this figure, the peak lateral acceleration at the tractor CG of TruckSim model is approximately 0.8g. On the other hand, the peak lateral accelerations of the 3 DOF and the 5 DOF models reach as large as 1.28g.

The yaw rate time history of the tractor, 1st semitrailer and 2nd semitrailer are shown in Figure 4.26. The articulation angle time history is presented in Figure 4.27. The roll angle of the vehicle units are shown in Figure 4.28. These figures reveal that the yaw rate, articulation and roll angle time history of the linear model are far away from those of the TruckSim model. The main reason of the huge differences is mainly due to the difference in the tire models used. In the linear model the lateral fore of each tire is a linear function of tire lateral side slip angle. In the TruckSim model, however, a nonlinear tire model is used, where the tire lateral forces are increased with the increase of tire side slip angle up to a certain value. After this value of tire slip angle, the lateral tire forces start to decrease due to saturation with further increase in tire lateral side slip angles. This type of lateral tire force saturation is absent in the case of linear tire model in the 3 DOF and the 5 DOF models. Hence, with the same steering input under the higher lateral acceleration maneuver, the linear models have higher value of lateral tire forces than the TruckSim model. This phenomenon is clearly shown in the time history of the lateral tire forces in each axle of the 3 DOF, the 5 DOF, and the TruckSim model in Figure 4.29. All the notations in this figure are consistent with the Figure 4.15.

4.4.2 MTAHV Simulation Results for High-g Case

The simulation results of the 4 DOF, the 7 DOF, and the TruckSim models of the MTAHV under the high lateral acceleration are presented from Figure 4.30 to 4.35. The lateral acceleration time history at the tractor, 1st semitrailer, and 2nd semitrailer of the MTAHV is shown in Figure 4.30. Like the case of the STAHV, the lateral acceleration responses of the linear models and the TruckSim model of MTAHV are very different from each other. Figures 4.31, 4.32, and 4.33 show the

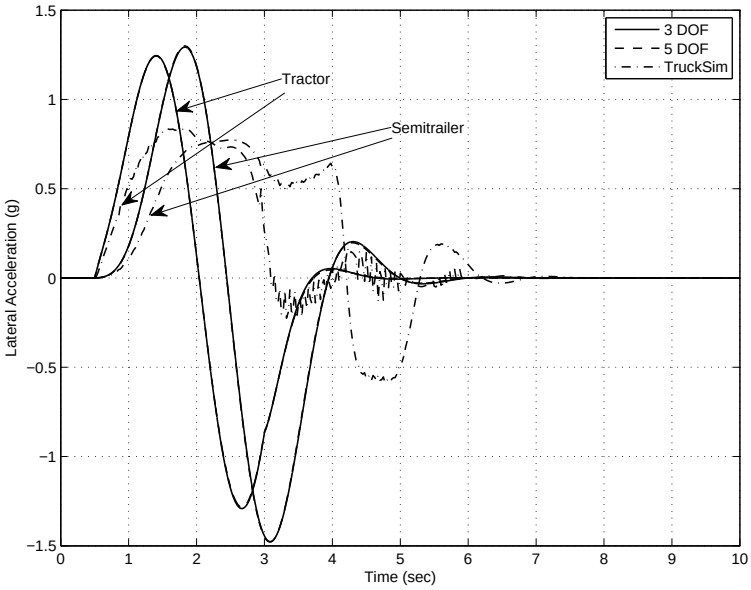

Figure 4.25: Lateral acceleration time history of the STAHV under the high lateral acceleration maneuver with the single sine-wave steering input (A=0.14 rad) at a forward speed of 88.0 km/h

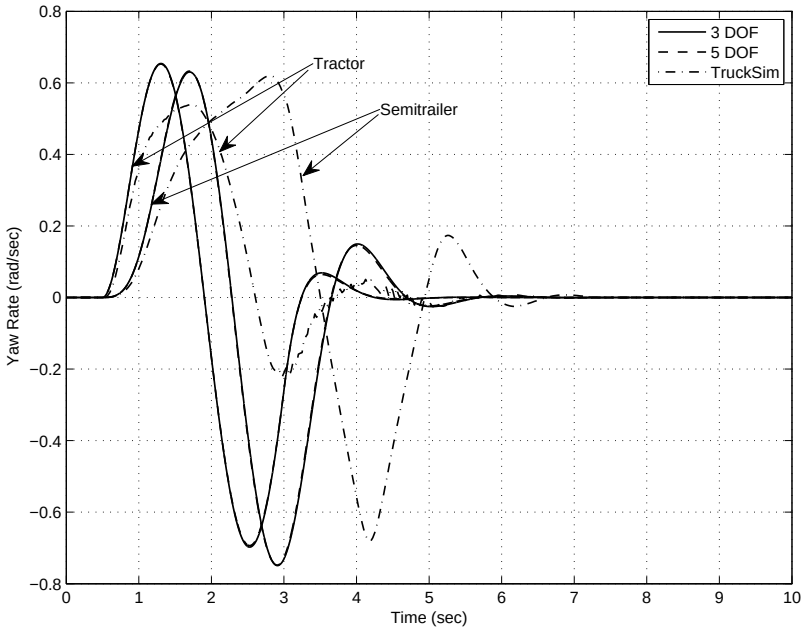

Figure 4.26: Yaw rate time history of the STAHV under the high lateral acceleration maneuver with the single sine-wave steering input (A=0.14 rad) at a forward speed of 88.0 km/h

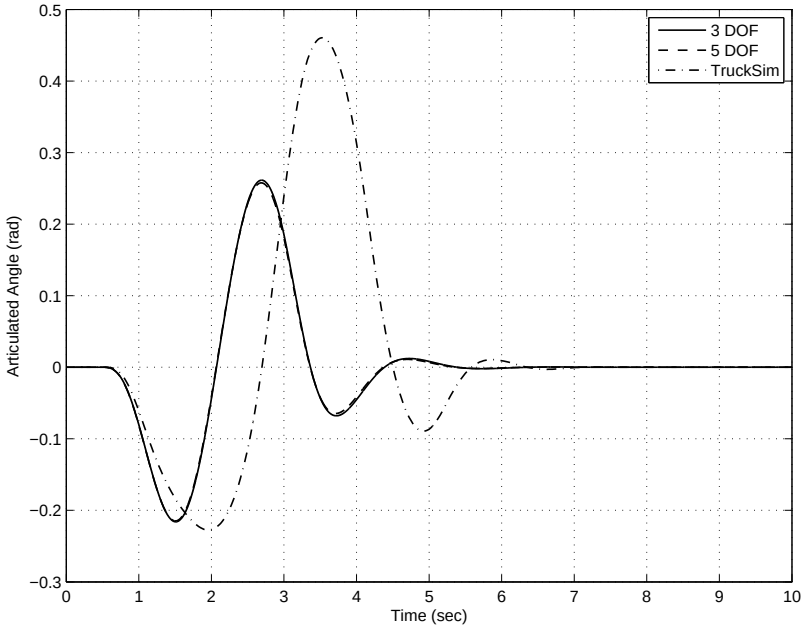

Figure 4.27: Articulated angle time history of the STAHV at the high lateral acceleration condition under the single sine-wave steering input at a forward speed of 88.0 km/h

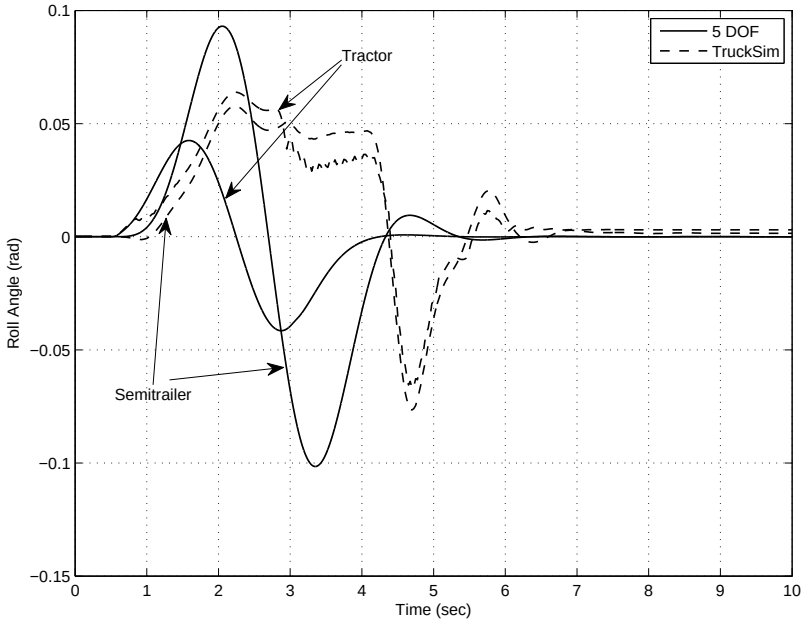

Figure 4.28: Time history of roll of sprung mass of the STAHV at high lateral acceleration condition under the single sine-wave steering input at a forward speed of 88.0 km/h

yaw rate, articulation angle, and roll angle time history of the three models under the high-g lane change maneuver. All these responses of the 4 DOF and the 7 DOF model are very different from those of TruckSim model. This difference is also due the same reason of tire force saturation of the nonlinear tire model at the higher lateral tire slip angle, as described in the previous subsection. The tire lateral forces in each axle are presented in Figure 4.34. Note that all the notations of this figure are same as in Figure 4.29. A close observation of the figure reveals that the tire lateral forces of the linear 4 DOF, and the 7 DOF models are higher than those of the TruckSim model which is very similar to the case of STAHV.

Figure 4.35 shows the trajectory of the front axle center of the tractor and that of the 2nd semitrailer of the 7 DOF linear model and those of the TruckSim model under the high-g lane change maneuver. The effect of the difference between the linear and the nonlinear tire model is very evident here. In the nonlinear TruckSim model, with the increase of tire lateral side slip angle, the lateral tire forces become saturated at some point. The nonlinear tire model cannot generate enough lateral tire force to complete the lane change. On the other hand, in the case of the linear tire model, the lateral tire force is always directly proportional to the tire lateral side slip angle. The linear tire model thus can generate enough lateral tire force even at the higher lateral acceleration to complete the lane change, which would not be the case in reality.

4.5 Summary

This chapter presents a systematic validation and comparison of the linear 3 DOF yaw plane model and the linear 5 DOF yaw-roll model of the STAHV, and the linear 4 DOF yaw plane model and the linear 7 DOF yaw-roll model of the MTAHV against the corresponding nonlinear TruckSim models. The comparison has been performed in terms of fidelity, complexity, and applicability for the lateral motion controller design. The linear models are effective to estimate the lateral stability and also to predict dominating motion modes leading to possible instability.

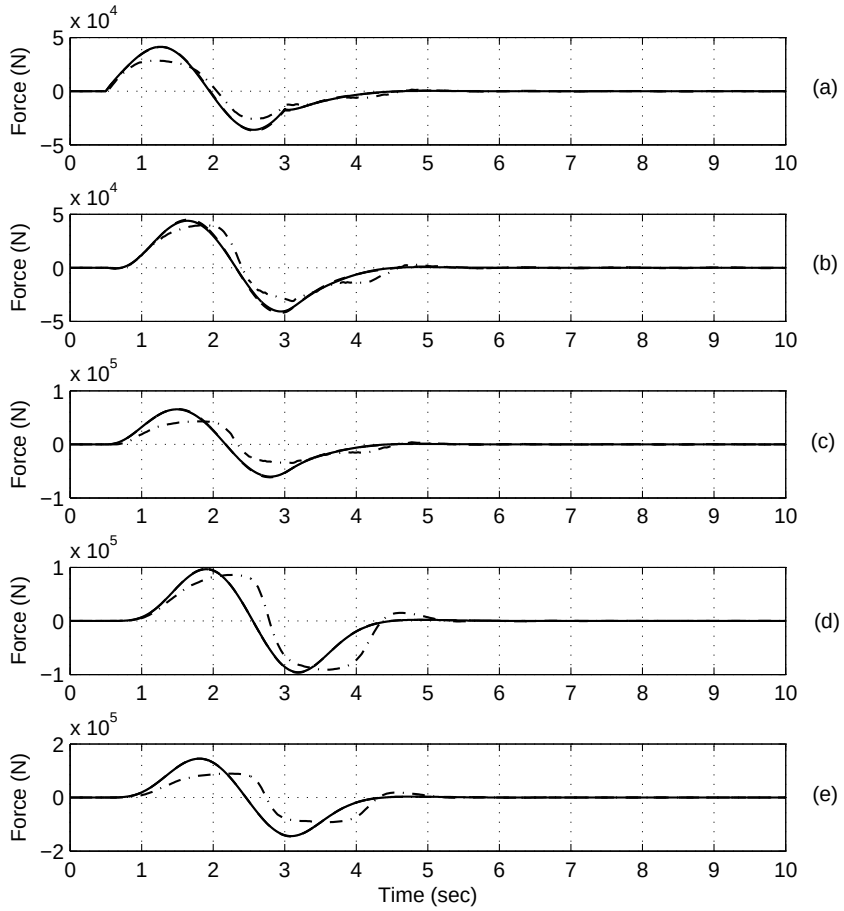

Figure 4.29: Time history of the total tire forces in each axle of STAHV at high lateral acceleration condition under the single sine-wave steering input at a forward speed of 88.0 km/h: 3 DOF (solid line), 5 DOF (dashed line), TruckSim (dashed dot line); (a) axle-1, (b) axle-2 and so on

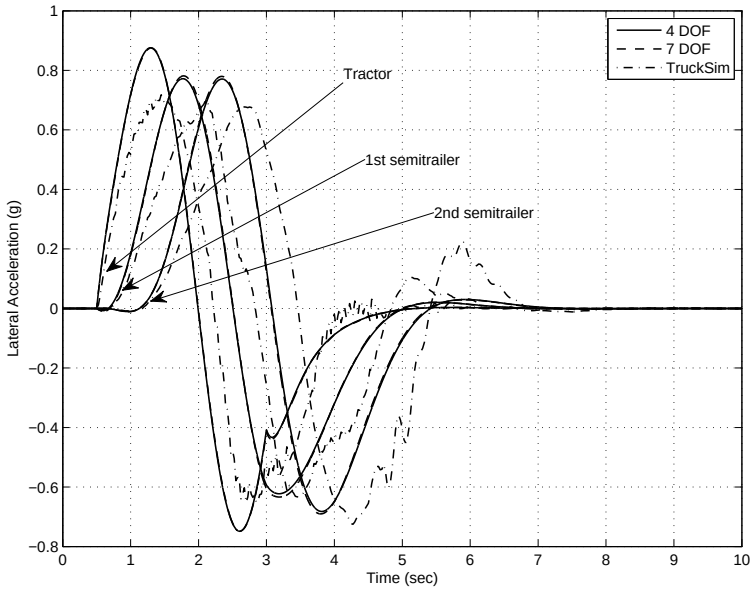

Figure 4.30: Lateral acceleration time history of the MTAHV under the high lateral acceleration maneuver with the single sine-wave steering input (A=0.14 rad) at a forward speed of 88.0 km/h

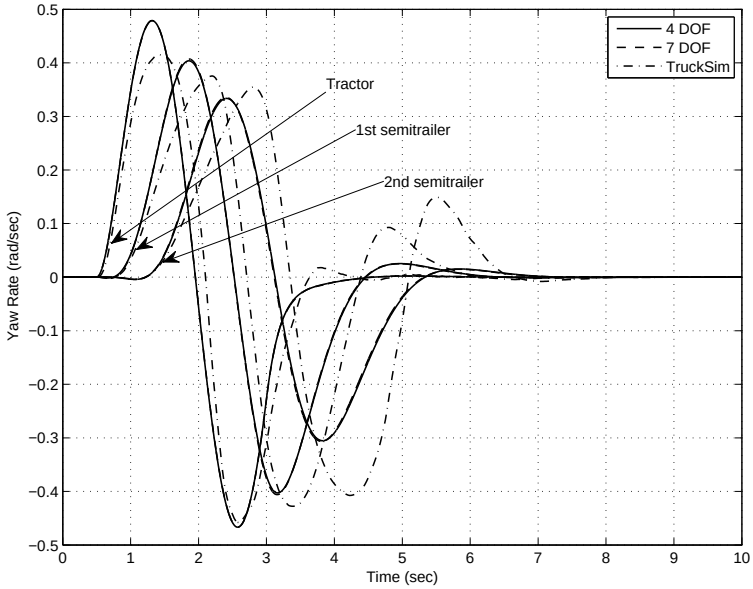

Figure 4.31: Yaw rate time history of the MTAHV under the high lateral acceleration maneuver with the single sine-wave steering input (A=0.14 rad) at a forward speed of 88.0 km/h

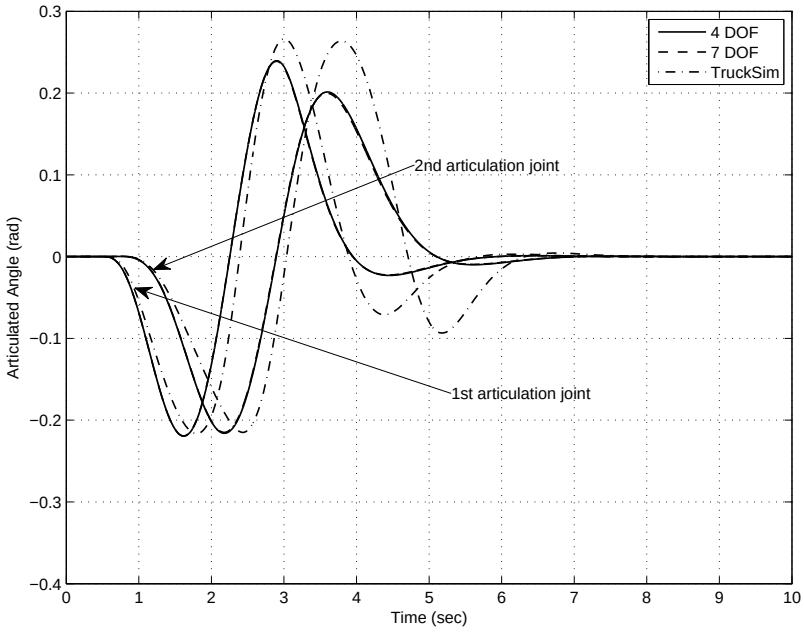

Figure 4.32: Articulated angle time history of the MTAHV at the high lateral acceleration condition under the single sine-wave steering input at a forward speed of 88.0 km/h

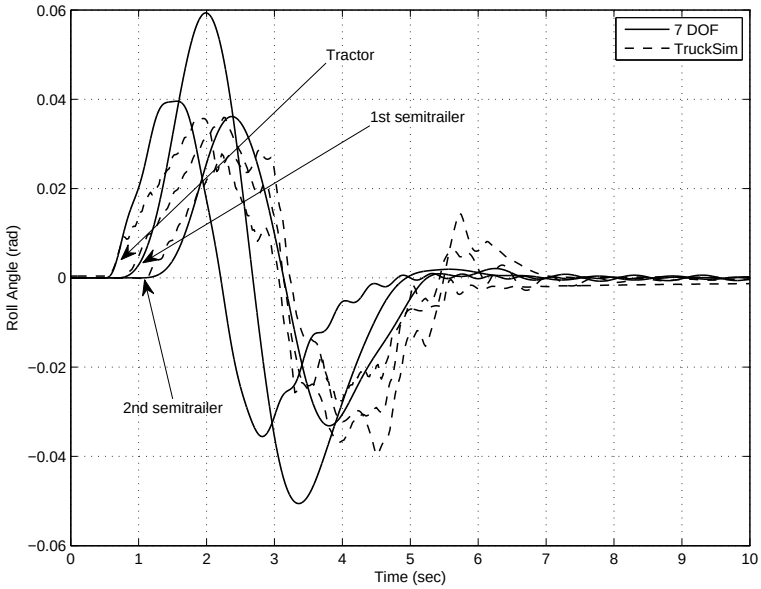

Figure 4.33: Time history of roll of sprung mass of the MTAHV at high lateral acceleration condition under the single sine-wave steering input at a forward speed of 88.0 km/h

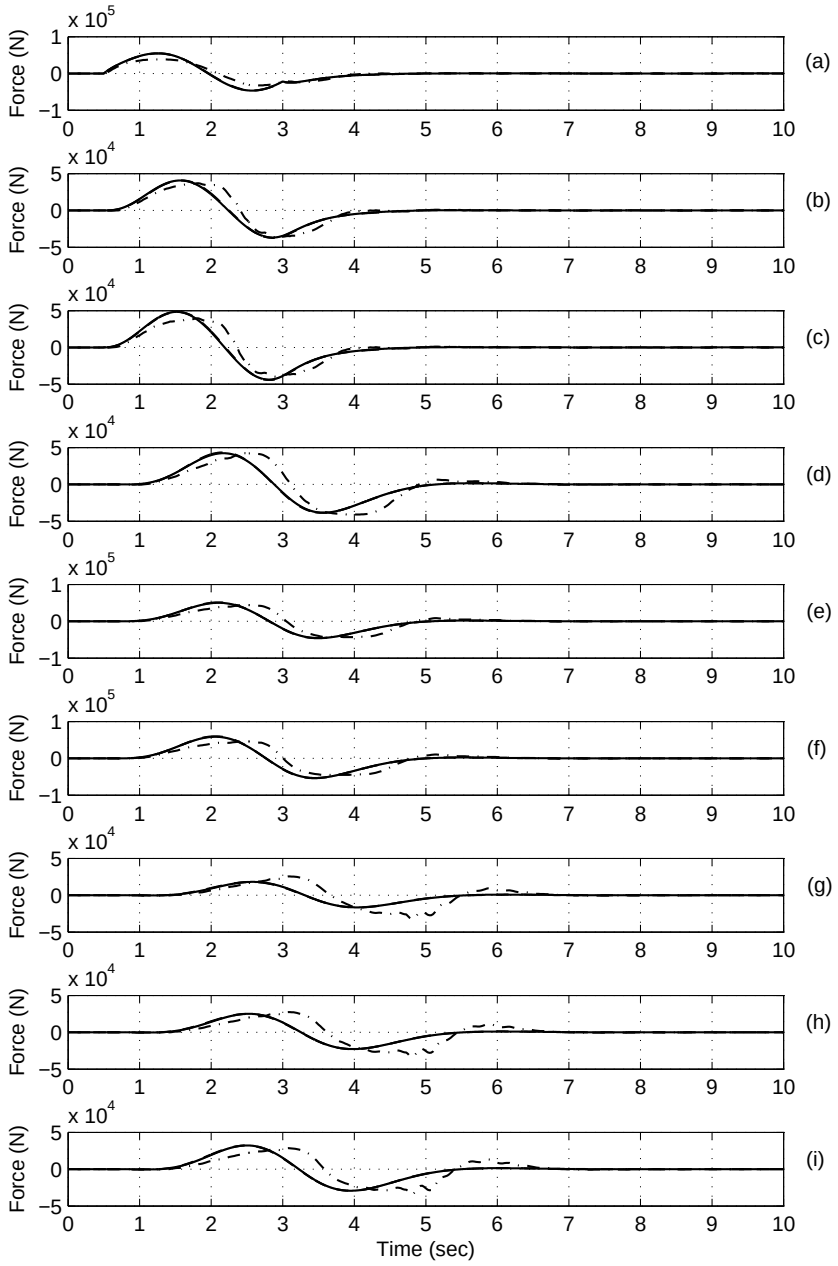

Figure 4.34: Time history of the total tire forces in each axle of MTAHV at the low lateral acceleration condition under the single sine-wave steering input at the forward speed of 88.0 km/h: 4 DOF (solid line), 7 DOF (dashed line), TruckSim (dashed dot line); (a) axle-1, (b) axle-2 and so on

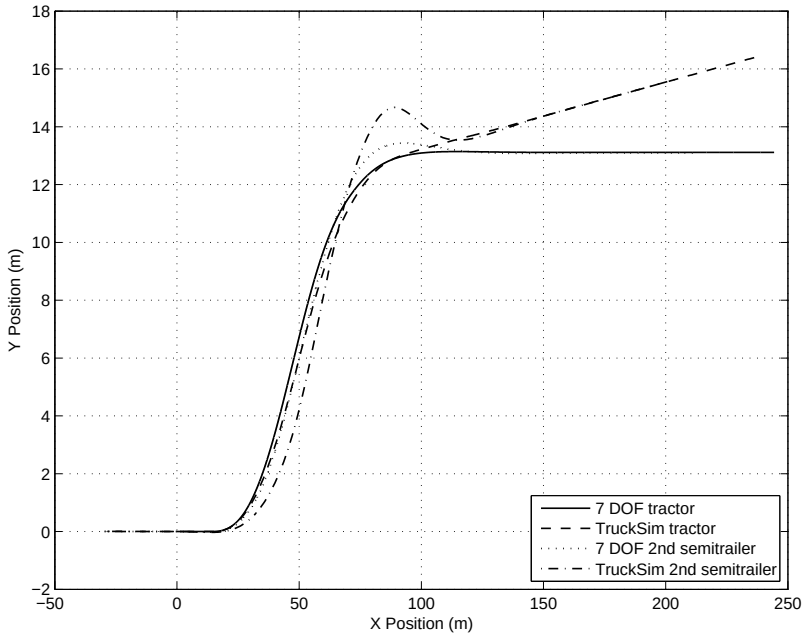

Figure 4.35: Trajectory of the front axle center and that of the rearmost axle of the MTAHV at the high lateral acceleration condition under the single sine-wave steering input at a forward speed of 88.0 km/h

Under regular evasive maneuvers at low lateral acceleration (lower than 0.3g), the linear models are suitable to predict the dynamic features which are in good agreement with the nonlinear TruckSim models. The linear models under low lateral acceleration maneuvers, thus, can be used to design the lateral motion controller and to utilize in the integrated design optimization technique. For the higher lateral acceleration maneuvers, the linear models are not suitable to estimate the dynamic behavior accurately. Hence, the linear models should not be used to design lateral motion controllers and optimization of such systems at higher lateral acceleration (larger than 0.5g) maneuvers. It is expected that the linear models are more effective in terms of computational efficiency compared to nonlinear and highly complicated models.

CHAPTER 5

Driver Model Development

5.1 Introduction

To assess road vehicle directional performance, two types of tests, namely, open-loop and closed-loop, are frequently conducted [75]. In open-loop tests, specific steering inputs are predefined and they are not dependent on the response of the vehicle. These tests can be conducted with high repeatability and they are used for the purpose of characterizing only vehicle responses. In closed-loop tests, a desired vehicle motion or trajectory is achieved by continuously monitoring vehicle response and adjusting steering actions accordingly. Because of the cost and safety concerns, it may not be practical to perform field testing during the concept design phase. Simulation assessment thus may be more practical in certain situations. In past studies on active safety systems for AHVs, the open-loop tests were frequently simulated to evaluate the vehicles' directional performance measures.

The National Highway Traffic Safety Administration (NHTSA) Fishhook test maneuver was modified and simulated to assess the roll stability of an AHV [20]. This open-loop test was originally designed to evaluate the roll stability of light vehicles [34] and it may not be well-suited for determining the RWA ratio, a comprehensive stability measure for AHVs. As mentioned previously, an open-loop test with a prescribed single sine-wave steer input for an AHV with a truck/full-trailer combination was emulated to determine the high-speed RWA ratio of the

AHV. Numerical results indicate that with the same steering input, the truck's trajectory in the baseline case is different from that of the AHV with an ATS system [34]. Numerous numerical experiments demonstrate that using open-loop dynamic simulation, it is difficult to accurately simulate the well-defined single lane-change maneuver defined by SAE J2179 for evaluating the RWA ratio [34]. Thus, in the current research, a driver model will be developed and the closed-loop tests are to be simulated for evaluating AHVs' directional performance under the well-defined test maneuvers. In this research, the closed-loop test maneuvers are simulated to evaluate the AHVs' directional performance.

5.2 Test Maneuvers Emulated

Two test maneuvers, i.e. the 360-degree roundabout path-following defined in the United Kingdom's Road Vehicle Regulation [51] and the high-speed single-lane change specified in SAE J2179 [68], are widely accepted for measuring low-speed PFOT value and high-speed RWA ratio of AHVs, respectively. In each of the maneuvers, the vehicle tested is required to follow a precisely prescribed path at a specified speed and the driver should continuously monitor and adjust steering actions accordingly. In the research, the recommended single lane-change test procedure will be simulated for determining the high-speed RWA ratio. In this simulation, the vehicle is traveling at the speed of 88.0 km/h along a straight path section. Then, a sudden lane-change is conducted. The lateral displacement of the vehicle in the lane-change is 1.46 m. The maneuver emulated during the design process for measuring low-speed PFOT value is based on the 360-degree roundabout test procedure. In this case, the center of tractor front axle is required to travel along a specified path. The vehicle travels at the constant speed of 4.0 km/h. Moreover, a low-speed 90-degree intersection-turn testing maneuver defined in the UK regulation [51] will be emulated.

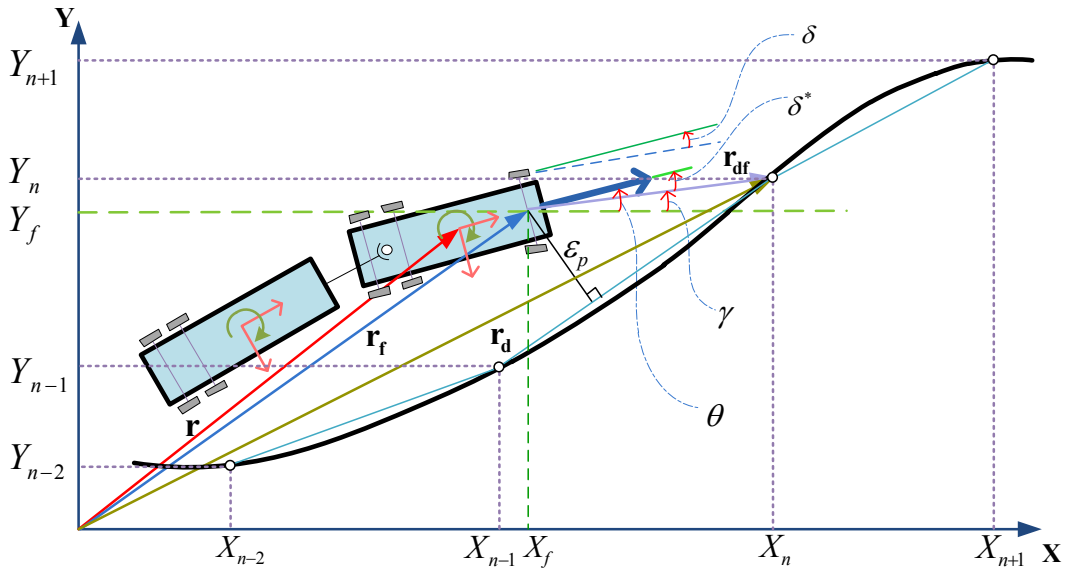

Figure 5.1: Geometry representation of vehicle and prescribed path

5.3 Driver Modeling for Low-Speed Path-Following Simulation

The driver model developed for the research is based on a modified proportional-integral-derivative controller (PID controller) technique. The driver model is to *drive* the virtual vehicle along the prescribed path. The vehicle steering angle correction is made through the PID control of the vehicle position error and angular error. In this research, the driver model position error ε_p is defined as the distance from the tractor's front axle center to the nearest point on the specified path measured along the corresponding radius of curvature. The angular error ε_a is defined as the heading error which is the angle between direction θ of the tractor heading and the direction γ from the front axle center to the target point. The target point is located on the prescribed path and the distance between the target point and the center of the tractor's front axle center is equal to the preview distance.

As shown in Figure 5.1, the prescribed path is defined by a series of point, (X_i, Y_i), $i = 1, 2, ..., m$, in the global coordinate system $X - Y$. The position vectors of the

tractor center of gravity (CG), tractor front axle center and the target point on the path are denoted as $\mathbf{r}$, $\mathbf{r}_f$, and $\mathbf{r}_d$, respectively. In the global coordinate system, these vectors are expressed as

$$\mathbf{r} = X\mathbf{i} + Y\mathbf{j} \tag{5.3.1a}$$

$$\mathbf{r}_f = X_f\mathbf{i} + Y_f\mathbf{j} \tag{5.3.1b}$$

$$\mathbf{r}_d = X_d\mathbf{i} + Y_d\mathbf{j} \tag{5.3.1c}$$

where $\mathbf{i}$ and $\mathbf{j}$ are the unit vectors in the X and Y directions, respectively. If the initial position of tractor center-of-gravity (CG) and the angle swept from the longitudinal axis of the tractor to the X axis are (X_0, Y_0) and θ_0, respectively, the corresponding position of the tractor front axle center (X_{f_0}, Y_{f_0}) can be determined as

$$X_{f_0} = X_0 + a_1 \cos\theta_0 \tag{5.3.2a}$$

$$Y_{f_0} = Y_0 + a_1 \sin\theta_0 \tag{5.3.2b}$$

where, a_1 denotes the longitudinal distance between the tractor CG and the front axle. In the simulation of the low-speed path-following (LSPF) test maneuver, at an arbitrary time instant t, the vehicle position error $\varepsilon_p(t)$, is defined as follows. Assume that at this instant, the position of the truck front axle center is $\Big(X_f(t), Y_f(t)\Big)$, and on the prescribed path the two adjoining points close to the truck front axle center are (X_{n-1}, Y_{n-1}) and (X_n, Y_n). The vehicle position error $\varepsilon_p(t)$ is defined as the distance measured from the point $\Big(X_f(t), Y_f(t)\Big)$ to the straight line connecting the points (X_{n-1}, Y_{n-1}) and (X_n, Y_n).

The desired vehicle heading direction can be represented with the position vector defined by

$$\mathbf{r}_{df}(t) = \mathbf{r}_d(t) - \mathbf{r}_f(t) \tag{5.3.3}$$

The angle swept from vector $\mathbf{r}_{df}(t)$ to X axis is denoted as $\gamma(t)$. The vehicle angular error $\varepsilon_a(t)$ can be determined by

$$\varepsilon_a(t) = \theta(t) - \gamma(t) \tag{5.3.4}$$

where $\theta(t)$ is the yaw angle of the tractor at the time instant t. The vehicle steering angle correction $\delta(t)$ at this instant is defined as

$$\delta(t) = \varepsilon_a(t) \,.\, p(t) \tag{5.3.5}$$

where $p(t)$ is a control variable determined using the following PID control of the vehicle position error.

$$p(t) = K_{pl}\varepsilon_p(t) + K_{il}\int \varepsilon_p(\tau)\mathrm{d}\tau + K_{dl}\frac{\mathrm{d}}{\mathrm{d}t}\varepsilon_p(t) \tag{5.3.6}$$

In Equation (5.3.6), K_{pl}, K_{il} and K_{dl} represent the proportional, integral and derivative controller gains, respectively.

5.4 Driver Modeling for High-Speed Lane Change Simulation

The driver model, constructed using PID control theory, as described in Section 5.3 can also be used in the simulation of high-speed lane-change (HSLC) test maneuver. However, the driver model with PID control algorithm becomes computationally expensive when it is applied to the HSLC simulation. Moreover, the dynamic response, e.g., lateral acceleration time history etc. becomes very spiky. An example of such response is given in Figure 5.2. To avoid these problems, the PID control theory is replaced by a proportional (P) control theory. In this case, only the angular error $\varepsilon_a(t)$ is used to determine the steering angle $\delta(t)$.

Following the same procedure described in the previous section, the angular error $\varepsilon_a(t)$ is determined using equation 5.3.4. The vehicle steering angle correction $\delta(t)$ is defined as

$$\delta(t) = \varepsilon_a(t) \,.\, K_{ph} \tag{5.4.1}$$

where K_{ph} represents the proportional gain of the controller. The preview distance d_{pv} is determined as follows,

$$d_{pv}(t) = \frac{U_1}{t_{pv}} \tag{5.4.2}$$

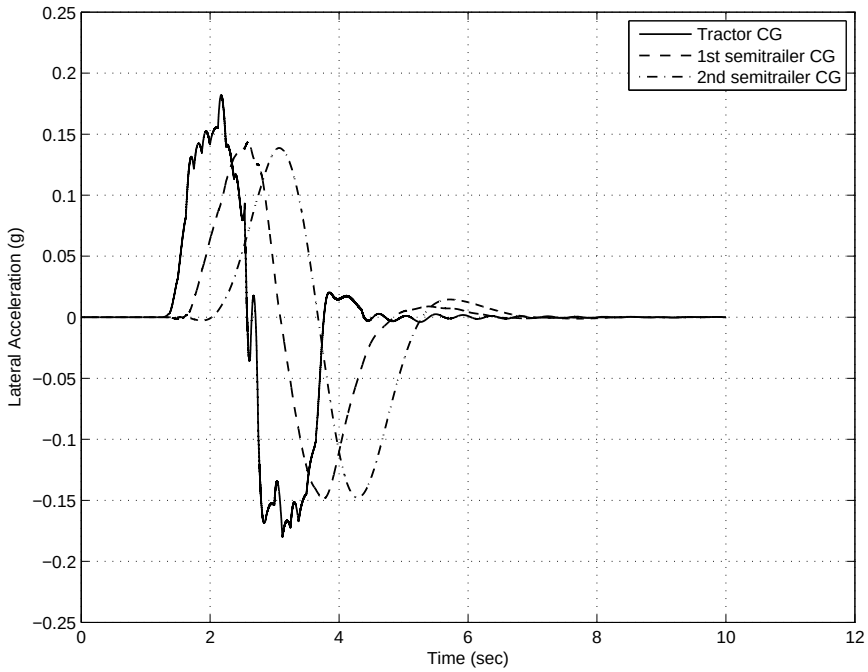

Figure 5.2: An example of spikes in vehicle units' lateral acceleration responses vs. time in a high-speed lane-change maneuver with the driver model constructed using the PID control algorithm

where U_1 and t_{pv} denotes the vehicle forward speed and the preview time, respectively.

5.5 Target Point Updating

With the vehicle steering angle input $\delta(t)$ determined at time t, the differential equation of the vehicle model, as shown in Equation (3.2.3) and (3.3.1), can be solved in the time span t_1 (from time t to time $t + t_1$). The time span from t to $t + t_1$ is divided by a constant time interval denoted as Δt. Throughout the simulation from time t to $t + t_1$, the driver steering input takes the constant value of $\delta(t)$ and does not update its value until the simulation reaches the time $t + t_1$.

When the simulation is performed from time t to time $t + \Delta t$ with the driver steering input $\delta(t)$, the tractor lateral velocity $V_1(t + \Delta t)$ and yaw rate $\omega_1(t + \Delta t)$ can

be determined from the state variable set **x** at time $t + \Delta t$. If the time increment Δt is sufficiently small, the vehicle heading angle increment $\Delta\theta(t)$ can be calculated by

$$\Delta\theta(t) = -\frac{\omega_1(t) + \omega_2(t + \Delta t)}{2} \,.\, \Delta t \tag{5.5.1}$$

Note that the direction of yaw rate and that of vehicle heading angle θ are opposite. Thus, the resulting heading angle at the time instant $t + \Delta t$ is

$$\theta(t + \Delta t) = \theta(t) + \Delta\theta(t) \tag{5.5.2}$$

Over the time interval Δt, the position variation of the tractor CG can be determined using the constant vehicle forward speed U_1 and the instantaneous lateral speed $V_1(t + \Delta t)$ of tractor.

$$X(\Delta t) = U_1 \cos\left(\frac{\theta(t) + \theta(t + \Delta t)}{2}\right)\Delta t + \frac{V_1(t) + V_1(t + \Delta t)}{2}\sin\left(\frac{\theta(t) + \theta(t + \Delta t)}{2}\right)\Delta t \tag{5.5.3a}$$

$$X(\Delta t) = U_1 \sin\left(\frac{\theta(t) + \theta(t + \Delta t)}{2}\right)\Delta t - \frac{V_1(t) + V_1(t + \Delta t)}{2}\cos\left(\frac{\theta(t) + \theta(t + \Delta t)}{2}\right)\Delta t \tag{5.5.3b}$$

Then at the time instant $t + \Delta t$, the position of the tractor CG and its front axle center can be determined by

$$X(t + \Delta t) = X(t) + \Delta X(t) \tag{5.5.4a}$$

$$Y(t + \Delta t) = Y(t) + \Delta Y(t) \tag{5.5.4b}$$

and

$$X_f(t + \Delta t) = X(t + \Delta t) + S_1 \cos\big(\theta(t + \Delta t)\big) \tag{5.5.5a}$$

$$Y_f(t + \Delta t) = Y(t + \Delta t) + S_1 \cos\big(\theta(t + \Delta t)\big) \tag{5.5.5b}$$

respectively. Following the same procedure described above, the simulation is performed until time $t + t_1$ with the driver steering input $\delta(t)$. Then, the vehicle steering angle input $\delta(t + t_1)$ can be determined for the simulation of next time span following the procedure described in Section 5.3 and 5.4 for the LSPF and HSLC simulations, respectively.

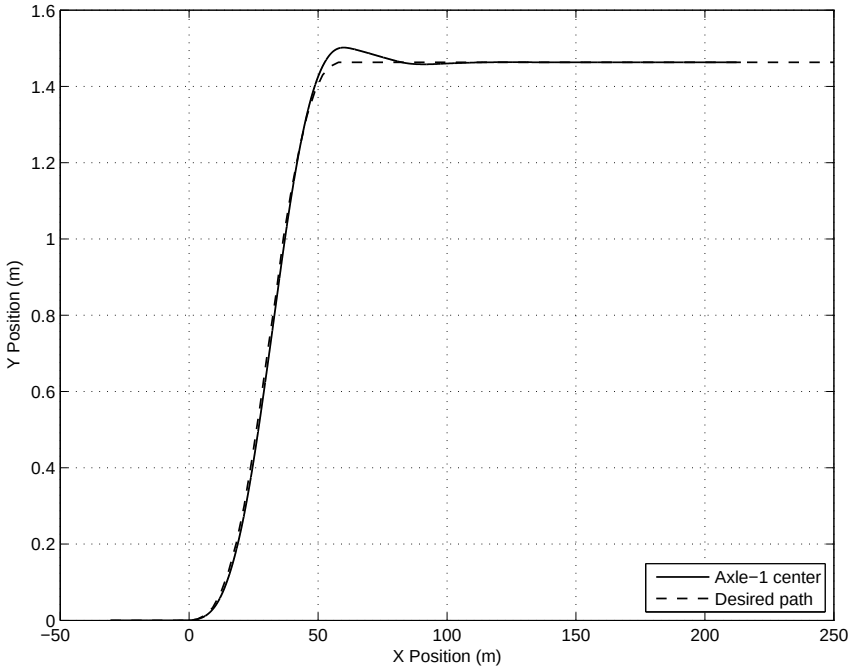

Figure 5.3: Trajectories of the 7 DOF model during the lane change maneuver

5.6 HSLC Driver Model Validation

To validate the developed driver model, it is integrated with the 7 DOF model of the MTAHV with a tractor and two trailers (B-train Double) combination described in Chapter 3. Figure 5.3 shows the simulated trajectories of the tractor front axle (axle-1) center and the prescribed path for the high-speed lane-change (HSLC) test specified in SAE J2179 [68]. The demonstration reveals that the HSLC driver model is effective for following the prescribed path.

5.7 LSPF Driver Model Validation

To validate the LSPF driver model, the simulation is performed for the 7 DOF MTAHV model incorporated with LSPF driver model. Figure 5.4 illustrates the fidelity of the simulated trajectory of the tractor front axle (axle-1) center tracking the prescribed path in the 360-degree roundabout maneuver. A closed observation of the figure reveals and validates that the driver model designed for low-speed

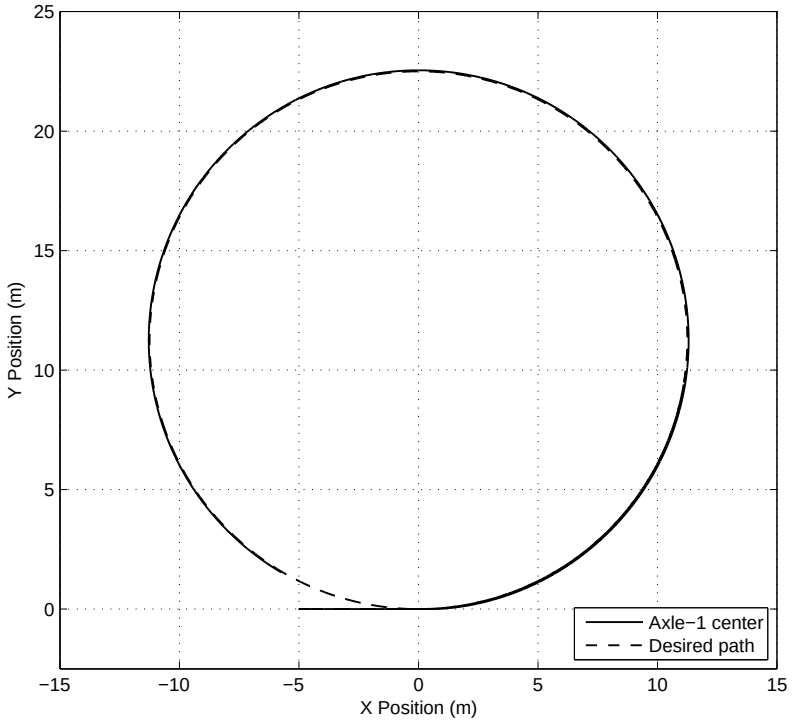

Figure 5.4: Trajectory of passive tractor-semitrailer during 360-degree roundabout

path-following (LSPF) is capable to follow the prescribed path very effectively.

5.8 Sensitivity Analysis

Figure 5.5 and 5.6 show the sensitivity of the positive and the negative peak lateral accelerations at the tractor CG with the variation of the preview time t_{pv} and proportional gain K_{ph} of the HSLC driver model, respectively. A close observation of both figures reveals that with the increase of the proportional gain K_{ph} of the HSLC driver model, the absolute peak value of the lateral acceleration at the trailer CG decreases. On the other hand, the preview time t_{pv}, and thereby, the preview distance d_{pv}, has a certain value where the peak value of the lateral acceleration at the trailer CG has minimum value. Any further increase of the preview time or the distance cause an increase of the peak value of the lateral acceleration.

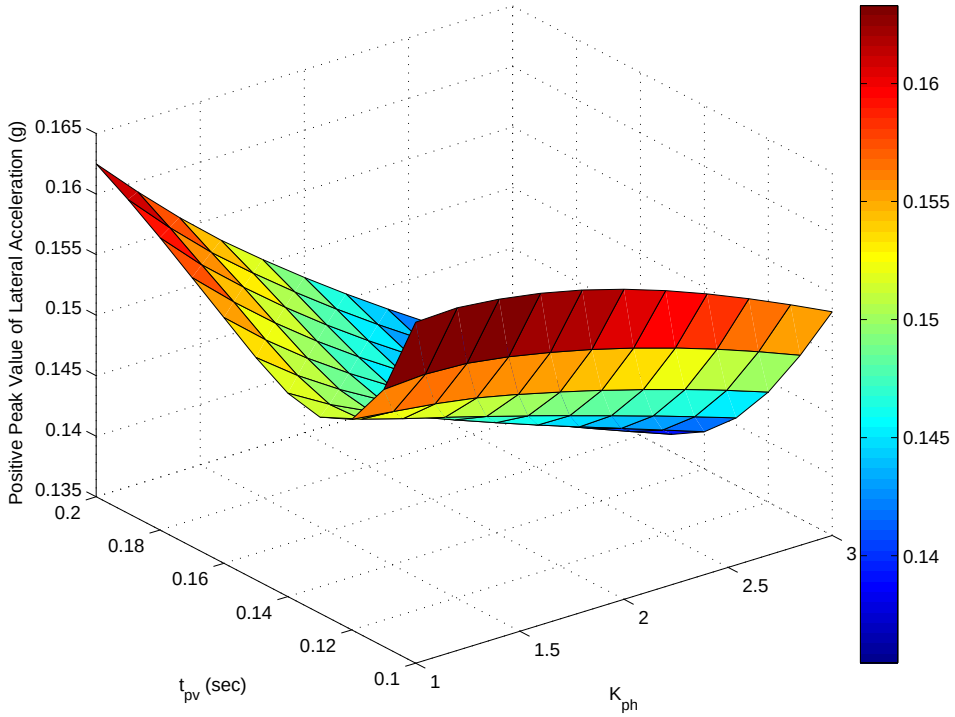

Figure 5.5: Effect of preview the time and the proportional gain variation on the positive peak value of the lateral acceleration in the high-speed lane-change maneuver

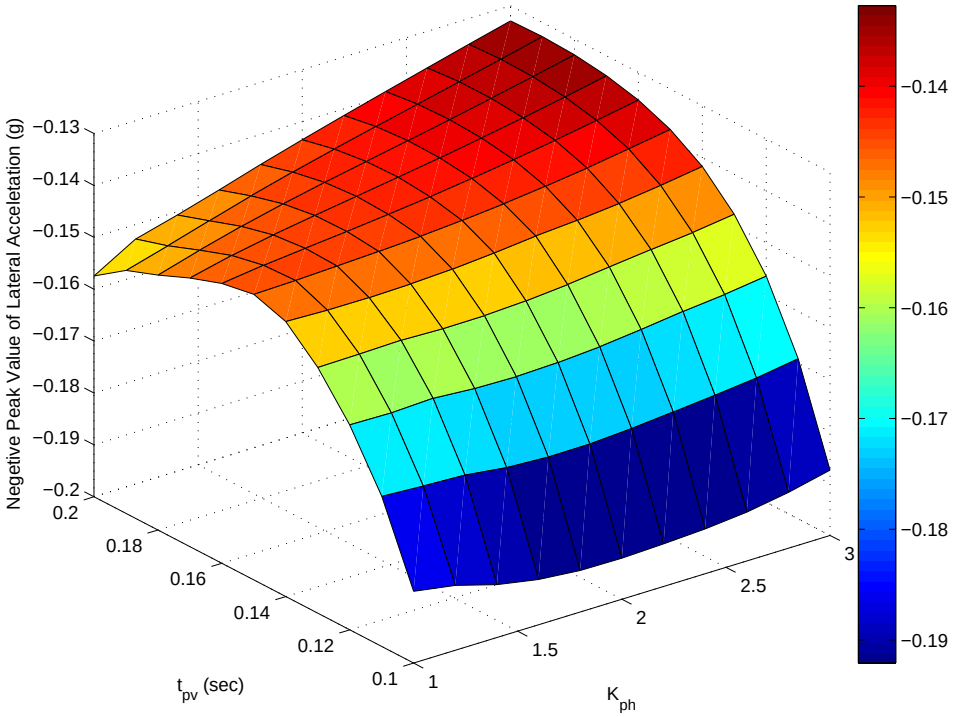

Figure 5.6: Effect of the preview time and the proportional gain variation on the negative peak value of the tractor CG lateral acceleration in the high-speed lane-change maneuver

5.9 Summary

In this chapter, the driver-model for the high-speed lane-change (HSLC) simulation and the driver model for low-speed path-following (LSPF) simulation has been introduced, validated, and the parametric sensitivity analysis has been performed. The simulation results from both the high and low speed test maneuvers indicate that the vehicle model is well-controlled by the driver model and accurately follows the desired paths. Investigation on the HSLC driver model reveals that an increase in proportional gain decreases the peak value of lateral acceleration at the tractor center of gravity.

CHAPTER 6

Control Strategies

6.1 Introduction

In this chapter, different control strategies are investigated for active safety systems the single trailer articulated heavy vehicle (STAHV) and the multi-trailer articulated heavy vehicle (MTAHV). Seven different control approaches are discussed, including, active trailer steering (ATS), differential braking (DB), anti-roll (AR), integrated ATS and AR, integrated ATS and DB, integrated DB and AR, and integrated ATS, DB and AR control.

6.2 Control Goals

Each control strategy has two versions, namely RWA and PFOT mode. The purpose of the RWA mode of the controller is to make the vehicle's rearward amplification (RWA) ratio approach the value of 1.0 in the single lane-change maneuver. The goal of the PFOT mode of controller is to minimize the vehicle's path-following off-tracking (PFOT) value in the 360-degree roundabout (or the 90-degree intersection turn) test.

The two operational controllers, i.e. RWA and PFOT, are designed considering the high- speed (88.0 km/h) single-lane change (HSLC) test maneuver specified in

SAE J2179 and the low-speed (4.0 km/h) path-following (LSPF) 360-degree roundabout (or the 90-degree intersection turn) path-following test procedure, respectively. The controller design is dependent on the vehicle forward speed. Thus, vehicle forward speed is the criterion governing the transition of the two controllers. It is proposed that below 40.0 km/h the PFOT controller should be applied, while above this speed the RWA controller should be operated.

6.3 Control strategies

In this section, different control strategies will be discussed and their relevant cost functions will be constructed for the STAHV. The control strategies are also applicable to the design optimization of the MTAHV with active safety systems.

6.3.1 ATS (Active Trailer Steering) control

The linear quadratic regulator (LQR) controller has two versions, namely RWA and PFOT. The objective of the RWA controller is to make the vehicle's RWA ratio approach the value of 1.0 in the single lane change maneuver; the goal of the PFOT controller is to minimize the vehicle's PFOT value in the 360-degree roundabout (or the 90-degree intersection turn) test.

The two operational controllers, i.e. RWA and PFOT, are designed considering the high-speed (88.0 km/h) single-lane change test maneuver specified in SAE J2179 and the low-speed (4.0 km/h) 360-degree roundabout (or the 90-degree intersection turn) path-following test procedure, respectively. The controller designs are vehicle forward speed dependent. Thus, vehicle forward speed is the criterion governing the transition of the two controllers. It is proposed that below 40.0 km/h the PFOT controller is applied, while above this speed the RWA controller is operated.

6.3.1.1 *RWA mode of the ATS controller*

As shown in Figure 3.1, the axles of the semitrailer are designed to be steerable and the steering angles δ_{2f} and δ_{2r} are determined by the optimal controller based on the linear quadratic regulator (LQR) control strategy [11]. The LQR controller design alone is an optimization problem of minimizing the performance index. In the RWA controller design, the performance index takes the following form

$$\begin{aligned} J_{RWA} = \int_0^\infty \Bigg[& q_{RWA1} \left(U_1(\dot{\beta}_1 + \dot{\psi}_1) - \frac{m_{s1}}{m_1} (h_{s1} - h_{r1}) \ddot{\phi}_1 \right)^2 \\ & + q_{RWA2} \left(U_2(\dot{\beta}_2 + \dot{\psi}_2) - \frac{m_{s2}}{m_2} (h_{s2} - h_{r2}) \ddot{\phi}_2 \right)^2 \\ & + q_{RWA3}\delta_{f2}^2 + q_{RWA4}\delta_{r2}^2 \Bigg] \, dt \end{aligned} \tag{6.3.1}$$

subject to equation (6.3.2).

$$\dot{\mathbf{x}} = \mathbf{A}\mathbf{x} + \mathbf{B_1}\mathbf{u} + \mathbf{B}\delta_{1f} \tag{6.3.2}$$

By solving the algebraic Riccati equation, the solution of the optimization problem is the control vector of the form

$$\mathbf{u} = -\mathbf{K}_{RWA}\mathbf{x} \tag{6.3.3}$$

where $\mathbf{K}_{RWA}$ is the control matrix with a dimension of 2×10; $\mathbf{x}$ and $\mathbf{u}$ are the state and control variable vectors defined by equations (3.2.4) and (6.3.4), respectively.

$$\mathbf{u} = \begin{bmatrix} \delta_{2f} & \delta_{2r} \end{bmatrix}^T. \tag{6.3.4}$$

In equation (6.3.1), q_{RWAi}, where $i = 1, 2, \ldots, 4$, are weighting factors that impose penalties upon the magnitude and duration of the lateral acceleration at the tractor center of gravity (CG), $U_1(\dot{\beta}_1 + \dot{\psi}_1) - \frac{m_{s1}}{m_1} (h_{s1} - h_{r1}) \ddot{\phi}_1$, the lateral acceleration at the trailer CG, $U_2(\dot{\beta}_2 + \dot{\psi}_2) - \frac{m_{s2}}{m_2} (h_{s2} - h_{r2}) \ddot{\phi}_2$, and active steering angles, δ_{2f} and δ_{2r}, respectively. Note that the third and the fourth terms on the right hand side of equation (6.3.1) represents the energy consumption of the ATS system for the AHV with a tractor and semitrailer combination.

In the design of the LQR controller, it is intended to meet the seventh design criterion: minimizing power consumption. Note that the design criterion will be further discussed in section 7.3, by means of minimizing the performance index shown in equation (6.3.1). The weighting factor vector $\begin{bmatrix} q_{RWA1} & q_{RWA2} & \dots & q_{RWA4} \end{bmatrix}^T$ corresponds to the RWA controller parameters $\mathbf{X}_{RWA}$ in section 7.4.

6.3.1.2 *PFOT mode of the ATS controller*

In the PFOT controller design, on the other hand, the performance index takes the following form

$$\begin{aligned} J_{PFOT} = \int_0^\infty \Big[& q_{PFOT1}\phi_1^2 + q_{PFOT2}\dot{\phi}_1^2 + q_{PFOT3}\beta_1^2 + q_{PFOT4}\dot{\psi}_1^2 + q_{PFOT5}\phi_2^2 + q_{PFOT6}\dot{\phi}_2^2 \\ & + q_{PFOT7}\beta_2^2 + q_{PFOT8}\dot{\psi}_2^2 + q_{PFOT9}\phi_{1t}^2 + q_{PFOT10}\phi_{2t}^2 + q_{PFOT11}\delta_{f2}^2 \\ & + q_{PFOT12}\delta_{r2}^2 \Big] \, dt \end{aligned} \tag{6.3.5}$$

subject to equation (6.3.2). Since, at low speeds, the lateral accelerations at tractor and trailer CG are negligible, in construction of the performance index of the PFOT controller, the acceleration terms are ignored. By solving the algebraic Riccati equation, the solution of the optimization problem is the control vector of the form

$$\mathbf{u} = -\mathbf{K}_{PFOT}\mathbf{x} \tag{6.3.6}$$

where $\mathbf{K}_{PFOT}$ is the control matrix with a dimension of 2×10; $\mathbf{x}$ and $\mathbf{u}$ are the state and control variable vectors defined by equations (3.2.4) and (6.3.4), respectively. In equation (6.3.5), q_{PFOTi}, where $i = 1, 2, \dots, 12$, are weighting factors that impose penalties upon the each state valuables of state vector $\mathbf{x}$ defined by equations (3.2.4). The weighting factor vector $\begin{bmatrix} q_{PFOT1} & q_{PFOT2} & \dots & q_{PFOT12} \end{bmatrix}^T$ corresponding controller parameters $\mathbf{X}_{PFOT}$.

6.3.2 DB (Differential Braking) control

As shown in Figure 3.1, the active yaw moments, i.e. M_1 and M_2 resulting from the differential braking (DB) system, are applied to the tractor and semitrailer, respectively. The active yaw moments M_1 and M_2 are determined by the optimal controller based on the linear quadratic regulator (LQR) control strategy [11]. As mentioned before, the LQR controller design itself is an optimization problem, minimizing the performance index.

6.3.2.1 *RWA mode of the DB controller*

In the RWA controller design, the performance index takes the following form

$$J_{RWA} = \int_0^\infty \left[q_{RWA1} \left(U_1(\dot{\beta}_1 + \dot{\psi}_1) - \frac{m_{s1}}{m_1} (h_{s1} - h_{r1}) \ddot{\phi}_1 \right)^2 + q_{RWA2} \left(U_2(\dot{\beta}_2 + \dot{\psi}_2) - \frac{m_{s2}}{m_2} (h_{s2} - h_{r_2}) \ddot{\phi}_2 \right)^2 + q_{RWA3} M_1^2 + q_{RWA4} M_2^2 \right] dt \tag{6.3.7}$$

subject to equation (6.3.8).

$$\dot{\mathbf{x}} = \mathbf{A}\mathbf{x} + \mathbf{B_2}\mathbf{u} + \mathbf{B}\delta_{1f} \tag{6.3.8}$$

By solving the algebraic Riccati equation, the solution of the optimization problem is the control vector of the form of equation (6.3.3), where $\mathbf{K}_{RWA}$ is the control matrix with a dimension of 2×10; $\mathbf{x}$ and $\mathbf{u}$ are the state and control variable vectors defined by equations (3.2.4) and (6.3.9), respectively.

$$\mathbf{u} = \begin{bmatrix} M_1 & M_2 \end{bmatrix}^T. \tag{6.3.9}$$

In equation (6.3.7), q_{RWAi}, where $i = 1, 2, \ldots, 4$, are weighting factors that impose penalties upon the magnitude and duration of the lateral acceleration at the tractor center of gravity (CG), $U_1(\dot{\beta}_1 + \dot{\psi}_1) - \frac{m_{s1}}{m_1} (h_{s1} - h_{r1}) \ddot{\phi}_1$, the lateral acceleration at the trailer CG, $U_2(\dot{\beta}_2 + \dot{\psi}_2) - \frac{m_{s2}}{m_2} (h_{s2} - h_{r2}) \ddot{\phi}_2$, and the yaw moment torques, M_1 and M_2, respectively. Note that the third and fourth terms on the right hand side of equation (6.3.7) represent the energy consumption of the DB system.

6.3.2.2 *PFOT mode of the DB controller*

On the other hand, in the PFOT controller design, the performance index takes the following form

$$J_{PFOT} = \int_0^\infty \Big[q_{PFOT1}\phi_1^2 + q_{PFOT2}\dot{\phi}_1^2 + q_{PFOT3}\beta_1^2 + q_{PFOT4}\dot{\psi}_1^2 + q_{PFOT5}\phi_2^2 + q_{PFOT6}\dot{\phi}_2^2 + q_{PFOT7}\beta_2^2 + q_{PFOT8}\dot{\psi}_2^2 + q_{PFOT9}\phi_{1t}^2 + q_{PFOT10}\phi_{2t}^2 + q_{PFOT11}M_1^2 + q_{PFOT12}M_2^2 \Big]\, dt \tag{6.3.10}$$

subject to equation (6.3.8). Since, at the low speeds, the lateral accelerations at tractor and trailer CG are negligible, in construction of the performance index of the PFOT controller, the acceleration terms are ignored. By solving the algebraic Riccati equation, the solution of the optimization problem is the control vector of the form of equation (6.3.6), where $\mathbf{K}_{PFOT}$ is the control matrix with a dimension of 2×10, $\mathbf{x}$ and $\mathbf{u}$ are the state and control variable vectors defined by equations (3.2.4) and (6.3.9), respectively. In equation (6.3.10), q_{PFOTi}, where $i = 1, 2, \ldots, 12$, are weighting factors that impose penalties upon the each state valuables of state vector $\mathbf{x}$ defined by equations (3.2.4).

6.3.3 AR (Anti-Roll) control

As described in Figure 3.1, the active anti-roll bar moments, u_{c1} and u_{c2}, are applied to the tractor and semitrailer, respectively. Note that each of the axles of the tractor and that of the semitrailer are considered as a single body, which is permitted for its roll motion. The active roll moments, u_{c1} and u_{c2}, are determined by the optimal controller based on the linear quadratic regulator (LQR) control strategy.

6.3.3.1 *RWA mode of the AR controller*

In the RWA controller design, the performance index is designed as follows

$$J_{RWA} = \int_0^\infty \left[q_{RWA1} \left(U_1(\dot{\beta}_1 + \dot{\psi}_1) - \frac{m_{s1}}{m_1} (h_{s1} - h_{r1}) \ddot{\phi}_1 \right)^2 + q_{RWA2} \left(U_2(\dot{\beta}_2 + \dot{\psi}_2) - \frac{m_{s2}}{m_2} (h_{s2} - h_{r_2}) \ddot{\phi}_2 \right)^2 + q_{RWA3} u_{c1}^2 + q_{RWA4} u_{c2}^2 \right] dt \tag{6.3.11}$$

subject to equation (6.3.12).

$$\dot{\mathbf{x}} = \mathbf{A}\mathbf{x} + \mathbf{B_3}\mathbf{u} + \mathbf{B}\delta_{1f} \tag{6.3.12}$$

By solving the algebraic Riccati equation, the solution of the optimization problem is the control vector of the form of equation (6.3.3), where $\mathbf{K}_{RWA}$ is the control matrix with a dimension of 2×10, $\mathbf{x}$ and $\mathbf{u}$ are the state and control variable vectors defined by equations (3.2.4) and (6.3.13), respectively.

$$\mathbf{u} = \begin{bmatrix} u_{c1} & u_{c2} \end{bmatrix}^T. \tag{6.3.13}$$

In equation (6.3.11), q_{RWAi}, where $i = 1, 2, \ldots, 4$, are weighting factors that impose penalties upon the magnitude and duration of the lateral acceleration at the tractor center of gravity (CG), $U_1(\dot{\beta}_1 + \dot{\psi}_1) - \frac{m_{s1}}{m_1} (h_{s1} - h_{r1}) \ddot{\phi}_1$, the lateral acceleration at the trailer CG, $U_2(\dot{\beta}_2 + \dot{\psi}_2) - \frac{m_{s2}}{m_2} (h_{s2} - h_{r2}) \ddot{\phi}_2$, and the anti-roll torques, u_{c1} and u_{c2}, respectively. Note that the third and the fourth terms on the right hand side of equation (6.3.11) represent the energy consumption of the AR system.

6.3.3.2 *PFOT mode of the AR controller*

On the other hand, in the PFOT controller design, the performance index takes the following form

$$J_{PFOT} = \int_0^\infty \Big[q_{PFOT1}\phi_1^2 + q_{PFOT2}\dot{\phi}_1^2 + q_{PFOT3}\beta_1^2 + q_{PFOT4}\dot{\psi}_1^2 + q_{PFOT5}\phi_2^2 + q_{PFOT6}\dot{\phi}_2^2 + q_{PFOT7}\beta_2^2 + q_{PFOT8}\dot{\psi}_2^2 + q_{PFOT9}\phi_{1t}^2 + q_{PFOT10}\phi_{2t}^2 + q_{PFOT11}u_{c1}^2 + q_{PFOT12}u_{c2}^2 \Big] dt \tag{6.3.14}$$

subject to equation (6.3.12). Since, at the low speeds, the lateral accelerations at the tractor and trailer CG are negligible, in the design of the performance index of the PFOT controller, the acceleration terms are ignored. By solving the algebraic Riccati equation, the solution of the optimization problem is the control vector of the form of equation (6.3.6), where $\mathbf{K}_{PFOT}$ is the control matrix with a dimension of 2×10, $\mathbf{x}$ and $\mathbf{u}$ are the state and control variable vectors defined by equations (3.2.4) and (6.3.13), respectively. In equation (6.3.14), q_{PFOTi}, where $i = 1, 2, \ldots, 12$, are weighting factors that impose penalties upon the each state valuables of state vector $\mathbf{x}$ defined by equations (3.2.4).

6.3.4 Integrated ATS and AR control

In this control strategy, the active trailer steering (ATS) and anti-roll (AR) systems are combined. In this proposed integrated system, the trailer axles are steerable and active steering angles are δ_{2f} and δ_{2r} for the trailer axles. The active control variables, δ_{2f}, δ_{2r}, u_{c1}, and u_{c2} are also applied to the tractor and semitrailer, respectively.

6.3.4.1 *RWA mode of the Integrated ATS and AR controller*

As mentioned in section 6.3.3, the axles of tractor and that of semitrailer are considered as a single body which has roll motion. The active roll moments, u_{c1} and u_{c2}, are determined by the optimal controller based on the linear quadratic regulator (LQR) control strategy.

In the RWA controller design, the performance index is designed as follows

$$\begin{aligned} J_{RWA} = \int_0^\infty \Bigg[& q_{RWA1} \left(U_1(\dot{\beta}_1 + \dot{\psi}_1) - \frac{m_{s1}}{m_1} \left(h_{s1} - h_{r1}\right) \ddot{\phi}_1 \right)^2 \\ & + q_{RWA2} \left(U_2(\dot{\beta}_2 + \dot{\psi}_2) - \frac{m_{s2}}{m_2} \left(h_{s2} - h_{r_2}\right) \ddot{\phi}_2 \right)^2 \\ & + q_{RWA3}\delta_{f2}^2 + q_{RWA4}\delta_{r2}^2 + q_{RWA5}u_{c1}^2 + q_{RWA6}u_{c2}^2 \Bigg] \, dt \end{aligned} \tag{6.3.15}$$

subject to equation (6.3.16).

$$\dot{\mathbf{x}} = \mathbf{A}\mathbf{x} + \mathbf{B_4}\mathbf{u} + \mathbf{B}\delta_{1f} \tag{6.3.16}$$

By solving the algebraic Riccati equation, the solution of the optimization problem is the control vector of the form of equation (6.3.3), where $\mathbf{K}_{RWA}$ is the control matrix with a dimension of 4×10, $\mathbf{x}$ and $\mathbf{u}$ are the state and control variable vectors defined by equations (3.2.4) and (6.3.17), respectively.

$$\mathbf{u} = \begin{bmatrix} \delta_{2f} & \delta_{2r} & u_{c1} & u_{c2} \end{bmatrix}^T. \tag{6.3.17}$$

In equation (6.3.15), q_{RWAi}, where $i = 1, 2, \ldots, 6$, are weighting factors that impose penalties upon the magnitude and duration of the lateral acceleration at the tractor center of gravity (CG), $U_1(\dot{\beta}_1 + \dot{\psi}_1) - \frac{m_{s1}}{m_1}(h_{s1} - h_{r1})\ddot{\phi}_1$; the lateral acceleration at the trailer CG, $U_2(\dot{\beta}_2 + \dot{\psi}_2) - \frac{m_{s2}}{m_2}(h_{s2} - h_{r2})\ddot{\phi}_2$; the active steering angles, δ_{2f} and δ_{2r}; and the anti-roll torques, u_{c1} and u_{c2}, respectively. Note that the third to the sixth terms on the right hand side of equation (6.3.15) represent the energy consumption of the integrated control system.

6.3.4.2 *PFOT mode of the Integrated ATS and AR controller*

On the other hand, in the PFOT controller design, the performance index takes the following form

$$\begin{aligned} J_{PFOT} = \int_0^\infty \Big[& q_{PFOT1}\phi_1^2 + q_{PFOT2}\dot{\phi}_1^2 + q_{PFOT3}\beta_1^2 + q_{PFOT4}\dot{\psi}_1^2 + q_{PFOT5}\phi_2^2 + q_{PFOT6}\dot{\phi}_2^2 \\ & + q_{PFOT7}\beta_2^2 + q_{PFOT8}\dot{\psi}_2^2 + q_{PFOT9}\phi_{1t}^2 + q_{PFOT10}\phi_{2t}^2 + q_{PFOT11}\delta_{f2}^2 \\ & + q_{PFOT12}\delta_{r2}^2 + q_{PFOT13}u_{c1}^2 + q_{PFOT14}u_{c2}^2 \Big]\, dt \end{aligned} \tag{6.3.18}$$

subject to equation (6.3.16). Since, at the low speeds, the lateral accelerations at tractor and trailer CG are negligible, in design of the performance index of the PFOT controller, the acceleration terms are ignored. By solving the algebraic Riccati equation, the solution of the optimization problem is the control vector of the form of equation (6.3.6), where $\mathbf{K}_{PFOT}$ is the control matrix with a dimension of 4×10, $\mathbf{x}$ and $\mathbf{u}$ are the state and control variable vectors defined by equations

(3.2.4) and (6.3.17), respectively. In equation (6.3.18), q_{PFOTi}, where $i = 1, 2, \ldots, 14$, are weighting factors that impose penalties upon the each state valuables of state vector **x** defined by equations (3.2.4).

6.3.5 Integrated ATS and DB control

In this control technique, the active trailer steering (ATS) and differential braking (DB) systems are combined. In this integrated system, the trailer axles are steerable and active steering angles are δ_{2f} and δ_{2r}. The active yaw moments M_1 and M_2 are also applied to the tractor and semitrailer, respectively. As mentioned in section 6.3.3, the axles of tractor and that of semitrailer are considered as a single body which has roll motion. The active control variables δ_{2f}, δ_{2r}, M_1, and M_2 are determined by the optimal controller based on the linear quadratic regulator (LQR) control strategy.

6.3.5.1 *RWA mode of the Integrated ATS and DB controller*

In the RWA controller design, the performance index is designed as follows

$$\begin{aligned} J_{RWA} = \int_0^\infty \Bigg[& q_{RWA1} \left(U_1(\dot{\beta}_1 + \dot{\psi}_1) - \frac{m_{s1}}{m_1} \left(h_{s1} - h_{r1}\right) \ddot{\phi}_1 \right)^2 \\ & + q_{RWA2} \left(U_2(\dot{\beta}_2 + \dot{\psi}_2) - \frac{m_{s2}}{m_2} \left(h_{s2} - h_{r_2}\right) \ddot{\phi}_2 \right)^2 \\ & + q_{RWA3}\delta_{f2}^2 + q_{RWA4}\delta_{r2}^2 + q_{RWA5}M_1^2 + q_{RWA6}M_2^2 \Bigg] \, dt \end{aligned} \tag{6.3.19}$$

subject to equation (6.3.20).

$$\dot{\mathbf{x}} = \mathbf{A}\mathbf{x} + \mathbf{B_5}\mathbf{u} + \mathbf{B}\delta_{1f} \tag{6.3.20}$$

By solving the algebraic Riccati equation, the solution of the optimization problem is the control vector of the form of equation (6.3.3), where $\mathbf{K}_{RWA}$ is the control matrix with a dimension of 4×10, **x** and **u** are the state and control variable vectors defined by equations (3.2.4) and (6.3.21), respectively.

$$\mathbf{u} = \begin{bmatrix} \delta_{2f} & \delta_{2r} & M_1 & M_2 \end{bmatrix}^T. \tag{6.3.21}$$

In equation (6.3.19), q_{RWAi}, where $i = 1, 2, \ldots, 6$, are weighting factors that impose penalties upon the magnitude and duration of the lateral acceleration at the tractor center of gravity (CG), $U_1(\dot{\beta}_1 + \dot{\psi}_1) - \frac{m_{s1}}{m_1}(h_{s1} - h_{r1})\ddot{\phi}_1$; the lateral acceleration at the trailer CG, $U_2(\dot{\beta}_2 + \dot{\psi}_2) - \frac{m_{s2}}{m_2}(h_{s2} - h_{r2})\ddot{\phi}_2$; the active steering angles, δ_{2f} and δ_{2r}; and the anti-roll torques, u_{c1} and u_{c2}, respectively. Note that the third to sixth terms on the right hand side of equation (6.3.19) represent the energy consumption of the integrated control system.

6.3.5.2 *PFOT mode of Integrated ATS and DB controller*

On the other hand, in the PFOT controller design, the performance index takes the following form

$$J_{PFOT} = \int_0^\infty \Big[q_{PFOT1}\phi_1^2 + q_{PFOT2}\dot{\phi}_1^2 + q_{PFOT3}\beta_1^2 + q_{PFOT4}\dot{\psi}_1^2 + q_{PFOT5}\phi_2^2 + q_{PFOT6}\dot{\phi}_2^2 + q_{PFOT7}\beta_2^2 + q_{PFOT8}\dot{\psi}_2^2 + q_{PFOT9}\phi_{1t}^2 + q_{PFOT10}\phi_{2t}^2 + q_{PFOT11}\delta_{f2}^2 + q_{PFOT12}\delta_{r2}^2 + q_{PFOT13}M_1^2 + q_{PFOT14}M_2^2 \Big] dt \tag{6.3.22}$$

subject to equation (6.3.20). Since, at the low speeds, the lateral accelerations at tractor and trailer CG are negligible, in design of the performance index of the PFOT controller, the acceleration terms are ignored. By solving the algebraic Riccati equation, the solution of the optimization problem is the control vector of the form of equation (6.3.6), where $\mathbf{K}_{PFOT}$ is the control matrix with a dimension of 4×10, $\mathbf{x}$ and $\mathbf{u}$ are the state and control variable vectors defined by equations (3.2.4) and (6.3.21), respectively. In equation (6.3.22), q_{PFOTi}, where $i = 1, 2, \ldots, 14$, are weighting factors that impose penalties upon the each state valuables of state vector $\mathbf{x}$ defined by equations (3.2.4).

6.3.6 Integrated AR and BD control

In this control technique, the anti roll (AR) and differential braking (DB) systems are combined. In this integrated system, the active anti-roll bar moments, i.e. u_{c1} and u_{c2}, are applied to tractor and trailer, respectively. The active yaw moments, M_1 and M_2, are also applied to the axles of tractor and semitrailer, respectively.

As mentioned in section 6.3.3, the axles of tractor and that of semitrailer are considered as a single body which has roll motion. The active variables u_{c1}, u_{c2}, M_1 and M_2 are determined by the optimal controller based on the linear quadratic regulator (LQR) control strategy.

6.3.6.1 *RWA mode of the Integrated AR and DB controller*

In the RWA controller design, the performance index is designed as follows

$$\begin{aligned} J_{RWA} = \int_0^\infty \Bigg[& q_{RWA1} \left(U_1(\dot{\beta}_1 + \dot{\psi}_1) - \frac{m_{s1}}{m_1} \left(h_{s1} - h_{r1}\right) \ddot{\phi}_1 \right)^2 \\ & + q_{RWA2} \left(U_2(\dot{\beta}_2 + \dot{\psi}_2) - \frac{m_{s2}}{m_2} \left(h_{s2} - h_{r_2}\right) \ddot{\phi}_2 \right)^2 \\ & + q_{RWA3} M_1^2 + q_{RWA4} M_2^2 + q_{RWA5} u_{c1}^2 + q_{RWA6} u_{c2}^2 \Bigg] \, dt \end{aligned} \tag{6.3.23}$$

subject to equation (6.3.24).

$$\dot{\mathbf{x}} = \mathbf{A}\mathbf{x} + \mathbf{B_6}\mathbf{u} + \mathbf{B}\delta_{1f} \tag{6.3.24}$$

By solving the algebraic Riccati equation, the solution of the optimization problem is the control vector of the form of equation (6.3.3), where $\mathbf{K}_{RWA}$ is the control matrix with a dimension of 4×10, $\mathbf{x}$ and $\mathbf{u}$ are the state and control variable vectors defined by equations (3.2.4) and (6.3.25), respectively.

$$\mathbf{u} = \begin{bmatrix} u_{c1} & u_{c2} & M_1 & M_2 \end{bmatrix}^T. \tag{6.3.25}$$

In equation (6.3.23), q_{RWAi}, where $i = 1, 2, \ldots, 6$, are weighting factors that impose penalties upon the magnitude and duration of the lateral acceleration at the tractor center of gravity (CG), $U_1(\dot{\beta}_1 + \dot{\psi}_1) - \frac{m_{s1}}{m_1}\left(h_{s1} - h_{r1}\right)\ddot{\phi}_1$; the lateral acceleration at the trailer CG, $U_2(\dot{\beta}_2 + \dot{\psi}_2) - \frac{m_{s2}}{m_2}\left(h_{s2} - h_{r2}\right)\ddot{\phi}_2$; the active roll moments M_1 and M_2; and the anti-roll torques, u_{c1} and u_{c2}, respectively. Note that the third to the sixth terms on the right hand side of equation (6.3.23) represent the energy consumption of the integrated control system.

6.3.6.2 *PFOT mode of the Integrated AR and DB controller*

On the other hand, in the PFOT controller design, the performance index takes the following form

$$J_{PFOT} = \int_0^\infty \Big[q_{PFOT1}\phi_1^2 + q_{PFOT2}\dot{\phi}_1^2 + q_{PFOT3}\beta_1^2 + q_{PFOT4}\dot{\psi}_1^2 + q_{PFOT5}\phi_2^2 + q_{PFOT6}\dot{\phi}_2^2 + q_{PFOT7}\beta_2^2 + q_{PFOT8}\dot{\psi}_2^2 + q_{PFOT9}\phi_{1t}^2 + q_{PFOT10}\phi_{2t}^2 + q_{PFOT11}M_1^2 + q_{PFOT12}M_2^2 + q_{PFOT13}u_{c1}^2 + q_{PFOT14}u_{c2}^2 \Big] dt \tag{6.3.26}$$

subject to equation (6.3.24). Since, at the low speeds, the lateral accelerations at tractor and trailer CG are negligible, in design of the performance index of the PFOT controller, the acceleration terms are ignored. By solving the algebraic Riccati equation, the solution of the optimization problem is the control vector of the form of equation (6.3.6), where $\mathbf{K}_{PFOT}$ is the control matrix with a dimension of 4×10, $\mathbf{x}$ and $\mathbf{u}$ are the state and control variable vectors defined by equations (3.2.4) and (6.3.25), respectively. In equation (6.3.26), q_{PFOTi}, where $i = 1, 2, \ldots, 14$, are weighting factors that impose penalties upon the each state valuables of state vector $\mathbf{x}$ defined by equation (3.2.4).

6.3.7 Integrated ATS, AR and DB control

In this control technique, the active trailer steering (ATS), active roll (AR) and differential braking (DB) systems are combined. In this integrated system, the trailer axles are steerable and active steering angles are δ_{2f} and δ_{2r}. The active anti-roll bar moments, u_{c1} and u_{c2}, are applied to the tractor and semitrailer, respectively. Also the active yaw moments, M_1 and M_2, are also applied to the tractor and semitrailer, respectively. As mentioned in section 6.3.3, the axles of tractor and that of semitrailer are considered as a single body which has roll motion. The active variables δ_{2f}, δ_{2r}, u_{c1}, u_{c2}, M_1, and M_2 are determined by the optimal controller based on the linear quadratic regulator (LQR) control strategy.

6.3.7.1 *RWA mode of the Integrated ATS, AR and DB controller*

In the RWA controller design, the performance index is designed as follows

$$J_{RWA} = \int_0^\infty \Bigg[q_{RWA1} \left(U_1(\dot{\beta}_1 + \dot{\psi}_1) - \frac{m_{s1}}{m_1} \left(h_{s1} - h_{r1}\right) \ddot{\phi}_1 \right)^2 + q_{RWA2} \left(U_2(\dot{\beta}_2 + \dot{\psi}_2) - \frac{m_{s2}}{m_2} \left(h_{s2} - h_{r_2}\right) \ddot{\phi}_2 \right)^2 + q_{RWA3}\delta_{f2}^2 + q_{RWA4}\delta_{r2}^2 + q_{RWA5}M_1^2 + q_{RWA6}M_2^2 + q_{RWA7}u_{c1}^2 + q_{RWA8}u_{c2}^2 \Bigg] \, dt \tag{6.3.27}$$

subject to equation (6.3.28).

$$\dot{\mathbf{x}} = \mathbf{A}\mathbf{x} + \mathbf{B_7}\mathbf{u} + \mathbf{B}\delta_{1f} \tag{6.3.28}$$

By solving the algebraic Riccati equation, the solution of the optimization problem is the control vector of the form of equation (6.3.3), where $\mathbf{K}_{RWA}$ is the control matrix with a dimension of 6×10, $\mathbf{x}$ and $\mathbf{u}$ are the state and control variable vectors defined by equations (3.2.4) and (6.3.29), respectively.

$$\mathbf{u} = \begin{bmatrix} \delta_{2f} & \delta_{2r} & u_{c1} & u_{c2} & M_1 & M_2 \end{bmatrix}^T. \tag{6.3.29}$$

In equation (6.3.27), q_{RWAi}, where $i = 1, 2, \ldots, 8$, are weighting factors that impose penalties upon the magnitude and duration of the lateral acceleration at the tractor center of gravity (CG), $U_1(\dot{\beta}_1 + \dot{\psi}_1) - \frac{m_{s1}}{m_1}\left(h_{s1} - h_{r1}\right)\ddot{\phi}_1$; the lateral acceleration at the trailer CG, $U_2(\dot{\beta}_2 + \dot{\psi}_2) - \frac{m_{s2}}{m_2}\left(h_{s2} - h_{r2}\right)\ddot{\phi}_2$; the active steering angles, δ_{2f} and δ_{2r}; the anti-roll torques, u_{c1} and u_{c2}; the active yaw moments M_1 and M_2, respectively. Note that from third to the eighth terms on the right hand side of equation (6.3.27) represent the energy consumption of the integrated control system.

Similarly, the LQR cost function for the MTAHV for the RWA mode of the inte-

grated ATS, AR and DB controller can be constructed as follows,

$$J_{RWA} = \int_0^\infty \Bigg[q_{RWA1} \left(U_1(\dot{\beta}_1 + \dot{\psi}_1) - \frac{m_{s1}}{m_1} (h_{s1} - h_{r1}) \ddot{\phi}_1 \right)^2 + q_{RWA2} \left(U_2(\dot{\beta}_2 + \dot{\psi}_2) - \frac{m_{s2}}{m_2} (h_{s2} - h_{r_2}) \ddot{\phi}_2 \right)^2 + q_{RWA3} \left(U_3(\dot{\beta}_3 + \dot{\psi}_3) - \frac{m_{s3}}{m_3} (h_{s3} - h_{r_3}) \ddot{\phi}_3 \right)^2 + q_{RWAi}\mathbf{x}^2 + q_{RWAj}\mathbf{u}^2 \Bigg] dt \tag{6.3.30}$$

where, $\mathbf{x}$ and $\mathbf{u}$ represent state variables and control variables sets represented in equation (3.3.2) and (3.3.3), respectively; and $i = 4, 5, \ldots, 15$ and $j = 16, 17, \ldots, 30$ for the weighting factors q_{RWAi} and q_{RWAj}, respectively. Note that the state variables are added in the cost function in equation (6.3.30) to achieve the improved results for the MTAHVs.

6.3.7.2 *PFOT mode of the Integrated ATS, AR and DB controller*

On the other hand, in the PFOT controller design, the performance index takes the following form

$$J_{PFOT} = \int_0^\infty \Big[q_{PFOT1}\phi_1^2 + q_{PFOT2}\dot{\phi}_1^2 + q_{PFOT3}\beta_1^2 + q_{PFOT4}\dot{\psi}_1^2 + q_{PFOT5}\phi_2^2 + q_{PFOT6}\dot{\phi}_2^2 + q_{PFOT7}\beta_2^2 + q_{PFOT8}\dot{\psi}_2^2 + q_{PFOT9}\phi_{1t}^2 + q_{PFOT10}\phi_{2t}^2 + q_{PFOT11}\delta_{f2}^2 + q_{PFOT12}\delta_{r2}^2 + q_{PFOT13}M_1^2 + q_{PFOT14}M_2^2 + q_{PFOT15}u_{c1}^2 + q_{PFOT16}u_{c2}^2 \Big] dt \tag{6.3.31}$$

subject to equation (6.3.28). Since, at the low speeds, the lateral accelerations at tractor and trailer CG are negligible, in design of the performance index of the PFOT controller, the acceleration terms are ignored. By solving the algebraic Riccati equation, the solution of the optimization problem is the control vector of the form of equation (6.3.6), where $\mathbf{K}_{PFOT}$ is the control matrix with a dimension of 6×10, $\mathbf{x}$ and $\mathbf{u}$ are the state and control variable vectors defined by equations (3.2.4) and (6.3.29), respectively. In equation (6.3.31), q_{PFOTi}, where $i = 1, 2, \ldots, 16$,

are weighting factors that impose penalties upon the each state valuables of state vector **x** defined by equations (3.2.4).

Similarly, following same procedure presented in equation (6.3.31), for MTAHV, the LQR cost function for thePFOT mode of the integrated ATS, AR and DB controller can be generated as follows,

$$J_{PFOT} = \int_0^\infty \left[q_{PFOTi}\mathbf{x}^2 + q_{PFOTj}\mathbf{u}^2 \right] dt \tag{6.3.32}$$

where, **x** and **u** represent state variables and control variables sets represented in equation (3.3.2) and (3.3.3), respectively; and $i = 1, 2, \ldots, 15$ and $j = 16, 17, \ldots, 27$ for the weighting factors q_{PFOTi} and q_{PFOTj}, respectively.

6.4 Summary

In this chapter, different control strategies are designed for the possible active safety systems design for the STAHV. The controller cost functions for the linear quadratic regulator (LQR) control theory for the active trailer steering (ATS), differential braking (DB), anti-roll (AR) systems and their different combination (integrated active safety systems) are derived. Note that in this research only integrated ATS, BD and AR controller will be utilized in designing a STAHV and a MTAHV, discussed in Chapter A and 10, respectively.

CHAPTER 7

Design Method Proposed

7.1 Introduction

This chapter presents a parallel design optimization (PDO) method for multi-trailer articulated heavy vehicles (MTAHVs) with active safety systems (ASSs). It is a challenge to deal with the trade-off between the high-speed stability and the low-speed maneuverability. Evolutionary algorithms have been used for the design optimization of MTAHVs, but the computational efficiency is low. To address the problem, a parallel computing technique with a master-slave system is proposed. Active trailer steering, differential braking and anti-roll sub-systems are combined in an integrated active safety system. Considering the interactions of Driver-Vehicle-ASS, the method simultaneously searches optimal active and passive design variables of the active safety system controllers, the driver model, and the trailers using the master-slave computing system.

The proposed parallel design optimization (PDO) method is described through the design optimization of an active safety system (ASS) for the MTAHV with the tractor/two-semitrailers combination based on the vehicle system model previously introduced. In this chapter, the design criteria for the ASS system, the construction of the LQR controllers, the PDO design method and its implementation are presented.

7.2 Design Variable Set

The design variable set $\mathbf{X}$ is defined as follows.

$$\mathbf{X} = \begin{bmatrix} \mathbf{X}_{SYS} & \mathbf{X}_{CON} & \mathbf{X}_{D} \end{bmatrix} \tag{7.2.1}$$

The design variable set consists of the following three components: the passive vehicle system parameters $\mathbf{X}_{SYS}$, such as the tractor and semitrailer(s) geometric and inertia parameters; the active design variables $\mathbf{X}_{CON}$ for the ASS; and the driver model parameters $\mathbf{X}_{D}$. The active design variable subset $\mathbf{X}_{CON}$ is defined as follows,

$$\mathbf{X}_{CON} = \begin{bmatrix} \mathbf{X}_{RWA} & \mathbf{X}_{PFOT} \end{bmatrix} \tag{7.2.2}$$

where $\mathbf{X}_{RWA}$ and $\mathbf{X}_{PFOT}$ represent the active parameters of the RWA and PFOT controllers. The driver model parameter subset $\mathbf{X}_{D}$ is defined as,

$$\mathbf{X}_{D} = \begin{bmatrix} \mathbf{X}_{DR} & \mathbf{X}_{DP} \end{bmatrix} \tag{7.2.3}$$

where $\mathbf{X}_{DR}$ and $\mathbf{X}_{DP}$ denotes driver model parameters for the high-speed lane change (HSLC) and low-speed path-following (LSPF) simulations, respectively.

7.3 Design Criteria for the ASS System

The objective of designing the active safety system (ASS) is to improve the tractor/semitrailer(s) combination's low-speed maneuverability and high-speed lateral stability. There are various design standards and test procedures imposing performance measure requirements on the low-speed maneuverability and high-speed lateral stability [24, 51]. As introduced previously, the test maneuvers of the 360-degree roundabout (or the 90-degree intersection turn) and the single lane change testing maneuvers are emulated to evaluate the vehicle's low-speed maneuverability and high-speed stability, respectively. Thus, in the design of the ASS system, the following requirements are proposed:

1. to minimize the path-following off-tracking (PFOT) value in the 360-degree roundabout or the 90-degree intersection turn test maneuver;

2. to make the RWA ratio approach the value of 1.0 in the single lane change test maneuver;
3. to minimize the cross differential gap (CDG) value in the single lane change test maneuver;
4. to make the the cross differential gap ratio (CDGR) approach the value of 1.0 in the single lane change test maneuver;
5. to make the lateral acceleration peak value at the tractor's CG approach the value of 0.15 g in the single lane change test maneuver;
6. to minimize the transient off-tracking (TROF) value in the single lane change test maneuver, and
7. to minimize the ASS system power consumption in both high-speed and low-speed test maneuvers.

7.3.1 Criterion-1: minimizing PFOT

In order to improve the low-speed maneuverability, i.e. low-speed circle or corner swept path width, the first design criterion is recommended.

7.3.2 Criterion-2: RWA approaching 1.0

For the purpose of enhancing the high-speed lateral stability, past studies minimized the RWA ratio in the LQR controller design for ASS systems [34, 48, 77, 78]. In a case, the RWA ratio was minimized and took the value of 0.68 [77]. The numerical simulation results reported in Ref. [48] indicate that compared with the baseline vehicle, the optimal design can greatly decrease the RWA ratio and make it take the value of less than 1.0, but the reduction of PFOT (path following off-tracking) value under a low-speed roundabout path following maneuver is limited. In the current research, an ideal value of the RWA ratio is adopted. Following the single lane change test procedure specified in SAE J2179 [68], the objective is

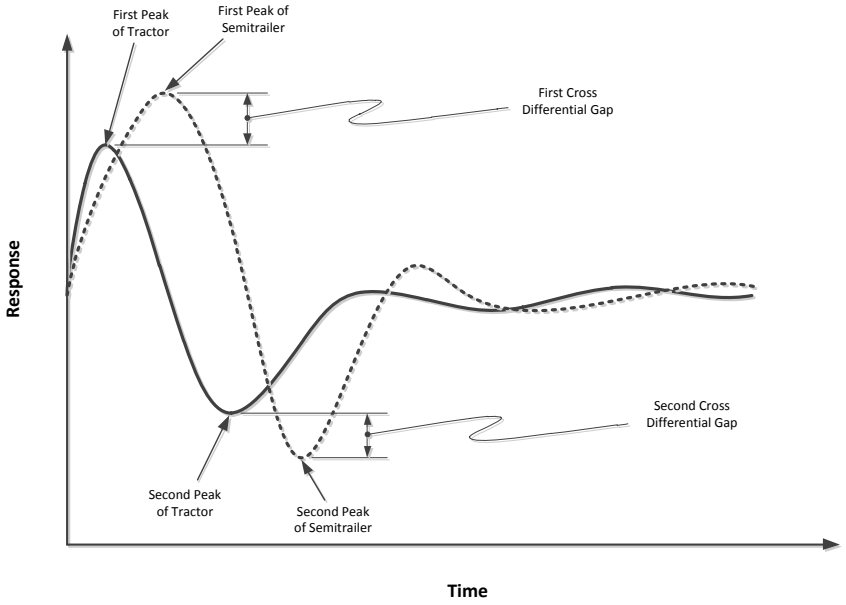

Figure 7.1: Vehicle dynamic response of a tractor and single semitrailer combination versus time in the simulated high-speed single lane change test maneuver

to make the rear end of an AHV follow the front end of the vehicle with adequate fidelity and to prevent the rear unit rollover at a relatively low level of lateral acceleration at the front unit CG. Along this line, it is requested that the lateral acceleration at the trailer's CG should be comparable to that at the tractor's CG. In other words, the ideal RWA ratio takes the value of 1.0. Thus, the second design criterion is proposed.

7.3.3 Criterion-3: minimizing CDG

In this thesis, an important measure is defined, namely, cross differential gap (CDG) of a pair of the dynamic response curves in the single lane-change test maneuver. The CDG is a measure to compare the magnitudes of the corresponding peaks between a pair of curves. Figures 7.1 and 7.2 illustrate the definition of CDG for a tractor and a semitrailer combination and a tractor and two semitrailers combination, respectively. During the maneuver, the time history of a vehicle units' lateral

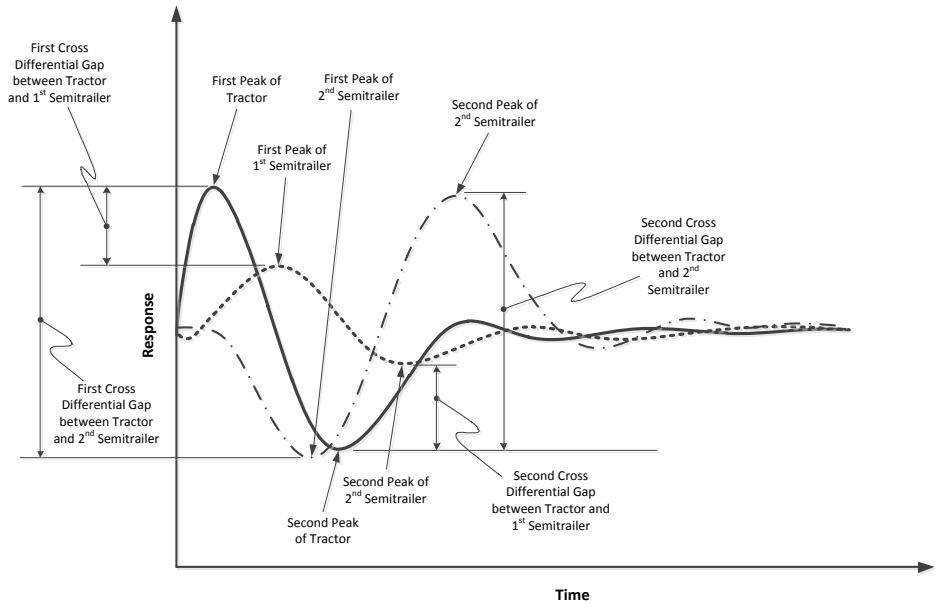

Figure 7.2: Vehicle dynamic response of a tractor and two semitrailers combination versus time in the simulated high-speed single lane change test maneuver

acceleration, yaw rate, etc. of the sprung mass takes a shape of single sine wave consisting of one high and one low peak values. Note that when an active system is integrated in a vehicle system, it is possible to have a reverse order of the high-peak and the low-peak in each of the two curves. An example can be seen in Figure 7.2, when the curves of the tractor and the second semitrailer responses are selected. For a pair of curves, there are two cross differential gaps: the first and the second cross differential gaps. The first cross differential gap, denoted as CDG_1, is the vertical distance between the first (appearing) peak-values of the two selected curves and the second cross differential gap, denoted as CDG_2, is that of the second (appearing) peak-values of the same pair of curves.

7.3.4 Criterion-4: R_{CDG} approaching 1.0

The cross differential gap ratio (R_{CDG}) between two curves are the ratio of the first cross differential gap (CDG_1) to the second cross differential gap (CDG_2) as shown in equation (7.3.1). This value should approach 1.0 so that the optimization process is to improve one CDG ignoring the other.

$$R_{CDG} = \frac{\text{CDG}_1}{\text{CDG}_2} \tag{7.3.1}$$

7.3.5 Criterion-5: lateral acceleration peak value approaching 0.15g

The kinematic description of the high-speed lane-change (HSLC) test maneuver for an AHV is offered in SAE J2179 [68] as follows: "The lateral displacement of the course in the maneuvering section represents the motion of a point that is traveling at 88.0 km/h for 2.5 s with a lateral acceleration of the form $-A\sin(2\pi t/2.5)$, where t is time in seconds ($t = 0$ at the beginning of the maneuvering section) and $A = 0.15g$ (g denoting the acceleration of gravity)".

To achieve the similar form of the curves of the lateral acceleration at the tractor and trailers' CG in the single lane-change maneuver, the fifth criterion is imposed on the design method. This criterion implies that the high- and low-peak of each

curve of the lateral acceleration at tractor and semitrailers' CG approach the value of 0.15 g.

Due to AHVs' large sizes, heavy loads and high centre of gravities, these vehicles have much lower rollover threshold values than those of passenger cars [91]. The AHVs' rollover stability is directly dependent on the tractor or trailer lateral acceleration. In obstacle avoidance situations on highways, the AHV should respond to the driver's steering input quickly and adequately and no unit of the vehicle should rollover. While AVHs' speeds are low in local road and street operations, these vehicles are still more susceptible than passenger cars to rollover during tight curve negations. To ensure safe and stable operations in both obstacle avoidance situations on highways and tight curve negations on local roads and streets, the lateral acceleration at the CG of both the tractor and trailer should be lower than the corresponding threshold values. Therefore, the fifth design criterion is drawn up.

7.3.6 Criterion-6: minimizing TROF

The transient off-tracking (TROF) is defined as the maximum radial offset between the trajectories of front axle center of tractor and that of rear axle of (usually, the rearmost) semitrailer in the high-speed lane change (HSLC) maneuver. In the proposed design method, this criterion is used to minimize the value of TROF, thereby, to improve path following performance at high-speeds.

7.3.7 Criterion-7: minimizing power consumption

With the consideration of the active safety system's power consumption, the seventh criterion is imposed on the proposed design methodology.

As will be discussed in the following sections, the above design criteria will be implemented in the design of AHVs with active safety systems.

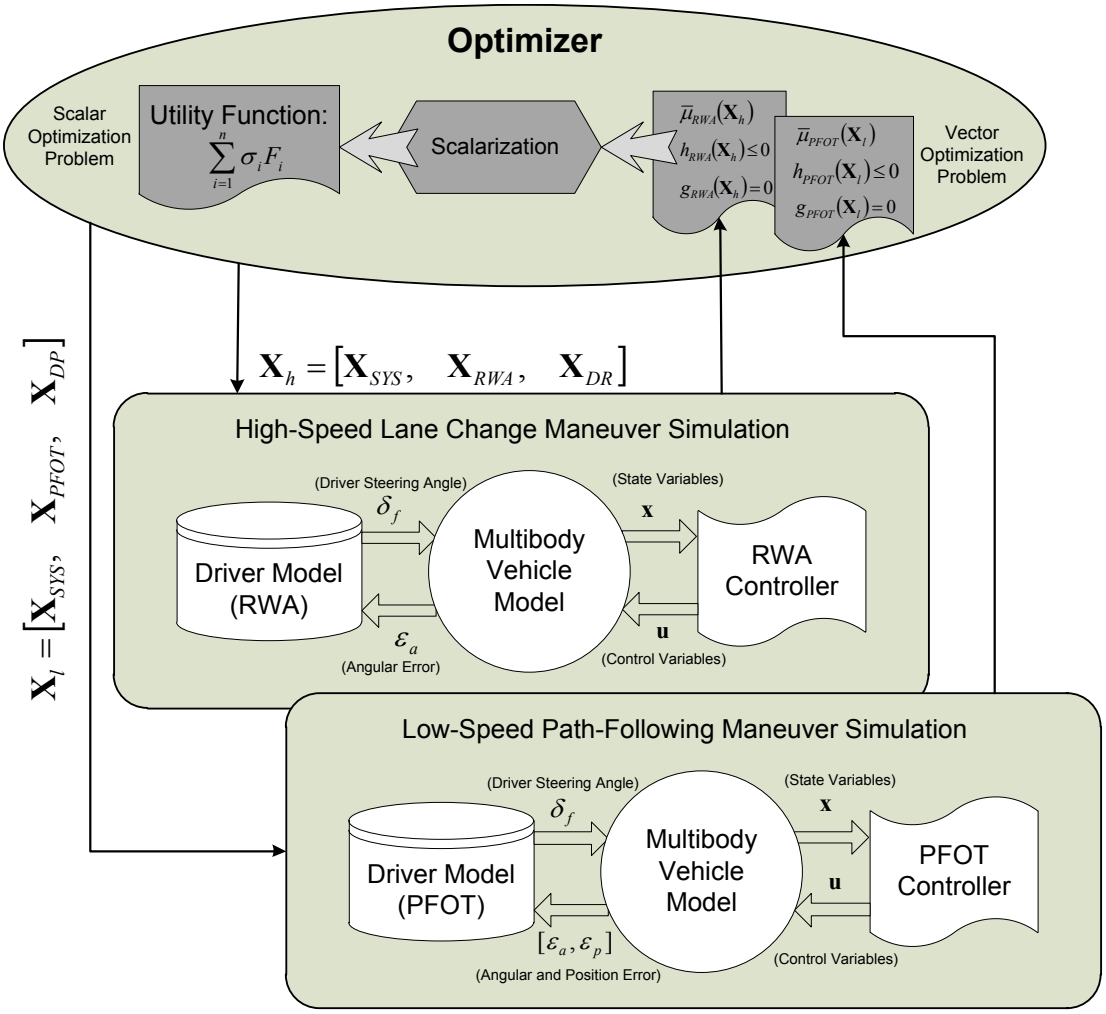

Figure 7.3: Schematic representation of the PDO design method

7.4 Proposed PDO Design Method

The framework of the proposed parallel design optimization (PDO) design method is shown in Figure 7.3. The single design loop (SDL) method offers a multi-objective formulation approach to a bilevel optimization problem of active safety systems for MTAHVs: at the subsystem level, the seventh design criterion discussed in section 7.3 is formulated; at the system level, from the first to the sixth design criteria are concocted.

As shown in Figure 7.3, in each iteration of the design optimization, the high-speed

lane change (HSLC) procedure and the low-speed path-following (LSPF) maneuver (360-degree roundabout or 90-degree intersection turn) can be simulated concurrently. For instance, in an iteration, a design variable set $\mathbf{X}_h$ is sent to the HSLC simulation module.

Design variable set $\mathbf{X}_h$ consists of $\mathbf{X}_{SYS}$, $\mathbf{X}_{RWA}$, and $\mathbf{X}_{DR}$. Note that $\mathbf{X}_{SYS}$ represents passive vehicle system parameters, such as the tractor and trailer geometric and inertia parameters; $\mathbf{X}_{RWA}$ denotes RWA controller parameters; and $\mathbf{X}_{DR}$ denotes the driver model parameters for HSLC maneuver, e.g., K_{ph} and t_{pv} as shown in equations (5.4.1) and (5.4.2), respectively. As discussed in Chapter 6, the RWA controller is designed to enhance the high-speed lateral stability of AHVs. The linear quadratic regulator (LQR) technique is applied to the design of the RWA controller. The design of the RWA controller alone is a subproblem of the AHV design optimization problem. As addressed in Chapter 6, at the subsystem level the seventh design criterion defined in section 7.3 will be formulated in the construction of the RWA controller. Given the design variable set $\mathbf{X}_h$, including $\mathbf{X}_{DR}$, $\mathbf{X}_{SYS}$ and $\mathbf{X}_{RWA}$ for the driver model, vehicle model and RWA controller, respectively, these three models are integrated and the HSLC test maneuver can be simulated.

With the feedback angular error (ε_a) between the direction of the path and the actual vehicle alignment, the driver *drives* the vehicle model by means of manipulating the steering angle (δ_{1f}). Given the current vehicle state variables $\mathbf{x}$ that can be achieved through a sensor system, the RWA controller determines the control variables $\mathbf{u}$ in order to get the desired active steering angles (δ_{2f}, δ_{2m}, δ_{2r}, δ_{3f}, δ_{3m}, and δ_{3r}), active yaw moments (M_1, M_2, and M_3), and anti-roll torques (u_{c1}, u_{c2}, and u_{c3}) for the MTAHV. In this process, the driver model *drives* the virtual vehicle following the test procedure specified in SAE J2179 [68]. After the numerical simulation of the HSLC test maneuver, the performance measures corresponding to the second to the sixth design criteria discussed in section 7.3 can be achieved.

Similarly, in the iteration, a design variable set $\mathbf{X}_l$ is sent to the LSPF simulation module. Design variable set $\mathbf{X}_l$ consists of $\mathbf{X}_{SYS}$, $\mathbf{X}_{PFOT}$, and $\mathbf{X}_{DP}$. Note that $\mathbf{X}_{DP}$

denotes driver model parameters for the LSPF maneuver, i.e., K_{pl}, K_{il} and K_{dl} shown in equation (5.3.6), and $\mathbf{X}_{PFOT}$ stands for the PFOT controller parameters. As addressed in Chapter 6, the PFOT controller is designed to improve the low-speed maneuverability of AHVs. The LQR technique is also applied to the design of the PFOT controller. Like the design of the RWA controller, at the subsystem level the seventh design criterion defined in section 7.3 will be formulated in the construction of the PFOT controller. Given the design variable set $\mathbf{X}_l$, including $\mathbf{X}_{DP}$, $\mathbf{X}_{SYS}$, and $\mathbf{X}_{PFOT}$ for the driver model, vehicle model and PFOT controller, respectively, these three models are integrated and the LSPF test maneuver can be simulated. During the process, the driver model *drives* the virtual vehicle based on the low-speed path-following maneuver (360-degree roundabout or 90-degree intersection turn). After the simulation of the LSPF test maneuver, the performance measure can be obtained, which corresponds to the first design criterion.

As shown in Figure 7.3, with the completion of this iteration's HSLC and LSPF simulations, at the system level one is faced with a vector optimization problem with the two design criteria, $\overline{\mu}_{RWA}(\mathbf{X}_h)$ and $\overline{\mu}_{PFOT}(\mathbf{X}_l)$, and corresponding constraints, $\mathbf{h}_{RWA}(\mathbf{X}_h) \leq 0$ and $\mathbf{g}_{RWA}(\mathbf{X}_h) = 0$, and $\mathbf{h}_{PFOT}(\mathbf{X}_l) \leq 0$ and $\mathbf{g}_{PFOT}(\mathbf{X}_l) = 0$. Using the technique of scalarization reported in Ref. [35], the vector optimization problem is reduced to a scalar optimization problem that can be formulated in the following format:

$$\begin{aligned} \textit{minimize} \quad & \sum_{i=1}^{n} \sigma_i F_i \\ \textit{with respect to} \quad & \mathbf{X}_h = \begin{bmatrix} \mathbf{X}_{SYS} & \mathbf{X}_{RWA} & \mathbf{X}_{DR} \end{bmatrix}, \\ & \mathbf{X}_l = \begin{bmatrix} \mathbf{X}_{SYS} & \mathbf{X}_{PFOT} & \mathbf{X}_{DP} \end{bmatrix} \end{aligned} \tag{7.4.1}$$

where σ_1 to σ_n are weighting factors. For the STAHV, n takes the value of 7 and, in the formulation in equation (7.4.1), and F_1 to F_7 are defined as

$$F_1 = \frac{CDG_{1\_12}(\mathbf{X}_h)}{CDG_{1\_12nom}} \tag{7.4.2a}$$

$$F_2 = \frac{CDG_{2\_12}(\mathbf{X}_h)}{CDG_{2\_12nom}} \tag{7.4.2b}$$

$$F_3 = \frac{\mid R_{CDG12}(\mathbf{X}_h) - 1.0 \mid}{\mid R_{CDG12nom} - 1.0 \mid} \tag{7.4.2c}$$

$$F_4 = \frac{TROF_{15}(\mathbf{X}_h)}{TROF_{15nom}} \tag{7.4.2d}$$

$$F_5 = \frac{\mid a_{peak1}(\mathbf{X}_h) - 0.15 \mid}{\mid a_{peak1\_nom} - 0.15 \mid} \tag{7.4.2e}$$

$$F_6 = \frac{\mid a_{peak2}(\mathbf{X}_h) - 0.15 \mid}{\mid a_{peak2\_nom} - 0.15 \mid} \tag{7.4.2f}$$

$$F_7 = \frac{PFOT_{15}(\mathbf{X}_l)}{PFOT_{15nom}} \tag{7.4.2g}$$

where the subscript *nom* implies the baseline vehicle of the STAHV. In equations (7.4.2a) and (7.4.2b), CDG_{i_jk}, where $j \neq k$, denotes the i-th (first or second) cross differential gap of the lateral acceleration CDG_i, where $i = 1, 2$, at vehicle unit-j CG and vehicle unit-k CG. Note that for an STAHV, the vehicle unit-1 denotes the tractor and vehicle unit-2 the represents semitrailer. In equations (7.4.2a) and (7.4.2b), CDG_{1_12} and CDG_{1_12} denote the first and second cross differential gap of the lateral acceleration curves of the tractor and the semitrailer, respectively, and CDG_{1_12nom} and CDG_{2_12nom} represent the corresponding nominal values. In equation (7.4.2c), R_{CDG12} denotes the cross differential gap ratio for the curves of the lateral acceleration at the tractor and the semitrailer CG and $R_{CDG12nom}$ denotes the corresponding ratio for the baseline case. In equation (7.4.2d), $TROF_{15}(\mathbf{X}_h)$ denotes the transient off-tracking between the trajectory of the centers of axle-1 and axle-5 in the high-speed lane change maneuver and $TROF_{15nom}$ denotes corresponding transient off-tracking of the baseline case. In equations (7.4.2e) and (7.4.2f), $a_{peak1}(\mathbf{X}_h)$ and $a_{peak2}(\mathbf{X}_h)$ represent the peak value of the first peak (the maximum value) and the second peak (the minimum value) of the curve of the lateral acceleration at the tractor CG, respectively. Similarly, a_{peak1_nom} and a_{peak2_nom} represent the corresponding peak values of the lateral acceleration curve for the

baseline case. In equation (7.4.2g), the path-following off-tracking (PFOT) value calculated from the trajectory of axle-1 and axle-5 is denoted as $PFOT_{15}(\mathbf{X}_l)$ and the corresponding baseline values are presented as $PFOT_{15nom}$.

In equation (7.4.2), F_1 and F_2 represent the third design criterion and F_3 denotes the fourth criterion defined in section 7.3. Note that F_1, F_2, and F_3 combinedly represent the second design criterion. In other words, satisfying the third and fourth design criteria automatically satisfy the second criteria. In equation (7.4.2d), F_4 represents the sixth design criterion described in section 7.3. The fifth design criteria is represented by F_5 and F_6. The sixth criterion is presented by F_7. Global search stochastic algorithms, e.g., simulated annealing algorithms and genetic algorithms (GAs), can be used to solve the scalar optimization problem [35]. In the current research, a GA is used as the optimizer to resolve the trade-off relation between the high-speed lateral stability and the low-speed maneuverability at the system level.

On the other hand, in equation (7.4.1), for a multi-trailer articulated heavy vehicle (MTAHV), n takes the value of 27. Using the similar notations described above, in the formulation in equation (7.4.1), the lateral acceleration terms from F_1 to F_6 for the MTAHV are defined as

$$F_1 = \frac{CDG_{acc1\_13}(\mathbf{X}_h)}{CDG_{acc1\_13nom}} \tag{7.4.3a}$$

$$F_2 = \frac{CDG_{acc2\_13}(\mathbf{X}_h)}{CDG_{acc2\_13nom}} \tag{7.4.3b}$$

$$F_3 = \frac{\mid R_{CDGacc13}(\mathbf{X}_h) - 1.0 \mid}{\mid R_{CDGacc13nom} - 1.0 \mid} \tag{7.4.3c}$$

$$F_4 = \frac{CDG_{acc1\_12}(\mathbf{X}_h)}{CDG_{acc1\_12nom}} \tag{7.4.3d}$$

$$F_5 = \frac{CDG_{acc2\_12}(\mathbf{X}_h)}{CDG_{acc2\_12nom}} \tag{7.4.3e}$$

$$F_6 = \frac{\mid R_{CDGacc12}(\mathbf{X}_h) - 1.0 \mid}{\mid R_{CDGacc12nom} - 1.0 \mid} \tag{7.4.3f}$$

The terms related to the cross-differential gap and ratio of the way rates from F_7 to F_{12} are generated as follows,

$$F_7 = \frac{CDG_{yaw1\_13}(\mathbf{X}_h)}{CDG_{yaw1\_13nom}} \tag{7.4.4a}$$

$$F_8 = \frac{CDG_{yaw2\_13}(\mathbf{X}_h)}{CDG_{yaw2\_13nom}} \tag{7.4.4b}$$

$$F_9 = \frac{\mid R_{CDGyaw13}(\mathbf{X}_h) - 1.0 \mid}{\mid R_{CDGyaw13nom} - 1.0 \mid} \tag{7.4.4c}$$

$$F_{10} = \frac{CDG_{yaw1\_12}(\mathbf{X}_h)}{CDG_{yaw1\_12nom}} \tag{7.4.4d}$$

$$F_{11} = \frac{CDG_{yaw2\_12}(\mathbf{X}_h)}{CDG_{yaw2\_12nom}} \tag{7.4.4e}$$

$$F_{12} = \frac{\mid R_{CDGyaw12}(\mathbf{X}_h) - 1.0 \mid}{\mid R_{CDGyaw12nom} - 1.0 \mid} \tag{7.4.4f}$$

The terms related to the cross-differential gap and ratio of the roll angles from F_{13} to F_{18} are generated as follows,

$$F_{13} = \frac{CDG_{roll1\_13}(\mathbf{X}_h)}{CDG_{roll1\_13nom}} \tag{7.4.5a}$$

$$F_{14} = \frac{CDG_{roll2\_13}(\mathbf{X}_h)}{CDG_{roll2\_13nom}} \tag{7.4.5b}$$

$$F_{15} = \frac{\mid R_{CDGroll13}(\mathbf{X}_h) - 1.0 \mid}{\mid R_{CDGroll13nom} - 1.0 \mid} \tag{7.4.5c}$$

$$F_{16} = \frac{CDG_{roll1\_12}(\mathbf{X}_h)}{CDG_{roll1\_12nom}} \tag{7.4.5d}$$

$$F_{17} = \frac{CDG_{roll2\_12}(\mathbf{X}_h)}{CDG_{roll2\_12nom}} \tag{7.4.5e}$$

$$F_{18} = \frac{\mid R_{CDGroll12}(\mathbf{X}_h) - 1.0 \mid}{\mid R_{CDGroll12nom} - 1.0 \mid} \tag{7.4.5f}$$

The terms related to the cross-differential gap and ratio of the articulation angles from F_{19} to F_{21} are generated as follows,

$$F_{19} = \frac{CDG_{art1\_13}(\mathbf{X}_h)}{CDG_{art1\_13nom}} \tag{7.4.6a}$$

$$F_{20} = \frac{CDG_{art2\_13}(\mathbf{X}_h)}{CDG_{art2\_13nom}} \tag{7.4.6b}$$

$$F_{21} = \frac{\mid R_{CDGart13}(\mathbf{X}_h) - 1.0 \mid}{\mid R_{CDGart13nom} - 1.0 \mid} \tag{7.4.6c}$$

Similarly, the terms F_{22} and F_{23} related to the lateral acceleration peak value of tractor CG, the terms F_{24} and F_{25} related to the transient path-following off-tracking in the high-speed lane-change maneuver, and the terms F_{26} and F_{27} related to the path-following off-tracking in the low-speed 90-degree intersection tern maneuver are generated as follows,

$$F_{22} = \frac{\mid a_{peak1}(\mathbf{X}_h) - 0.15 \mid}{\mid a_{peak1\_nom} - 0.15 \mid} \tag{7.4.7a}$$

$$F_{23} = \frac{\mid a_{peak2}(\mathbf{X}_h) - 0.15 \mid}{\mid a_{peak2\_nom} - 0.15 \mid} \tag{7.4.7b}$$

$$F_{24} = \frac{TROF_{19}(\mathbf{X}_h)}{TROF_{19nom}} \tag{7.4.7c}$$

$$F_{25} = \frac{TROF_{16}(\mathbf{X}_h)}{TROF_{16nom}} \tag{7.4.7d}$$

$$F_{26} = \frac{PFOT_{19}(\mathbf{X}_l)}{PFOT_{19nom}} \tag{7.4.7e}$$

$$F_{27} = \frac{PFOT_{16}(\mathbf{X}_l)}{PFOT_{16nom}} \tag{7.4.7f}$$

7.5 Implementation of the Design Optimization Method

Figure 7.4 shows the computer implementation of the SDL design method. In both of the high-speed lane change (HSLC) and the low-speed path-following (LSPF) maneuver simulation modules, the vehicle models are the same and they can be generated using multibody dynamic programs, e.g. ADAMS and TruckSim. It is observed that once a sophisticated nonlinear multibody articulated heavy vehicle model from TruckSim is integrated with the GA, the computational burden is

too high for a regular desktop computer [66]. Considering the computational efficiency, in the case study presented in this thesis no multibody dynamic software is integrated and the 5 DOF or the 7 DOF vehicle model is employed. In the case of the HSLC module, the RWA controller and driver model are constructed in Matlab. Then, the vehicle model, RWA controller and driver model are combined and prepared for numerical simulation. Note that in both of the HSLC and LSPF simulation modules, the corresponding driver models share the same structure, but parameters of the two driver models are different due to their velocity dependent features.

As shown in Figure 7.4, a population of n sets of design variables is evaluated by the GA [28]. For a given design variable set $\mathbf{X}$, it consists of $\mathbf{X}_{SYS}$, $\mathbf{X}_{CON}$ and $\mathbf{X}_D$ as shown in equation (7.2.1). The control variable set $\mathbf{X}_{CON}$ and the driver model parameter set $\mathbf{X}_D$ are defined in equation (7.2.2) and (7.2.3), respectively. The design variables can be recombined as $\mathbf{X}_h$ for HSLC simulation and $\mathbf{X}_l$ for LSPF simulation. The recombined design variables are defined as follows

$$\mathbf{X}_h = \begin{bmatrix} \mathbf{X}_{SYS} & \mathbf{X}_{RWA} & \mathbf{X}_{DR} \end{bmatrix} \tag{7.5.1}$$

and

$$\mathbf{X}_l = \begin{bmatrix} \mathbf{X}_{SYS} & \mathbf{X}_{PFOT} & \mathbf{X}_{DP} \end{bmatrix}. \tag{7.5.2}$$

With the variable vectors $\mathbf{X}_h$ and $\mathbf{X}_l$ sent to the HSLC and LSPF modules, respectively, the corresponding numerical simulation can be performed.

The introduction of active stability control has stimulated closed-loop stability analysis in which the driver is represented by a driver model [74]. The driver model is frequently treated as a controller, and the effects of the controller parameters, such as feedback control gains, on directional performance of AHVs have been investigated [59, 74]. To consider the impact of the driver on the directional performance of the AHV, the driver model parameters are treated as design variables in the proposed design method.

With the completion of the HSLC and LSPF simulation, the corresponding vehicle

dynamic responses can be achieved. The data processors determine the resulting performance measures. The performance measure obtained from HSLC simulation includes the first cross differential gap of the lateral acceleration CDG_1, the second cross differential gap CDG_2, the cross differential gap ratio of the lateral acceleration R_{CDG}, the first peak (the maximum value in Figure 7.1 and 7.2) lateral acceleration at the tractor CG a_{peak1}, the second peak (the minimum value in Figure 7.1 and 7.2) lateral acceleration at the tractor CG a_{peak2}, and transient off-tracking $TRPF$. From the LSPF simulation, the performance measure obtained is the path-following off-tracking $PFOT$ value.

The performance measures are used to formulate the following utility function that will be minimized at the system level by the GA.

$$obj(\mathbf{X}) = \sum_{i=1}^{n} \sigma_i F_i \tag{7.5.3}$$

As mentioned before, $\mathbf{X}$ denotes the design variable set, σ_i for $i = 1, 2, \ldots, n$, denotes the weighting factors, and n takes the value of 7 for the STAHV and 12 for the MTAHV. In equation (7.5.3), F_i can be obtained from equations (7.4.2) or (**??**) for the STAHV or MTAVH, respectively. Using the utility function, the GA may effectively coordinate the design criteria of the high-speed stability and the low-speed maneuverability.

As shown in Figure 7.4, corresponding to the n sets of design variables, $\mathbf{X}_i, i = 1, 2, \ldots, n$, the resulting fitness value vector $\begin{bmatrix} obj_1 & obj_2 & \ldots & obj_n \end{bmatrix}^T$ can be achieved by evaluating the utility function expressed in equation (7.5.3). At this point, if the convergence criteria are satisfied, the calculation terminates; otherwise, this vector is sent back to the GA. Based on the returned fitness values corresponding to the given sets of design variables, the GA produces the next generation of design variable sets using selection, crossover, and mutation operators. This procedure repeats until the optimized variable set is found.

With the above implementation of the design optimization problem, all the design variables, including passive vehicle design variables $\mathbf{X}_{SYS}$, and the weighting

factors $\mathbf{X}_{RWA}$ and $\mathbf{X}_{PFOT}$ for the RWA and PFOT controllers, and the driver model parameters $\mathbf{X}_{DR}$ and $\mathbf{X}_{DP}$ for the HSLC and LSPF simulations, respectively, can be optimized in a single design loop.

7.6 Summary

The proposed parallel design optimization (PDO) method for the STAHV and the MTAHV with active safety systems is described in details in this chapter. The parallel computing systems and its implementation technique of the proposed design method will be discussed in the next chapter.

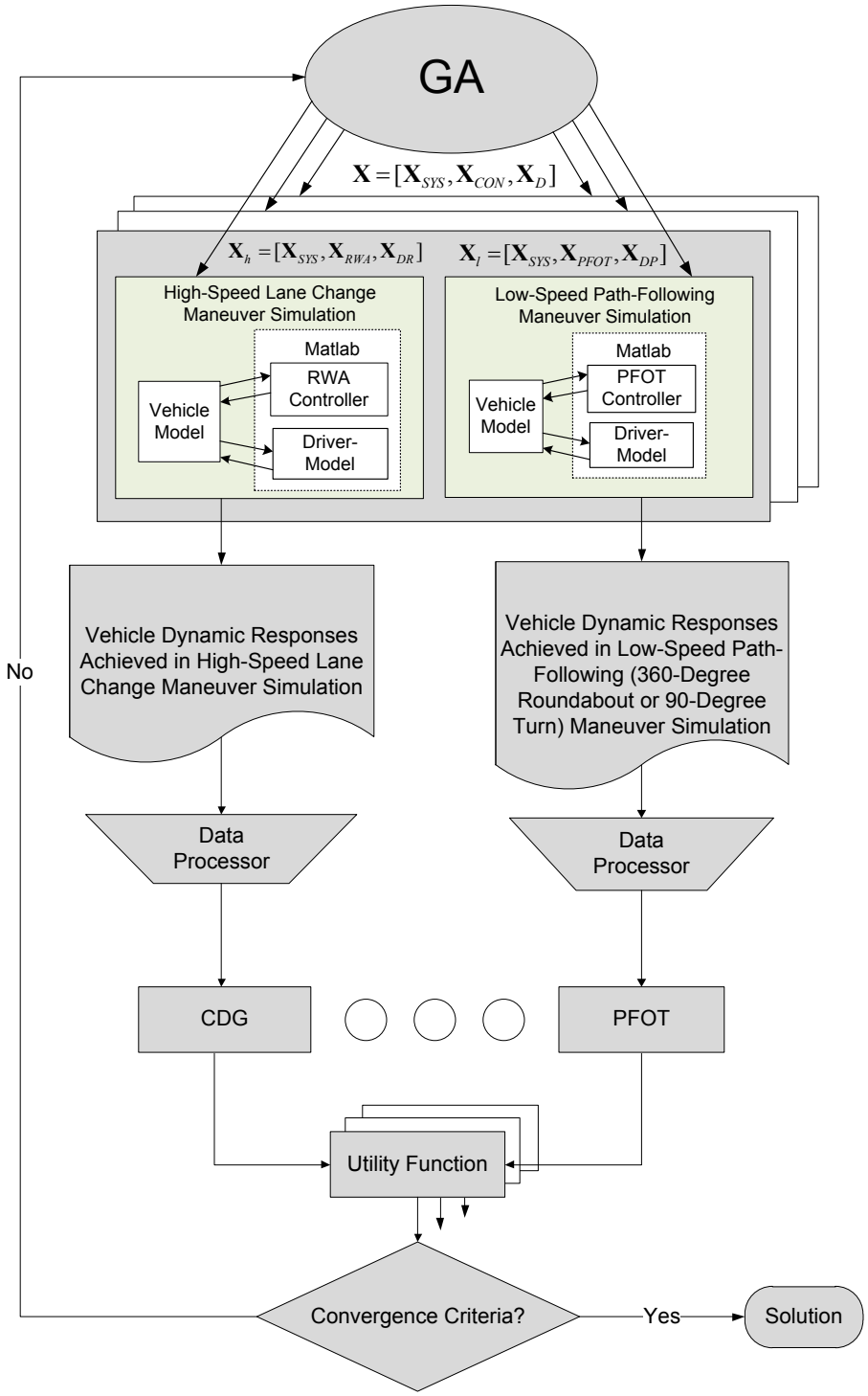

Figure 7.4: Schematic representation of the preliminary framework of proposed integrated design method

CHAPTER 8

Parallel Computation System

8.1 Introduction

To implement the parallel numerical optimization of MTAHVs with the ASS with respect to both the high-speed stability and the low-speed maneuverability, the GA is executed on a master/salve computer system that consists of one master node and twenty slave nodes. Each slave node contains one central processing unit (CPU), whereas the master node contains two CPUs. In both the master and slave nodes, each CPU consists of four cores. All available cores form a pool from which a core is assigned to a demanding computing job. At any instant of time, one process is executed by only one core based on the availability. However, it is possible that a task/process is completed by multiple cores, one by one consecutively. Among the Matlab workers, each one takes one core from the pool of CPU cores at any instant of time. All the task executions are done dynamically among the cores.

8.2 Parallel Computation System

Figure 8.2 shows the cluster architecture in Matlab environment. The user is directly connected to the parallel computation toolbox (PCT). The Matlab scheduler receives user instruction or task from PCT. This Matlab scheduler stays on the mas-

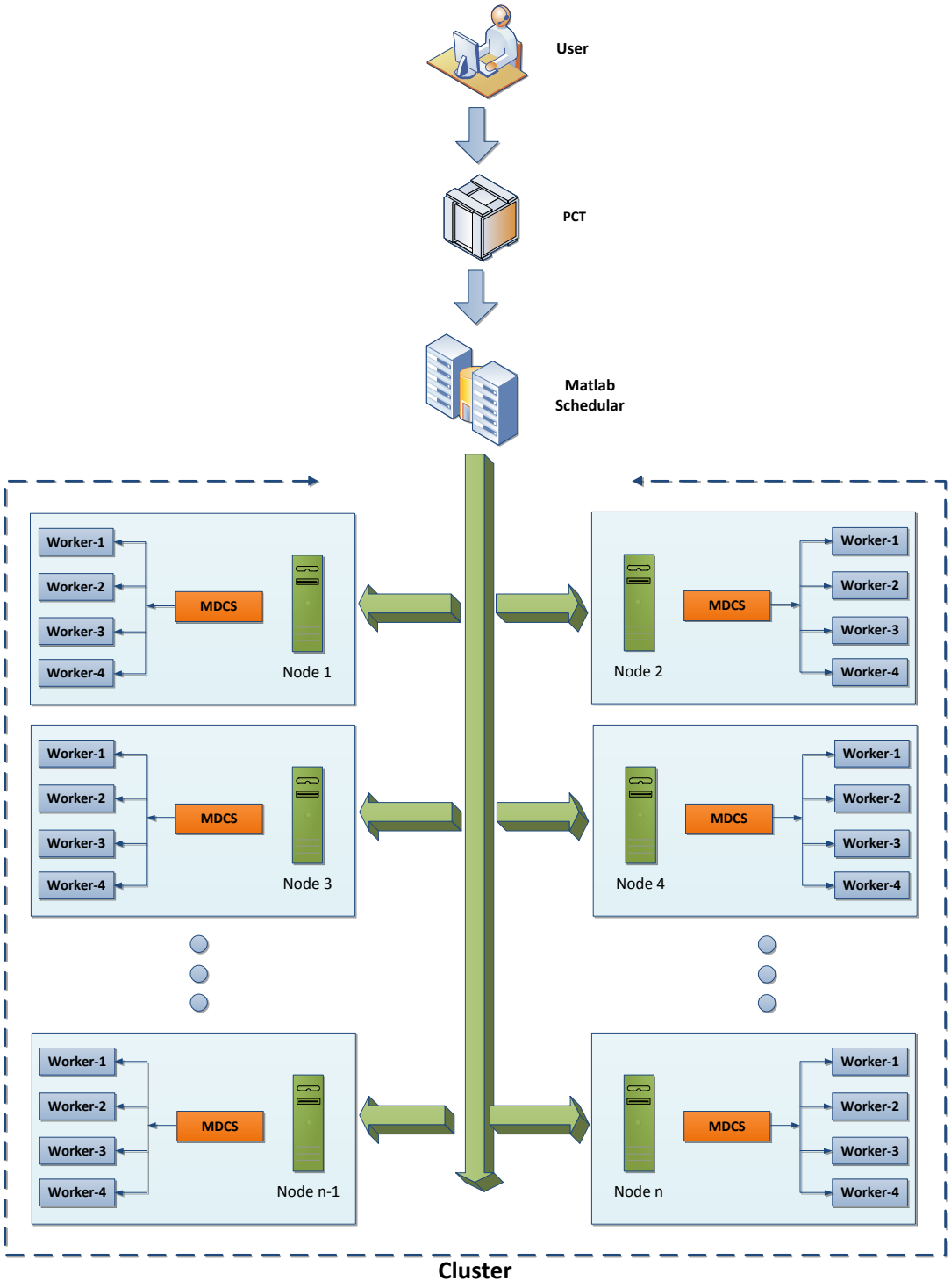

Figure 8.1: Cluster architecture in Matlab environment

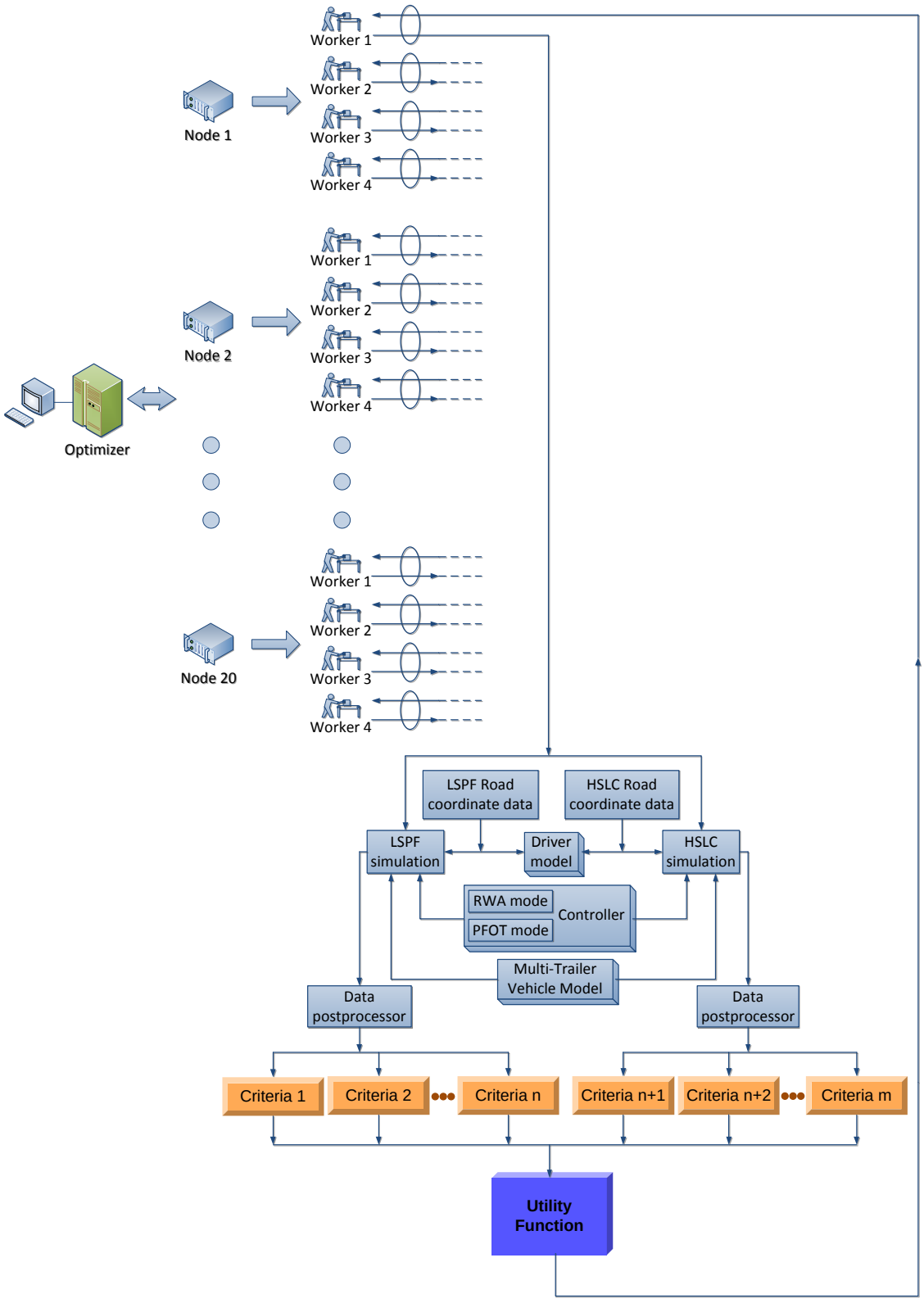

Figure 8.2: Design framework using the master-slave system in the design synthesis of MTAHVs with ASS

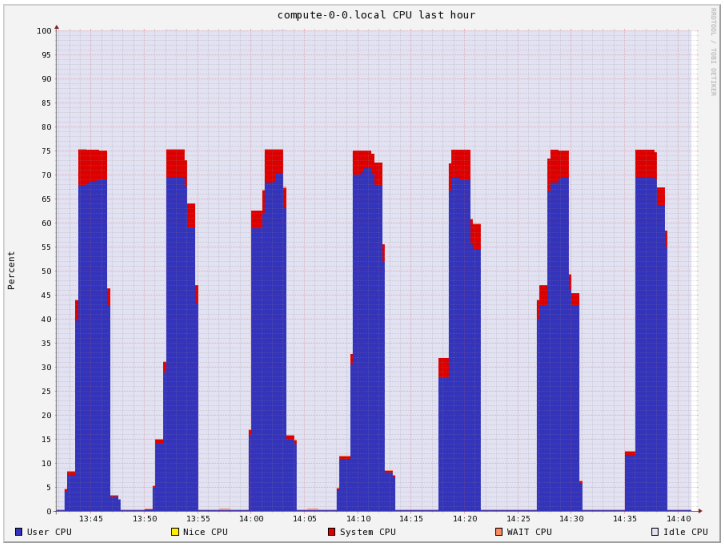

Figure 8.3: Utilization of the central processing unit capability of a node with single matlab session running

ter node and manages the entire parallel computation job. The scheduler assigns tasks to the Matlab distributed computation server (MDCS) agent. Each MDCS agent is connected to a worker. The agent sends computation task to a Matlab worker. When the computation task is done, the agent collects and sends the result back to PCT via scheduler. Then, the agent waits for the next instruction from the scheduler. Underneath Matlab MDCS (Matlab Distributed Computing Server) is a Beowulf cluster using MPI (Message Passing Interface) for interconnecting communication among cluster nodes.

8.3 Parallel Computational Efficiency

8.3.1 Communication Rate

The parallel computing task of the design problem using the proposed method is implemented in a cluster shown in Figure 8.5, called 'Hediy', located at the University of Ontario Institute of Technology (UOIT), Canada. Figure 8.3 illustrates the time history of the utilization of the central processing unit's capability of a node with single Matlab sessions of parallel design optimization tasks running.

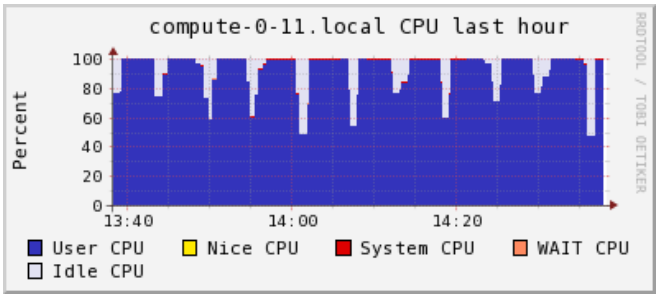

Figure 8.4: Utilization of the central processing unit's capability of a node with multiple matlab sessions running simultaneously

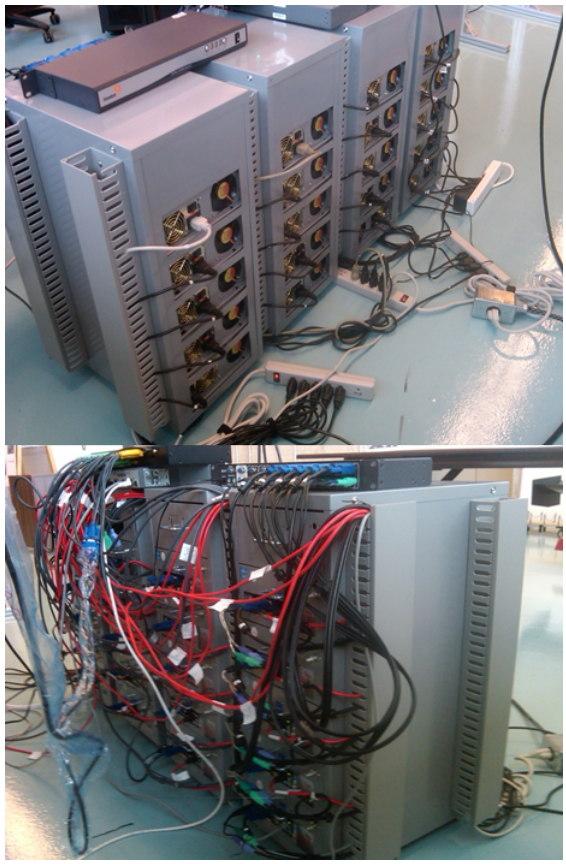

Figure 8.5: Parallel computing cluster system, 'Hediy'

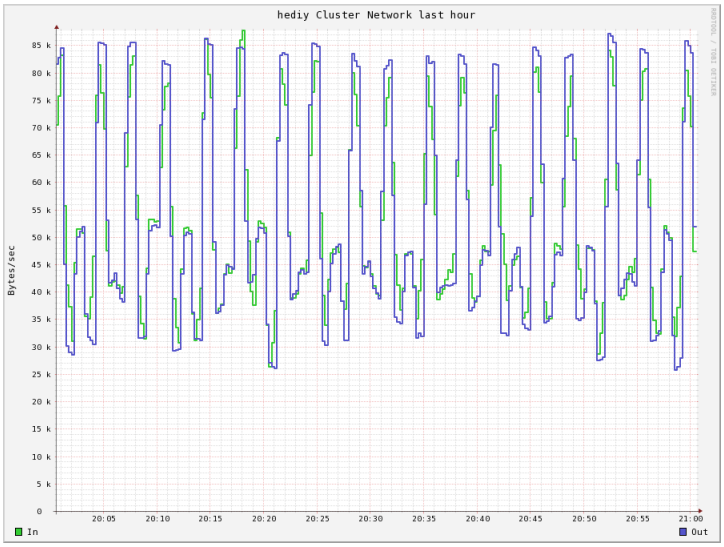

Figure 8.6: Network communication in the cluster for one hour

Figure 8.4 illustrates the improved utilization of the central processing unit's capability of a node with multiple Matlab sessions of parallel design optimization tasks running simultaneously. Figure 8.6 shows the time history of communication rate (Byte/sec) in the parallel computing cluster during a typical run of the design optimization of a tractor and two trailer combination using the proposed design method. A close observation of the figure reveals that the amount of communication rate among different nodes and workers is significantly low. This is a clear indication that the program and thereby the design method is scalable. Each node/worker performs its own assigned job more independently avoiding time-consuming communication through data transfer which may cause high-traffic situation. Therefore, the design job is more suitable for the parallel computation.

8.3.2 Effect of Number of Workers

The proposed design method is implemented for designing a tractor and two semi-trailers combination using the parallel computing cluster with a different number of workers. Figure 8.7 illustrates the computation time versus the number of workers selected for the given design problem. The total number of design variables is 63 in this design optimization problem of the MTAHV. For each run, the popula-

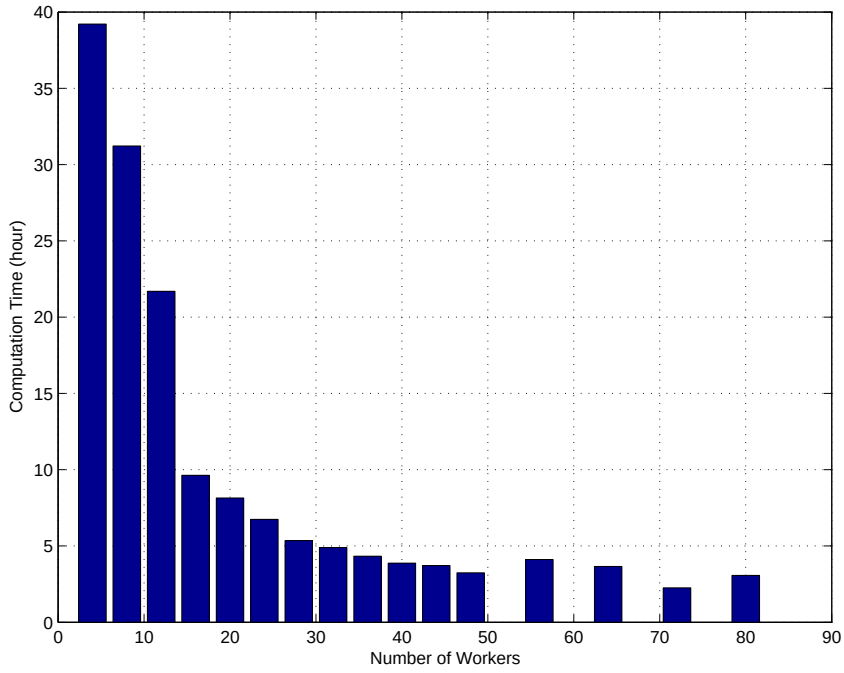

Figure 8.7: Computation time versus the number of workers during the design optimization of MTAHVs with ATS systems

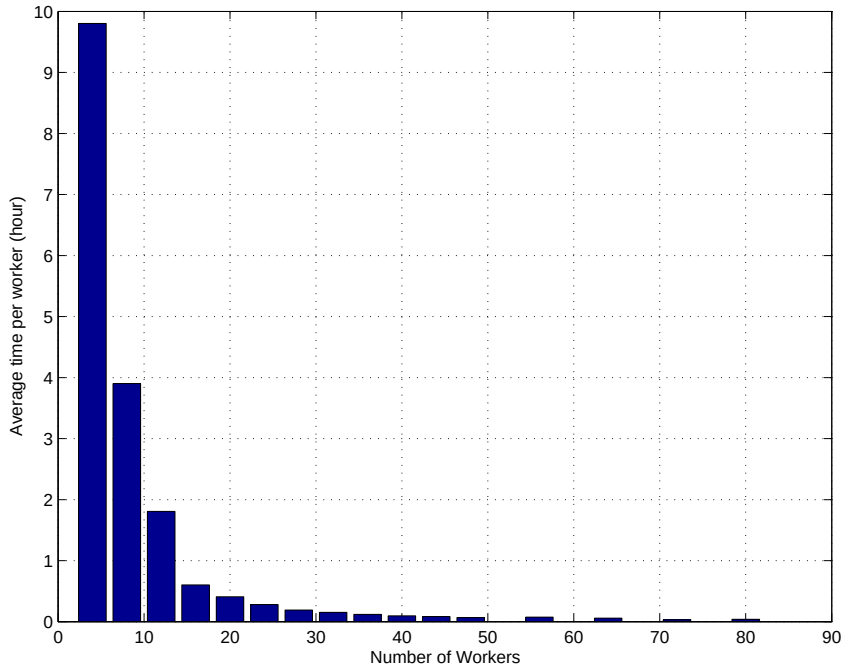

Figure 8.8: Ratio of computation time to the number of workers versus the number of workers during the design optimization of MTAHVs with ATS systems

tion size of the genetic algorithm (GA) is 640 and the maximum number of generation is 100. In this case, the tolerance function of the GA takes the value of 10^{-4}, which is a higher value compared to a typical design optimization. The solution of the design problem is not the main focus here, but the computational efficiency is more important. Therefore, the higher value of the tolerance function is chosen to finish the optimization relatively faster. With this tolerance function value, the optimization converges around 51th generation. The other conditions are kept the same for each run of the optimization problem. A close observation of the figure reveals that, with the increase of the number of workers, the computation time decreases. However, the rate of reduction of computation time is also decreased with an increasing number of workers. In other words, with a very high number of workers, a further increase in the number of workers does not have a significant effect on the computation time of the design problem.

This can be further illustrated in Figure 8.8. This figure shows the ratio of the total computation time to the number of workers versus the number of cores. It is clear from the figure that after the number of cores reaches 32, any additional worker in the pool is unable to significantly improve the ratio of total computation time to the number of workers. From Figure 8.7, in the range of the number of workers from 40 to 80, there is a little fluctuation in the total computation time. There are a couple of possible reasons that may cause this variation from the decremental pattern. When the temperature of the motherboard is very high, the CPU clock frequency is decreased to control the temperature and the computation time is increased. With a large number of workers, the communication among workers increases due to latency from the Ethernet interconnect. A possible solution to this latency could be the use of InfiniBand [7].

Another possible reason could be the lack of better partition of the computation problem [36, 65] so that some workers are sitting idle while the other workers are busy. If this is the case, although the number of workers is increased, the computation efficiency may not be increased accordingly. To avoid this type of problem, the population size of the GA should be multiple times that of the available number

of workers in the computation pool.

8.4 Summary

The framework of the proposed design optimization method using the parallel computation technique with the master-slave system is shown in this chapter. The proposed method offers a multi-objective formulation approach to the design optimization of integrated active systems for MTAHVs to be implemented using a parallel genetic algorithm (GA) in Matlab. This chapter investigated the high-performance computing platform and its performance has been analyzed. The master-slave computing system, called 'Hediy', has one master and twenty slave quad-core processors and runs the Matlab distributed computing software in Linux operating system.

CHAPTER 9

Design Optimization of the STAHV

9.1 Introduction

An articulated heavy vehicle (AHV) with a tractor and a semitrailer combination is designed to investigate the efficacy of the proposed design method discussed in Chapter 7. The AHV is designed using the 5 DOF model and the resulting optimal design is discussed and compared with the baseline design. The active safety system of the optimal design includes an integrated control system which have three subsystems, namely, active trailer steering (ATS), differential braking (DB) and anti-roll (AR).

9.2 Optimizer Specifications

The genetic algorithm (GA), used in the design optimization of the AHV, has the following specifications. The fraction of the population at the next generation, excluding the elite children, to be created by the crossover function takes the value of 0.8. In each subpopulation, only 20% of the individuals are allowed to migrate to a different subpopulations. If there is no improvement observed in the objective function, GA is still permitted to continue to run. Also, there is no overall time limit for the genetic algorithm. The algorithm will stop if the improvement in the objective function is less than 10^{-12} over 50 consecutive generations. The

population size of this problem takes the value of 736 (calculated as 8 times available number of workers 92 during the time of the computation) and the number of generations is 100. It is confirmed through a number of runs of the optimization problem that there is no significant improvement of the objective function after the 100th generation.

9.3 Design Variables

The design variables $\mathbf{X}$, as mentioned in equation (7.2.1), consists of with three subsets, including passive design variables $\mathbf{X}_{SYS}$, active design variables $\mathbf{X}_{CON}$, and driver model parameters $\mathbf{X}_{DR}$. The passive design variables $\mathbf{X}_{SYS}$, in the design optimization problem of the STAHV, include the sprung mass of trailer m_{s2}, roll moment of inertia of trailer I_{xx2}, yaw moment of inertia of trailer I_{zz2}, height of roll center of trailer sprung mass h_{r2}, height of trailer sprung mass CG h_{s2}, horizontal distance between the trailer sprung mass CG and coupling point l_{c2}, height of the coupling point connecting the tractor and the trailer h_{c2}, and trailer wheelbase b_2. Note that, as previously mentioned, the AHV with a tractor and a single semitrailer has the following axle groups: the tractor has one front axle and two rear axles; the semitrailer has two rear axles. The wheelbase of the semitrailer is measured as the horizontal distance between the coupling point and the middle point between the two rear axles. The passive design variables $\mathbf{X}_{SYS}$ are allowed to vary by 5% of their nominal values in this design optimization problem.

From equation (7.2.1), the design variable set also includes the control design variable set $\mathbf{X}_{CON}$ which includes $\mathbf{X}_{RWA}$ and $\mathbf{X}_{PFOT}$ as shown in equation (7.2.2). $\mathbf{X}_{RWA}$ and $\mathbf{X}_{PFOT}$ are defined as

$$\mathbf{X}_{RWA} = \begin{bmatrix} q_{RWA1} & q_{RWA2} & \dots & q_{RWAi} \end{bmatrix}, \qquad \text{where, } i = 1, 2, \dots, 8 \tag{9.3.1a}$$

$$\mathbf{X}_{PFOT} = \begin{bmatrix} q_{PFOT1} & q_{PFOT2} & \dots & q_{PFOTi} \end{bmatrix}, \qquad \text{where, } i = 1, 2, \dots, 16 \tag{9.3.1b}$$

The above weighting factor sets are from (6.3.27) and (6.3.31), respectively. The driver model design variable set consists of two subsets $\mathbf{X}_{DR}$ and $\mathbf{X}_{DP}$. The driver

model design variables are permitted to vary by 50% of their corresponding nominal values. Elements of these two subsets are described as follows,

$$\mathbf{X}_{DRh} = \begin{bmatrix} K_{ph} & t_{pv} \end{bmatrix} \tag{9.3.2a}$$

$$\mathbf{X}_{DRl} = \begin{bmatrix} K_{pl} & K_{il} & K_{dl} \end{bmatrix} \tag{9.3.2b}$$

where K_{ph} and t_{pv} denote the proportional gain and preview time of the driver model for the HSLC and the LSLC simulation, respectively, K_{pl}, K_{il}, and K_{dl} are the proportional, integral, and differential gains of the driver model for the LSPF simulation, accordingly.

For the purpose of comparison, the nominal and optimal design variables are listed in Table 9.1.

Table 9.1: Comparison of the baseline and optimal design variables of the STAHV

Design variables	***Units***	***Nominal values***	***Lower bounds***	***Upper bounds***	***Optimal values***
m_{s2}	m	30821	29279.95	32362.05	32018.76193
I_{xx2}	$kg\ m^2$	42025.2	39923.94	44126.46	42180.33365
I_{zz2}	$kg\ m^2$	226271.79	214958.2005	237585.3795	215834.8697
h_{r2}	m	0.723	0.68685	0.75915	0.689161
h_{s2}	m	0.9	0.855	0.945	0.933337
l_{c2}	m	5.853	5.56035	6.14565	5.611822
h_{c2}	m	1.1	1.045	1.155	1.146134
b_2	m	1.147	1.08965	1.20435	1.197419
$\log_{10} q_{RWA1}$		1.0	-10.0	10.0	0.376976
$\log_{10} q_{RWA2}$		1.0	-10.0	10.0	-0.641513
$\log_{10} q_{RWA3}$		1.0	-10.0	10.0	1.170486
$\log_{10} q_{RWA4}$		1.0	-10.0	10.0	-0.667056
$\log_{10} q_{RWA5}$		1.0	-10.0	10.0	2.152573
$\log_{10} q_{RWA6}$		1.0	-10.0	10.0	0.831506
$\log_{10} q_{RWA7}$		1.0	-10.0	10.0	1.698502

continued on next page

Table 9.1 – continued from previous page

Design variables	*Units*	*Nominal values*	*Lower bounds*	*Upper bounds*	*Optimal values*
$\log_{10} q_{RWA8}$		1.0	-10.0	10.0	-4.444369
$\log_{10} q_{PFOT1}$		1.0	-10.0	10.0	0.922051
$\log_{10} q_{PFOT2}$		1.0	-10.0	10.0	-0.683988
$\log_{10} q_{PFOT3}$		1.0	-10.0	10.0	6.185944
$\log_{10} q_{PFOT4}$		1.0	-10.0	10.0	0.042943
$\log_{10} q_{PFOT5}$		1.0	-10.0	10.0	-0.159616
$\log_{10} q_{PFOT6}$		1.0	-10.0	10.0	-1.112781
$\log_{10} q_{PFOT7}$		1.0	-10.0	10.0	3.201031
$\log_{10} q_{PFOT8}$		1.0	-10.0	10.0	-0.895296
$\log_{10} q_{PFOT9}$		1.0	-10.0	10.0	2.546962
$\log_{10} q_{PFOT10}$		1.0	-10.0	10.0	1.039366
$\log_{10} q_{PFOT11}$		1.0	-10.0	10.0	0.930585
$\log_{10} q_{PFOT12}$		1.0	-10.0	10.0	0.346828
$\log_{10} q_{PFOT13}$		1.0	-10.0	10.0	0.579086
$\log_{10} q_{PFOT14}$		1.0	-10.0	10.0	1.527362
$\log_{10} q_{PFOT15}$		1.0	-10.0	10.0	-7.818665
$\log_{10} q_{PFOT16}$		1.0	-10.0	10.0	2.193783
t_{pv}	sec	0.4	0.2	0.6	0.38202
K_{ph}		1.0	0.5	1.5	0.730553
K_{pl}		4.0	2.0	6.0	2.752962
K_{il}		0.1	0.05	0.15	0.115527
K_{dl}		0.1	0.05	0.15	0.12355

9.4 Simulation Results for the HSLC Maneuver

For the purpose of comparison, Table 9.2 lists the performance measures for the optimal design together with those for the baseline design. For the optimal and baseline cases, the selected vehicle dynamic responses are illustrated in Figures 9.1 and 9.8. Figures 9.1 and 9.2 show the time history of the lateral accelerations at the tractor and semitrailer CG in the HSLC maneuver for the baseline design and optimal design, respectively. Due to the RWA control mode of the ASS and the optimal passive design variables derived from the proposed method, the RWA ratio of the optimal design decreases 34.57% from the baseline value of 1.1432 to 0.9063. The drop of the RWA ratio will greatly improve the high-speed lateral stability of the resulting optimal design.

Figures 9.3 and 9.4 provide useful simulation results for investigating whether the trailer can follow the tractor's trajectory accurately in the HSLC maneuver. Compared with the baseline design, in the case of the optimal design, the trailer follows the tractor's path more accurately with the transient off-tracking of 0.0440 m, decreasing 80.07% from the corresponding baseline value of 0.1159 m. The results shown in Figure 9.2, 9.4, and 9.6 imply that with respect to the baseline design, the optimal design has higher lateral stability and the trailer can more accurately follow the tractor's path in high-speed obstacle avoidance maneuver.

Figures 9.5 and 9.6 present the time history of the sprung mass yaw rate of each vehicle unit under the HSLC maneuver for the baseline and optimal design case, respectively. The maximum peak value of the sprung mass yaw rate is decreased by 26.64% from 0.0961 rad/sec in the baseline design case to 0.0705 rad/sec in the optimal design case.

Table 9.2: Comparison of the performance measures for the baseline and optimal design

Performance measures	***Units***	***Nominal values***	***Optimal values***	***Improvement***
RWA		1.1432	0.9063	34.57%
CDG_1	g	0.0054	0.0148	63.51%
CDG_2		0.0238	0.0141	40.76%
$CDGR$		0.23	1.05	93.51%
a_{peak1}	g	0.1338	0.1246	-56.79%
a_{peak2}	g	0.1665	0.1500	100.00%
$TROF$	m	0.1159	0.0440	62.04%
$PFOT$	m	2.5150	0.5012	80.07%

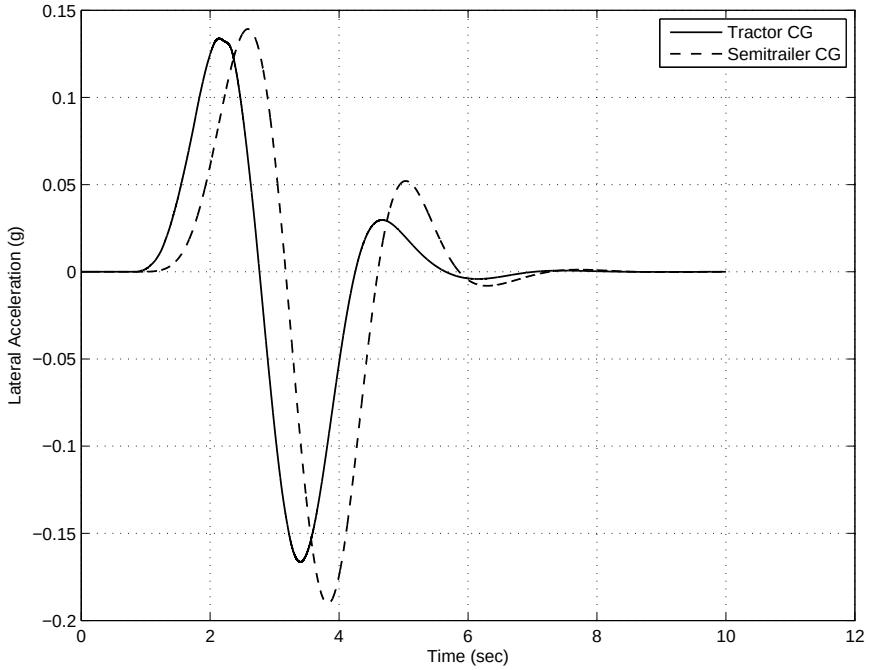

Figure 9.1: Time history of the lateral acceleration at the tractor and semitrailer CG under the HSLC maneuver for the baseline design

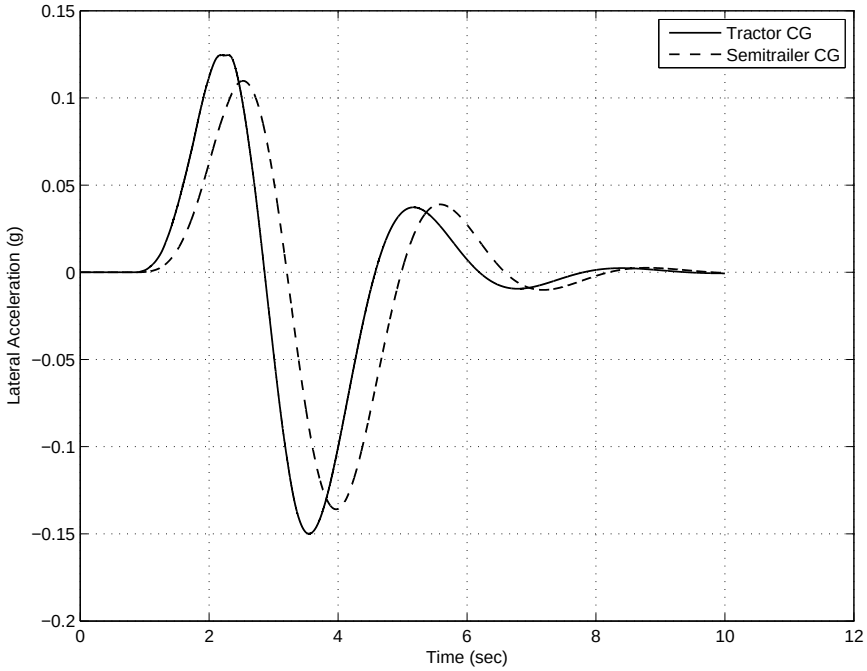

Figure 9.2: Time history of the lateral acceleration at the tractor and semitrailer CG under the HSLC maneuver for the optimal design

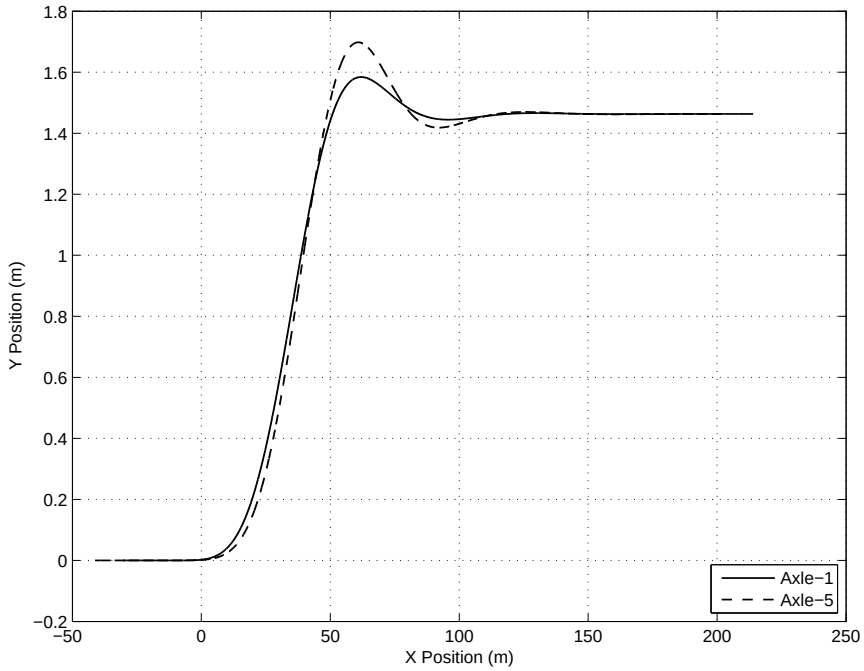

Figure 9.3: Trajectory of the tractor's front axle center and the semitrailer's rear-most axle center for the baseline design under the HSLC maneuver

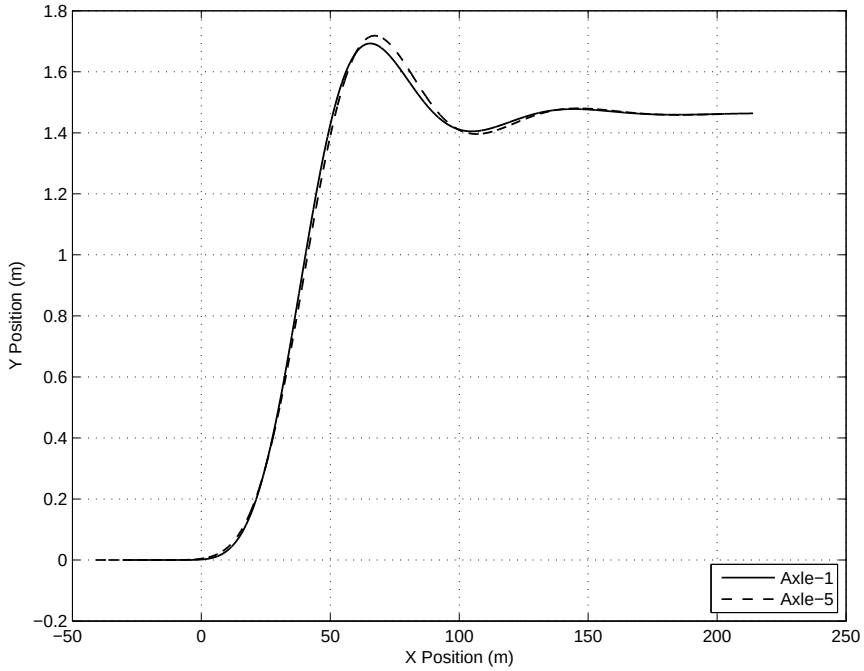

Figure 9.4: Trajectory of the tractor's front axle center and the semitrailer's rear-most axle center for the optimal design under the HSLC maneuver

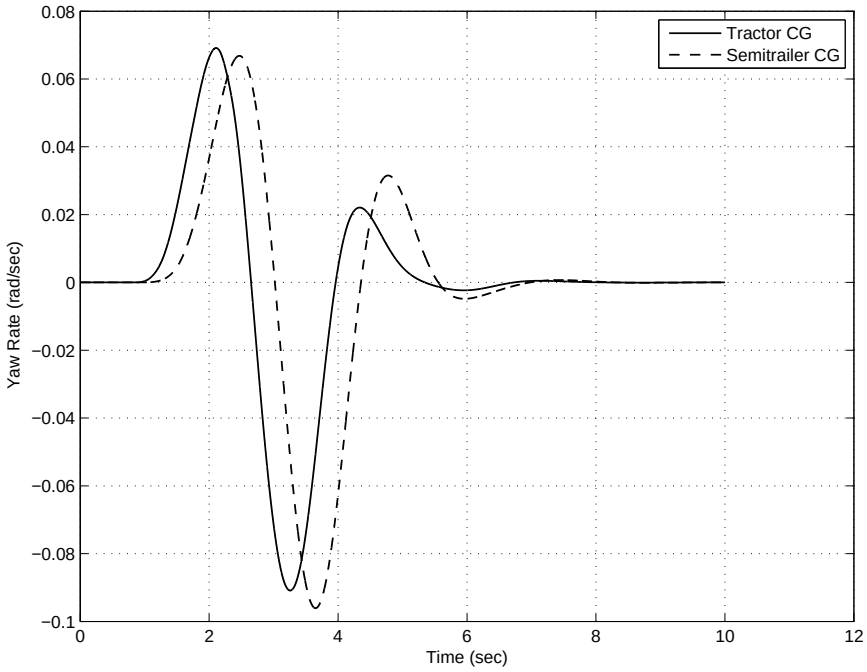

Figure 9.5: Time history of yaw rate of the tractor and semitrailer for the baseline design under the HSLC maneuver

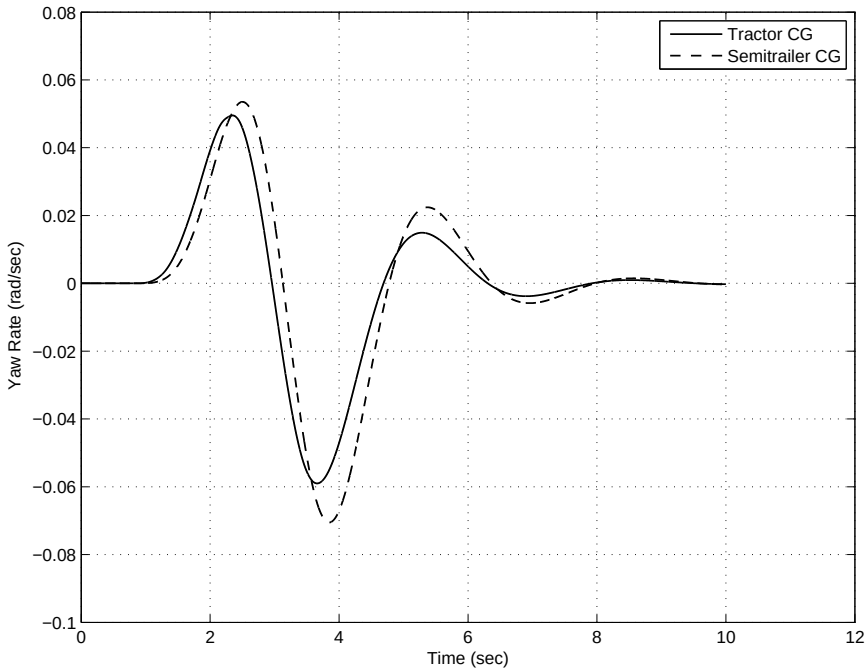

Figure 9.6: Time history of yaw rate of the tractor and semitrailer for the optimal design under the HSLC maneuver

9.5 Vehicle Dynamic Response of Low-Speed Maneuver

With the simulation results shown in Figures 9.7 and 9.8, the optimal design's low-speed maneuverability can be examined and evaluated. Figure 9.7 shows the simulation results of the baseline design, illustrating the trajectory of the tractor's front axle center and that of the semitrailer's rear axle center in the low-speed 360-degree roundabout maneuver. Figure 9.8 shows the corresponding simulation result for the optimal design. A close observation of the simulation results reveals that compared to the baseline design, for the optimal design, the trailer can track the tractor's trajectory more closely. For the optimal design, the PFOT value drops 80.07% from the baseline value of 2.52 m to 0.50 m. The low-speed performance improvement of the optimal design is attributed to the PFOT mode of active safety system controller and the optimal passive design variables derived from this design method. Regarding the active safety system power consumption,

the simulation results of the optimal design are not compared with those of the baseline design. Compared to the baseline design, the optimal design has better high-speed and low-speed performances. The improvement of the RWA ratio is calculated as follows

$$\text{Improvement} = \frac{\mid RWA_{baseline} - 1 \mid - \mid RWA_{optimal} - 1 \mid}{\mid RWA_{baseline} - 1 \mid} \times 100\% \tag{9.5.1}$$

The improvement calculation of the lateral acceleration maximum peak value a_{peak1} and minimum peak value a_{peak2} at the tractor CG is given below

$$\text{Improvement} = \frac{\mid a_{peak1\_baseline} - 0.15 \mid - \mid a_{peak1\_optimal} - 0.15 \mid}{\mid a_{peak1\_baseline} - 0.15 \mid} \times 100\% \tag{9.5.2}$$

The percentage of improvement in the cross differential gap ratio (R_{CDG}) is also calculated using equation (9.5.1). However, the path-following off-tracking (PFOT) is calculated as follows

$$\text{Improvement} = \frac{PFOT_{baseline} - PFOT_{optimal}}{PFOT_{baseline}} \times 100\% \tag{9.5.3}$$

Similarly, the cross differential gaps CDG_1 and CDG_2, transient off-tracking (TROF) are calculated from equation (9.5.2)

9.6 Summary

In this chapter, the proposed parallel design optimization (PDO) method has been implemented to the design of the active safety system for a single trailer articulated heavy vehicle (STAHV). The STAHV is designed using a 5 DOF model and the resulting optimal design is discussed and compared with the baseline design. The active safety systems of the optimal design includes an integrated control system which have three subsystems, namely, active trailer steering (ATS), differential braking (DB) and anti-roll (AR) systems.

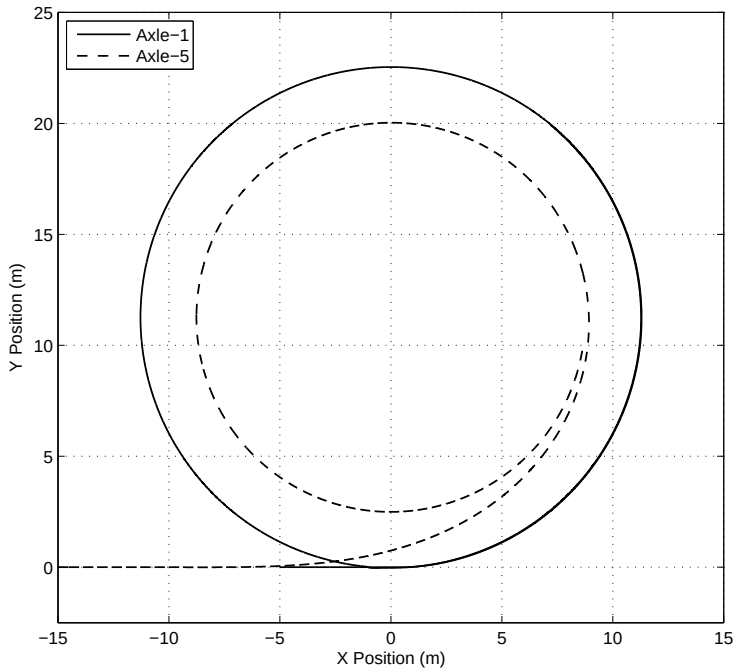

Figure 9.7: Trajectories of the tractor's front axle center and the semitrailer's rearmost axle center for the baseline design during the 360-degree roundabout turn maneuver

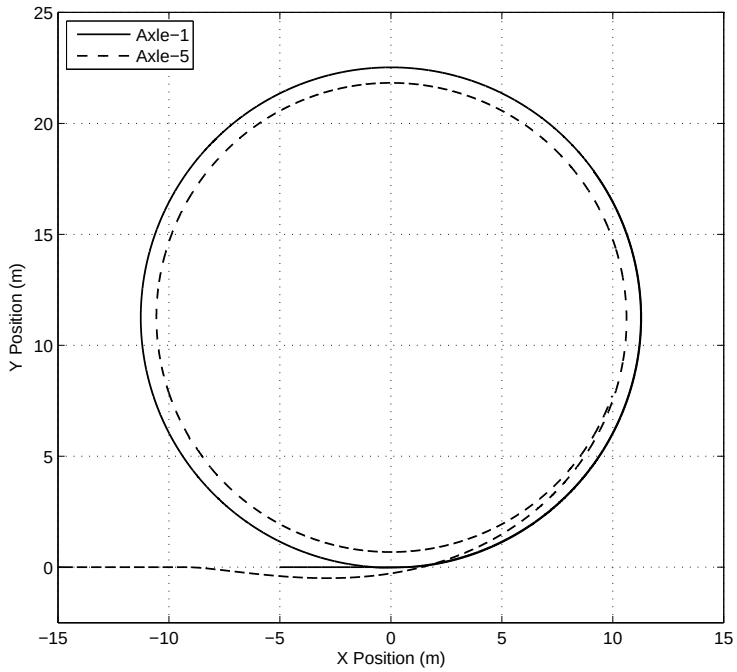

Figure 9.8: Trajectories of the tractor's front axle center and the semitrailer's rearmost axle center for the optimal design during the 360-degree roundabout turn maneuver

CHAPTER 10

Design Optimization of the MTAHV

10.1 Introduction

To examine the effectiveness of the proposed design method, in chapter A, it has been applied to the design of the multi-trailer articulated heavy vehicle (MTAHV) and the resulting optimal design is compared with the baseline design. Whereas, in this chapter, the proposed design method is applied to the design of the MTAHV. The active safety system of the optimal design includes an integrated control system which has three subsystems, namely, active trailer steering (ATS), differential braking (DB) and anti-roll (AR). The simulation results derived from the baseline design and the resulting optimal design are discussed and compared.

10.2 Optimizer Specifications

In the design optimization of the MTAHV, the optimizer, i.e., the GA, has the following specifications. The fraction of the population at the next generation, excluding elite children, to be created by the crossover function takes the value of 0.8. In each subpopulation, 20% of the individuals are permitted to migrate to a different subpopulations. There is no time limit to stop the algorithm if there is no improvement observed in the objective function. The genetic algorithm is free to run without any overall time limit. The algorithm is permitted to run until the

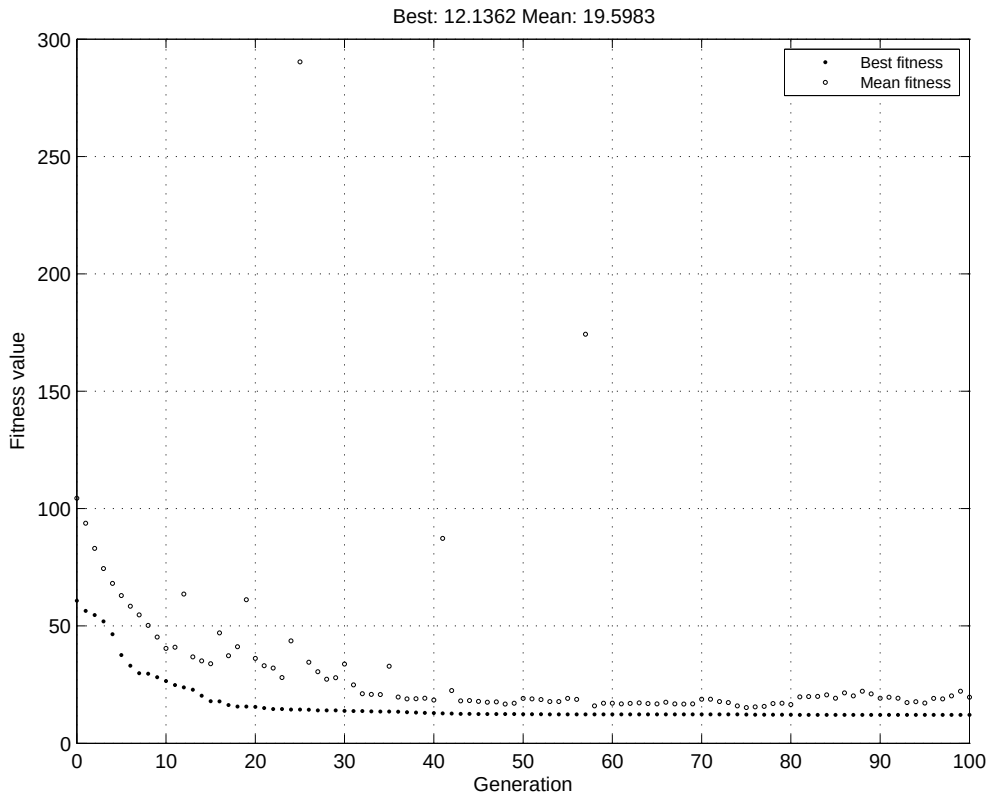

Figure 10.1: Best and mean values of fitness function in each generation during the design optimization of the MTAHV

cumulative change in the fitness function value over 50 consecutive generations is less than 10^{-12}. The value of the population size in this optimization is taken the value of 860 (calculated as 10 times the number of available workers during the computation). With numerous GA runs of the given design problem, it is observed that with the given population size, there is no significant improvement in best fitness function after the algorithm reaches the 100th generation. Therefore, the maximum number of generations is used as the principle stopping criteria. The algorithm halts if the number of generations exceeds the value of 100. Figure 10.1 shows the best and mean values of fitness function in each generation during the design optimization process of the MTAHV.

10.3 Design Variables

As mentioned in equation (7.2.1), the design variables $\mathbf{X}$ consists of three subsets: passive design variables $\mathbf{X}_{SYS}$, active design variables $\mathbf{X}_{CON}$, and driver model design variables $\mathbf{X}_D$. For the design optimization of the MTAHV, passive design variables $\mathbf{X}_{SYS}$ include sprung mass of the 1st semitrailer m_{s2}, spring mass of the 2nd semitrailer m_{s3}, roll moment inertia of the 1st semitrailer I_{xx2}, roll moment of inertia of the 2nd semitrailer I_{xx3}, yaw moment of inertia of the 1st semitrailer I_{zz2}, yaw moment of inertia of the 2nd semitrailer I_{zz3}, height of roll center of the 1st semitrailer measured upwards from ground h_{r2}, height of roll center of the 2nd semitrailer measured upwards from ground h_{r3}, height of center of gravity of the 1st semitrailer measured upwards from ground h_{s2}, height of center of gravity of the 2nd semitrailer measured upwards from ground h_{s3}, height of the 1st coupling point on 1st semitrailer measured upwards from ground h_{c2}, height of coupling point of the 2nd semitrailer measured upwards from ground h_{c3}, longitudinal distance between the 1st articulation joint of the 1st semitrailer and center of gravity of its sprung mass a_2, longitudinal distance between the 2nd articulation joint of the vehicle (articulation joint of 2nd semitrailer) and sprung mass center of gravity of 2nd semitrailer a_3, longitudinal distance between sprung mass center of gravity of the 1st semitrailer and mid-axle (5th axle of the vehicle) of 1st semitrailer b_{25}, and longitudinal distance between sprung mass center of gravity of 2nd semitrailer of mid-axle (8th axle of the vehicle) of 2nd semitrailer b_{38}. Note that, as mentioned before, the MTAHV has the following axle groups: the tractor has one front and two rear axles; and each of semitrailer has three axles. In this design optimization, the variables $\mathbf{X}_{SYS}$ are permitted to vary by 10% from the nominal values.

Table 10.1: Comparison of the baseline and optimal design variables of the STAHV

Design variables	***Units***	***Nominal values***	***Lower bounds***	***Upper bounds***	***Optimal values***
m_{s2}	kg	15927	14334.3	17519.7	14568.185219

continued on next page

Table 10.1 – continued from previous page

Design variables	*Units*	*Nominal values*	*Lower bounds*	*Upper bounds*	*Optimal values*
m_{s3}	kg	15927	14334.3	17519.7	15070.274740
I_{xx2}	kg m^2	30416	27374.4	33457.6	27638.896195
I_{xx3}	kg m^2	30416	27374.4	33457.6	32378.843337
I_{zz2}	kg m^2	439992	395992.8	483991.2	445218.524130
I_{zz3}	kg m^2	439992	395992.8	483991.2	405103.099204
h_{r2}	m	0.705	0.6345	0.7755	0.764612
h_{r3}	m	0.705	0.6345	0.7755	0.688074
h_{s2}	m	1.22	1.098	1.342	1.123450
h_{s3}	m	1.22	1.098	1.342	1.114632
h_{c2}	m	1.1	0.99	1.21	0.990652
h_{c3}	m	1.1	0.99	1.21	0.994515
a_2	m	6.385	5.7465	7.0235	5.817881
a_3	m	6.385	5.7465	7.0235	5.783899
b_{25}	m	5.115	4.6035	5.6265	4.694786
b_{38}	m	5.115	4.6035	5.6265	4.988562
$\log_{10} q_{RWA1}$		1.0	-8.0	8.0	0.196625
$\log_{10} q_{RWA2}$		1.0	-8.0	8.0	-0.929001
$\log_{10} q_{RWA3}$		1.0	-8.0	8.0	-0.884759
$\log_{10} q_{RWA4}$		1.0	-8.0	8.0	0.631223
$\log_{10} q_{RWA5}$		1.0	-8.0	8.0	3.606164
$\log_{10} q_{RWA6}$		1.0	-8.0	8.0	0.998350
$\log_{10} q_{RWA7}$		1.0	-8.0	8.0	0.265600
$\log_{10} q_{RWA8}$		1.0	-8.0	8.0	1.099294
$\log_{10} q_{RWA9}$		1.0	-8.0	8.0	0.766351
$\log_{10} q_{RWA10}$		1.0	-8.0	8.0	5.398385
$\log_{10} q_{RWA11}$		1.0	-8.0	8.0	0.831419
$\log_{10} q_{RWA12}$		1.0	-8.0	8.0	-0.438720

continued on next page

Table 10.1 – continued from previous page

Design variables	*Units*	*Nominal values*	*Lower bounds*	*Upper bounds*	*Optimal values*
$\log_{10} q_{RWA13}$		1.0	-8.0	8.0	0.281042
$\log_{10} q_{RWA14}$		1.0	-8.0	8.0	0.737927
$\log_{10} q_{RWA15}$		1.0	-8.0	8.0	-0.227255
$\log_{10} q_{RWA16}$		1.0	-8.0	8.0	1.411634
$\log_{10} q_{RWA17}$		1.0	-8.0	8.0	-0.299907
$\log_{10} q_{RWA18}$		1.0	-8.0	8.0	0.635078
$\log_{10} q_{RWA19}$		1.0	-8.0	8.0	1.407860
$\log_{10} q_{RWA20}$		1.0	-8.0	8.0	3.758048
$\log_{10} q_{RWA21}$		1.0	-8.0	8.0	1.078245
$\log_{10} q_{RWA22}$		1.0	-8.0	8.0	1.721759
$\log_{10} q_{RWA23}$		1.0	-8.0	8.0	0.543992
$\log_{10} q_{RWA24}$		1.0	-8.0	8.0	0.263030
$\log_{10} q_{RWA25}$		1.0	-8.0	8.0	1.465115
$\log_{10} q_{RWA26}$		1.0	-8.0	8.0	0.043595
$\log_{10} q_{RWA27}$		1.0	-8.0	8.0	1.246121
$\log_{10} q_{RWA28}$		1.0	-8.0	8.0	2.766858
$\log_{10} q_{RWA29}$		1.0	-8.0	8.0	2.990134
$\log_{10} q_{RWA30}$		1.0	-8.0	8.0	3.372249
$\log_{10} q_{PFOT1}$		1.0	-8.0	8.0	0.722112
$\log_{10} q_{PFOT2}$		1.0	-8.0	8.0	0.978496
$\log_{10} q_{PFOT3}$		1.0	-8.0	8.0	2.646232
$\log_{10} q_{PFOT4}$		1.0	-8.0	8.0	0.519316
$\log_{10} q_{PFOT5}$		1.0	-8.0	8.0	-0.350829
$\log_{10} q_{PFOT6}$		1.0	-8.0	8.0	1.395798
$\log_{10} q_{PFOT7}$		1.0	-8.0	8.0	6.281816
$\log_{10} q_{PFOT8}$		1.0	-8.0	8.0	1.018249
$\log_{10} q_{PFOT9}$		1.0	-8.0	8.0	-0.057707

continued on next page

Table 10.1 – continued from previous page

Design variables	*Units*	*Nominal values*	*Lower bounds*	*Upper bounds*	*Optimal values*
$\log_{10} q_{PFOT10}$		1.0	-8.0	8.0	6.092912
$\log_{10} q_{PFOT11}$		1.0	-8.0	8.0	2.677128
$\log_{10} q_{PFOT12}$		1.0	-8.0	8.0	1.088435
$\log_{10} q_{PFOT13}$		1.0	-8.0	8.0	0.722346
$\log_{10} q_{PFOT14}$		1.0	-8.0	8.0	0.438267
$\log_{10} q_{PFOT15}$		1.0	-8.0	8.0	0.665007
$\log_{10} q_{PFOT16}$		1.0	-8.0	8.0	0.061858
$\log_{10} q_{PFOT17}$		1.0	-8.0	8.0	1.235650
$\log_{10} q_{PFOT18}$		1.0	-8.0	8.0	2.714576
$\log_{10} q_{PFOT19}$		1.0	-8.0	8.0	0.626764
$\log_{10} q_{PFOT20}$		1.0	-8.0	8.0	1.795413
$\log_{10} q_{PFOT21}$		1.0	-8.0	8.0	2.771835
$\log_{10} q_{PFOT22}$		1.0	-8.0	8.0	3.671376
$\log_{10} q_{PFOT23}$		1.0	-8.0	8.0	-1.018005
$\log_{10} q_{PFOT24}$		1.0	-8.0	8.0	3.511002
$\log_{10} q_{PFOT25}$		1.0	-8.0	8.0	-0.752918
$\log_{10} q_{PFOT26}$		1.0	-8.0	8.0	1.296978
$\log_{10} q_{PFOT27}$		1.0	-8.0	8.0	-0.454758
K_p		1.6	1.28	1.92	1.609088
t_{pv}	sec	0.16	0.128	0.192	0.182526
K_p		4	3.2	4.8	4.666048
K_i		0.1	0.08	0.12	0.106696
K_d		0.1	0.08	0.12	0.097499

As shown in equation (7.2.2), the active design variable set $\mathbf{X}_{CON}$ consists of two subsets, including $\mathbf{X}_{RWA}$ and $\mathbf{X}_{PFOT}$.

$$\mathbf{X}_{RWA} = \begin{bmatrix} q_{RWA1} & q_{RWA2} & \dots & q_{RWAi} \end{bmatrix}, \qquad \text{where, } i = 1, 2, \dots, 30 \tag{10.3.1a}$$

$$\mathbf{X}_{PFOT} = \begin{bmatrix} q_{PFOT1} & q_{PFOT2} & \dots & q_{PFOTi} \end{bmatrix}, \qquad \text{where, } i = 1, 2, \dots, 27 \tag{10.3.1b}$$

The above weighting factor sets are from (6.3.30) and (6.3.32), respectively. The driver model design variable set $\mathbf{X}_D$ consists of two subsets, $\mathbf{X}_{DR}$ and $\mathbf{X}_{DP}$, as described in equation 7.2.3. In the design of MTAHV, the driver model design variable set has upper and lower bound fixed as +20% and -20% varied from their corresponding nominal values. Elements of these two subsets are described as follows,

$$\mathbf{X}_{DRh} = \begin{bmatrix} K_{ph} & t_{pv} \end{bmatrix} \tag{10.3.2a}$$

$$\mathbf{X}_{DRl} = \begin{bmatrix} K_{pl} & K_{il} & K_{dl} \end{bmatrix} \tag{10.3.2b}$$

where K_{ph} and t_{pv} denote the proportional gain and preview time, respectively, of the HSLC simulation driver model. For the LSPF simulation, K_{pl}, K_{il}, and K_{dl} are the proportional, integral, and differential control gains of the driver model, respectively.

10.4 Vehicle Dynamic Response under the HSLC Maneuver

Figures 10.2 and 10.3 illustrate the time history of the lateral acceleration at the CG of the tractor and the semitrailers for the baseline and optimal designs, respectively. In the baseline case, RWA_{31} and RWA_{21} take the values of 0.8851 and 0.8666, respectively, while their counterparts in the optimal case are 0.9244 and 1.0161, accordingly. Compared with the baseline design, the optimal design is aligned with the design criterion specified in the section 7.3, requiring that the RWA ratios should approach the value of 1.0. A close observation of Table 10.1 reveals that the improvement of the RWA ratios of the optimal design may be attributed to the

smaller values of the design variables a_2 and a_3, compared to the values of these design variables in the baseline design. From the view of rigid body dynamics, the smaller values of a_2 and a_3 will make the lateral accelerations of the 1st semitrailer and the 2nd semitrailer larger, approaching that of the tractor and resulting in the RWA ratios close to 1.0. It is also observed that the center of gravity of the trailers also shifted closer to the front articulation joint in the trailer unit.

Figures 10.4 and 10.5 show the time history of the variations of the articulation angle between adjacent units under the HSLC maneuver for the baseline and optimal designs, respectively. In the baseline design, the largest peak articulation angle occurs between tractor and 1st semitrailer, taking the value of 0.04767 rad. In the optimal design the largest peak also occurs between the tractor and 1st semitrailer taking the value of 0.03099 rad improving by 34.99% compared against the baseline design. This implies that the optimal design has less chance for the jackknifing unstable motion mode than the baseline design.

The variation of the rate of the articulation angle between adjacent units under the HSLC maneuver for the baseline and optimal design case are shown in Figures 10.6 and 10.7, respectively. The peak rate of the articulation angle occurs in the joint between the tractor and the 1st semitrailer in both the baseline and optimal design. In the optimal design, this value improves 24.53% by decreasing the value from 0.1174 rad/sec to 0.0886 rad/sec in the baseline design case. This implies further improvement of yaw stability of the long combination vehicle.

Figure 10.8 and 10.9 present the time history of the yaw rate of the sprung mass of each of the vehicle units under the HSLC maneuver for the baseline and optimal designs, respectively. The largest peak value of the yaw rate occurs in the tractor unit for the baseline design which takes the value of 0.0985 rad/sec. For the optimal case, the largest peak value occurs in the 1st semitrailer sprung mass improving 12.79% by decreasing the value to 0.0859 rad/sec.

The trajectory of the center of the tractor's front axle (axle-1), center of the 1st

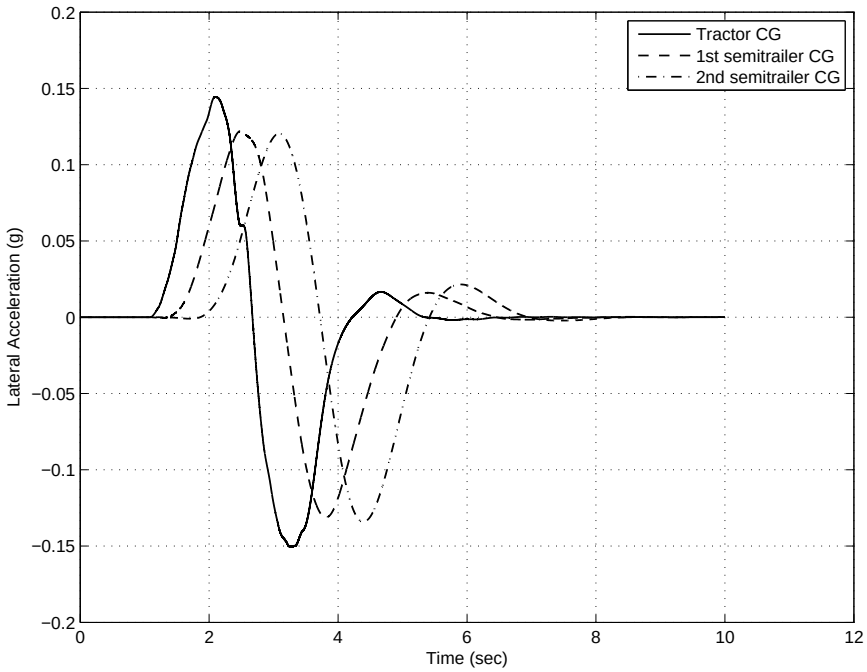

Figure 10.2: Time history of acceleration at the center of gravity of tractor, 1st semitrailer and 2nd semitrailer of passive case during lane change maneuver at high speed

semitrailer's rear axle (axle-6), and that of the 2nd semitrailer's rear axle (axle-9) are presented in Figures 10.10 and 10.11 for the baseline and optimal designs, respectively. The figures reveal that compared with the baseline design, in the case of the optimal design, the axle-9 follows the path of axle-1 more accurately with the transient off-tracking of 0.0176 m, decreasing 86.02% from the corresponding value of 0.1259 m. The maximum lateral offset between the trajectories of the center of axle-1 and that of axle-6 is improved by 68.55% by decreasing to the value of 0.0456 m for the optimal design case, from the value of 0.1450 m for the baseline design case.

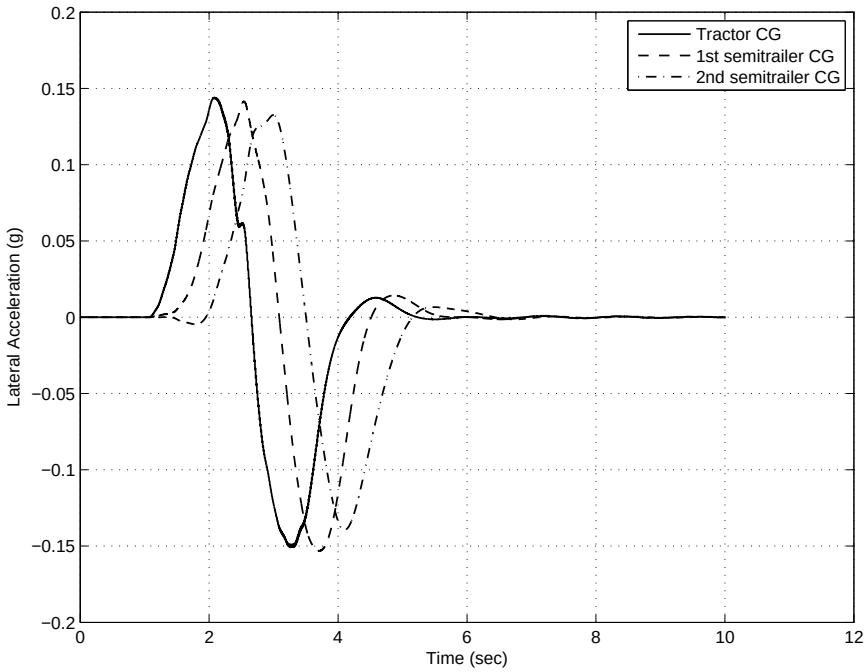

Figure 10.3: Time history of acceleration at the center of gravity of tractor, 1st semitrailer and 2nd semitrailer of optimal case during lane change maneuver at high speed

10.5 Vehicle Dynamic Responses under LSPF maneuver

Figures 10.12 and 10.13 show the trajectories of the tractor and the semitrailers during the LSPF maneuver in the baseline and optimal design case, respectively. Note that in both figures axle-1, axle-6, and axle-9 represent the tractor's front axle center, the rear axle center of the 1st semitrailer, the rear axle center of the 2nd semitrailer, respectively. For the optimal design, the PFOT, calculated from the trajectory between the center of axle-1 and that of axle-9, is 0.5704 m decreasing 92.29% from the baseline value of 7.3947 m. Similarly, the PFOT, calculated from the trajectory between the center of axle-1 and that of axle-6, is improved by 84.46% by decreasing to the value of 0.7738 m, in the optimal design case, to the value of 4.9796 m for the baseline design case.

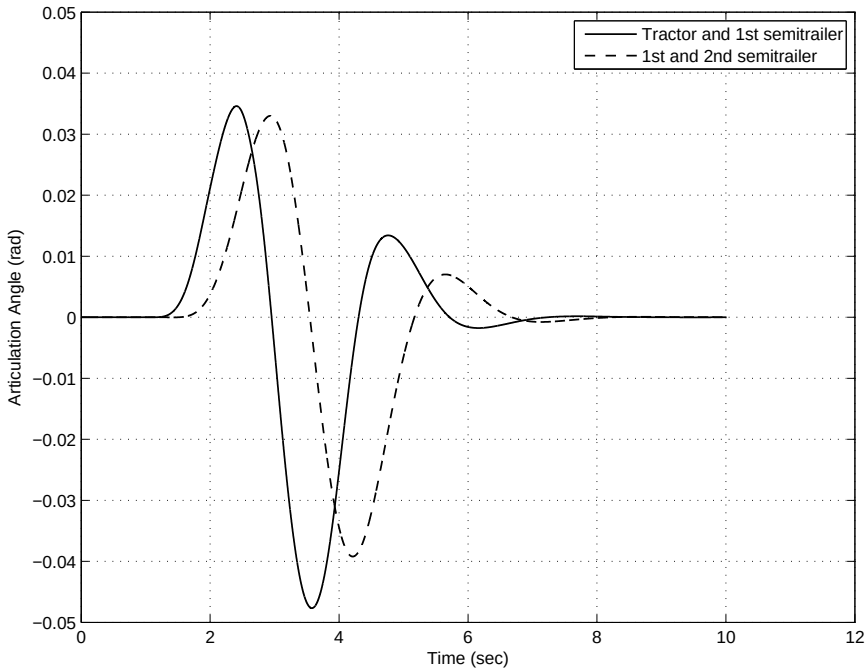

Figure 10.4: Time history of articulation angle between tractor and 1st semitrailer and that between 1st and 2nd semitrailer of passive case during lane change maneuver at high speed

10.6 Summary

The effectiveness of the proposed design method has been examined by applying the method to the design of an MTAHV with a tractor and two semitrailers combination with an active safety system. The simulation results derived from the baseline design and the optimal design method are discussed and compared. The simulation results illustrate that the proposed method is able to improve the stability at high speeds by approaching the RWA ratio (calculated between the tractor and rearmost trailer CG) by 89.30% closer to the value of 1.0. The maneuverability is improved by decreasing the value of PFOT (calculated from the center points of axle-1 and axle-9) by 83.01%

Table 10.2: Comparison of the performance measures of the baseline and optimal designs

Performance measures	***Units***	***Nominal values***	***Optimal values***	***Improvement***
RWA_{31}		0.8851	0.9244	34.20%
RWA_{21}		0.8666	1.0161	87.93%
CDG_{1_13}	g	0.0245	0.0114	53.47%
CDG_{2_13}	g	0.0174	0.0114	34.48%
R_{CDG13}		1.41	1.00	100.00%
CDG_{1_12}	g	0.0227	0.0024	89.43%
CDG_{2_12}	g	0.0202	0.0024	88.19%
R_{CDG12}		0.23	1.00	100.00%
a_{peak1}	g	0.1450	0.1508	84.00%
a_{peak2}	g	0.1514	0.1440	-328.57%
$TROF_{19}$	m	0.1259	0.0176	86.02%
$TROF_{16}$	m	0.1450	0.0456	68.55%
$PFOT_{19}$	m	7.3947	0.5704	92.29%
$PFOT_{16}$	m	4.9796	0.7738	84.46%

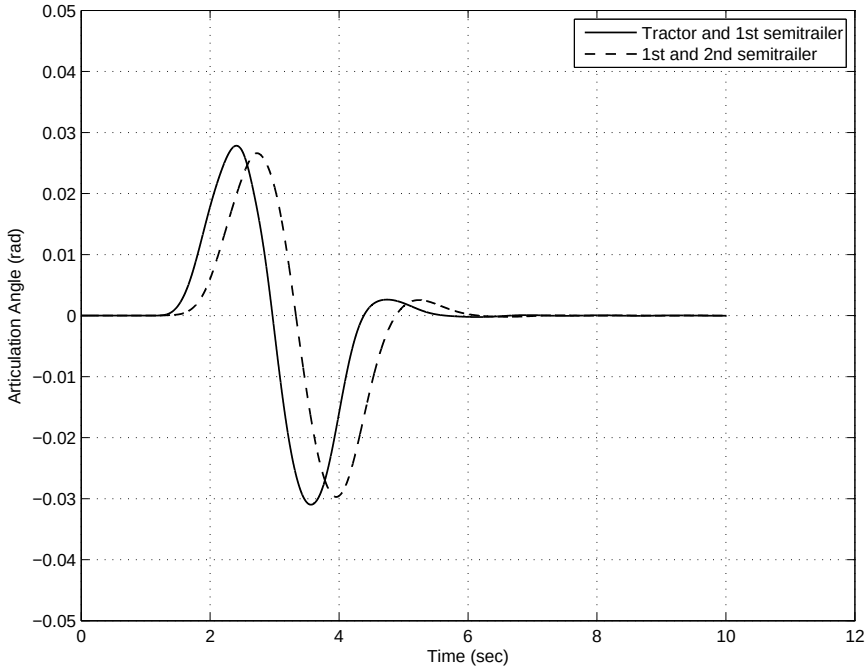

Figure 10.5: Time history of articulation angle between tractor and 1st semitrailer and that between 1st and 2nd semitrailer of optimal case during lane change maneuver at high speed

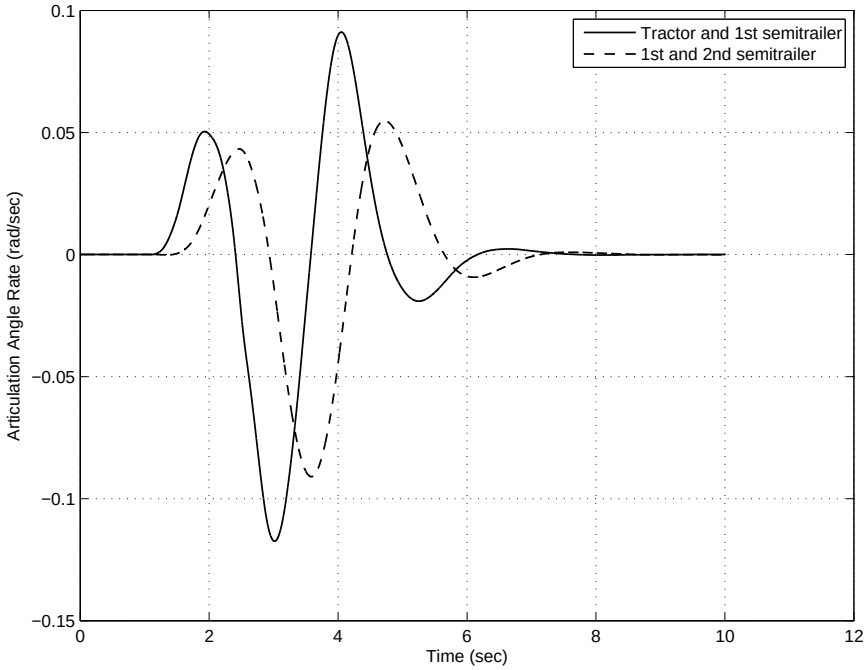

Figure 10.6: Time history of acceleration at the center of gravity of tractor and semitrailer of passive case during lane change maneuver at high speed

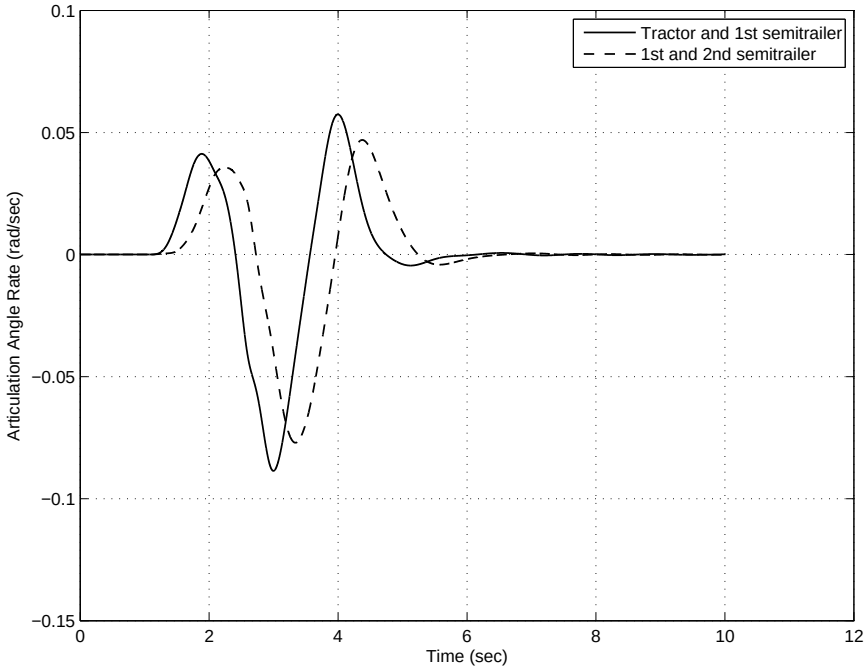

Figure 10.7: Time history of acceleration at the center of gravity of tractor and semitrailer of optimal case during lane change maneuver at high speed

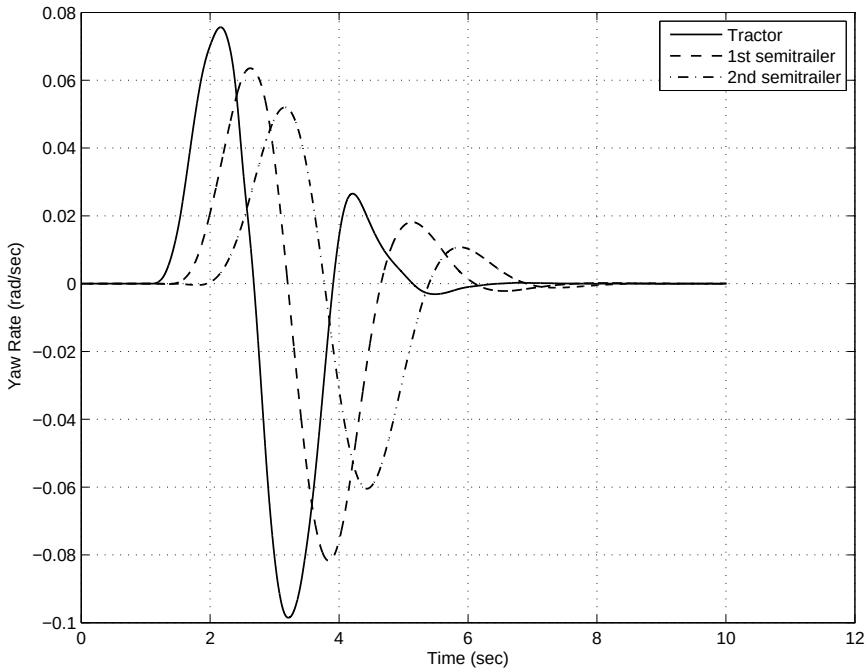

Figure 10.8: Time history of yaw rate of sprung mass of tractor, 1st semitrailer and 2nd semitrailer of passive case during lane change maneuver at high speed

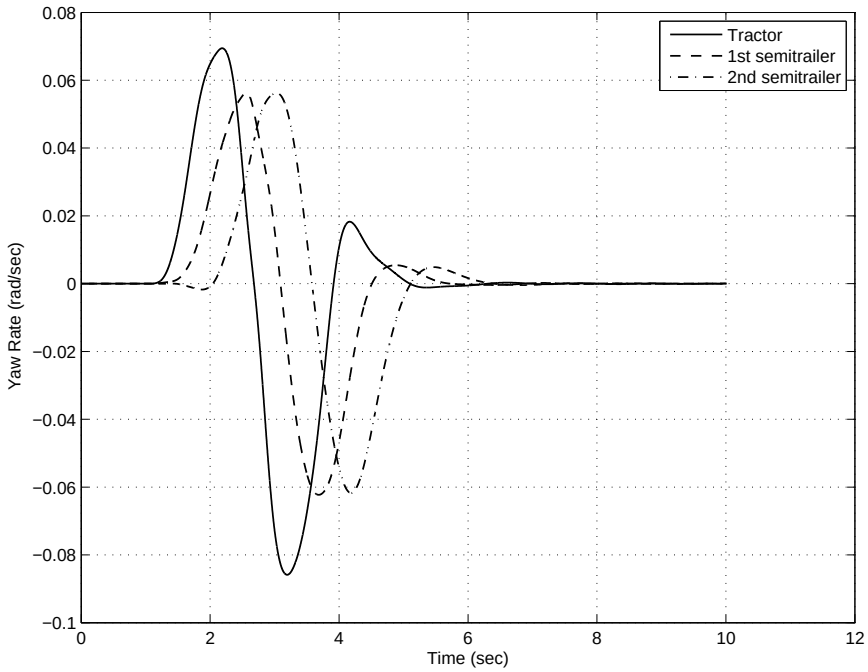

Figure 10.9: Time history of yaw rate of sprung mass of tractor, 1st semitrailer and 2nd semitrailer of optimal case during lane change maneuver at high speed

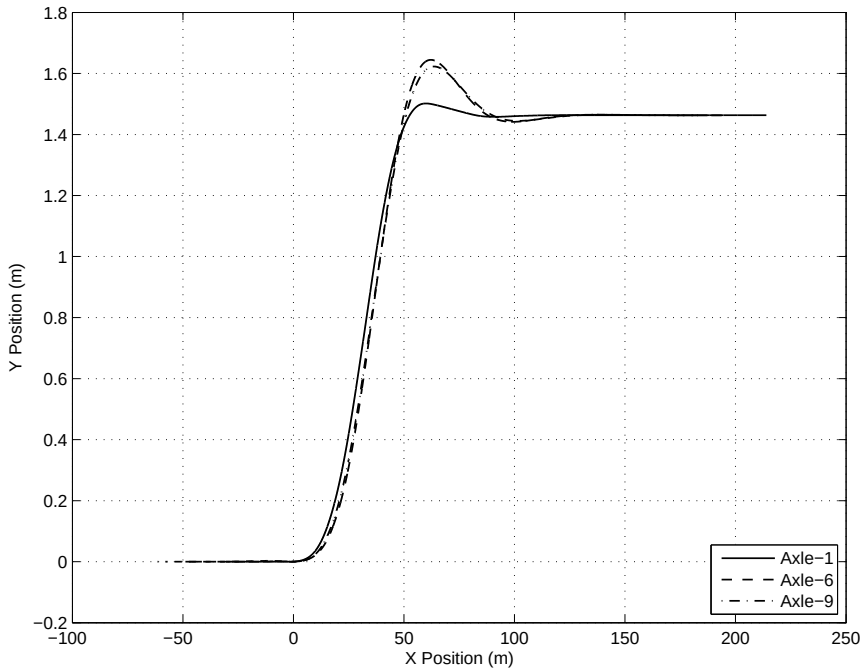

Figure 10.10: Trajectory of center of front axle (axle-1) of tractor, center of rear axle (axle-6) of 1st semitrailer and center of rear axle (axle-9) of 2nd semitrailer of passive case during lane change maneuver at high speed

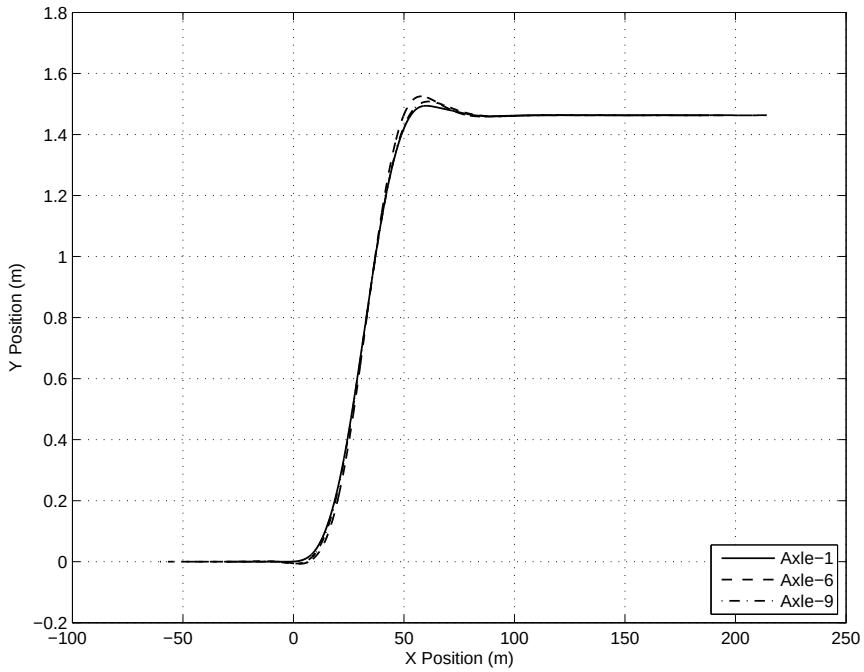

Figure 10.11: Trajectory of center of front axle (axle-1) of tractor, center of rear axle (axle-6) of 1st semitrailer and center of rear axle (axle-9) of 2nd semitrailer of optimal case during lane change maneuver at high speed

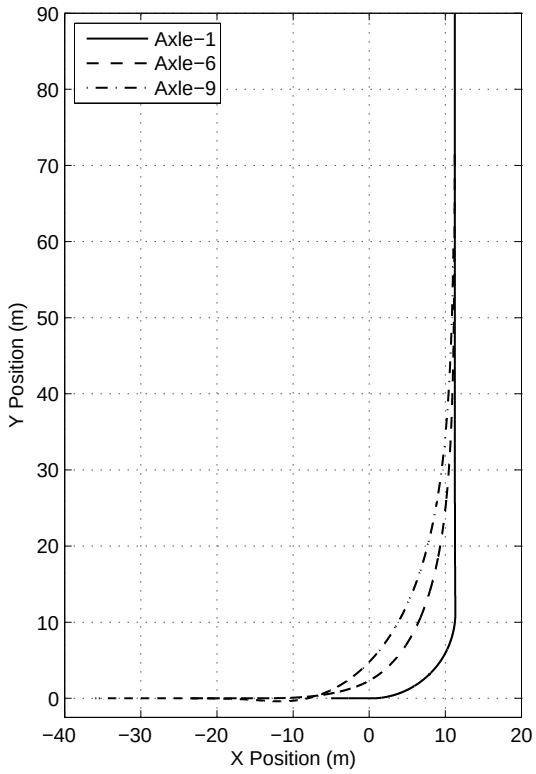

Figure 10.12: Trajectory of center of front axle (axle-1) of tractor, center of rear axle (axle-6) of 1st semitrailer and center of rear axle (axle-9) of 2nd semitrailer of passive case during 90-degree intersection turn at low speed

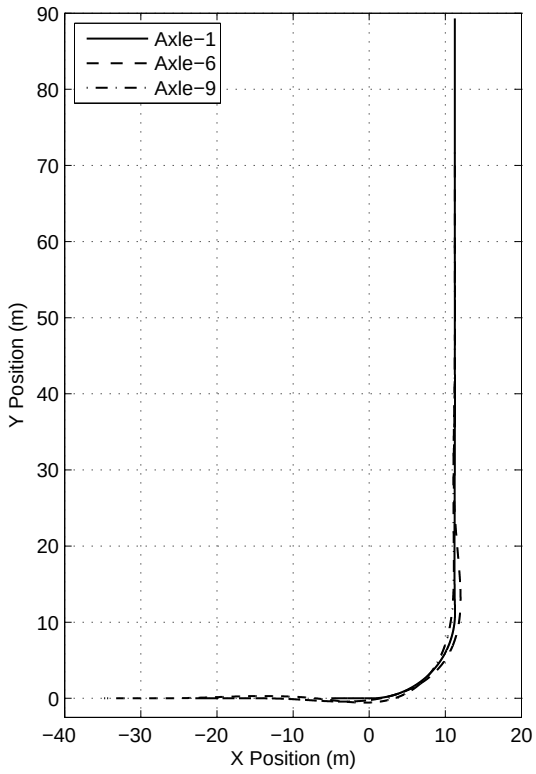

Figure 10.13: Trajectory of center of front axle (axle-1) of tractor, center of rear axle (axle-6) of 1st semitrailer and center of rear axle (axle-9) of 2nd semitrailer of optimal case during 90-degree intersection turn at low speed

CHAPTER 11

Conclusions

This thesis presents a parallel design optimization (PDO) method for multi-trailer articulated heavy vehicles (MTAHVs) with active safety systems. The proposed design method has the following features: 1) a parallel computation technique with a master-slave system is introduced to improve the computation efficiency; 2) a formulation for the optimization problem of MTAVHs with active safety systems is recommended, in which the design criteria related to directional performance measures are defined; 3) the optimal active design variables of the ASS and the optimal passive vehicle design variables are searched simultaneously in a single design loop; 4) in the design process, to evaluate the vehicle performance measures, a driver model is incorporated and it *drives* the virtual vehicle based on the well-defined test specifications; 5) the active safety system controller derived from this design method has two modes, one for improving the lateral stability at high speeds, and the other for enhancing the path-following at low speeds. With the proposed design framework using a master-slave parallel computing system, the task of vehicle system modeling, integrated controller construction, and performance evaluation and optimal design variable value selection can be assigned to a number of computers and the entire design process can be implemented in a single design loop.

The proposed design method has been applied to the design of a single trailer articulated heavy vehicle (STAHV) with an active safety system using a 5 degrees

of freedom (DOF) vehicle model and a MTAHV with a ASS using a 7 DOF vehicle model. In the design optimizations, multiple design criteria for improving the low-speed maneuverability and the high-speed stability are defined. Numerical simulation results show that the resulting optimal designs are superior to the baseline designs in the performance measures of high-speed lateral stability and low-speed path-following for both the vehicle combinations. The proposed method may be used for identifying desired design variables and predicting performance envelops in the early design stages of AHVs with active safety systems.

To further examine and improve the proposed PDO method for MTAHVs with active safety systems, the following directions for future research are recommended: 1) in order to improve the fidelity of MTAHV models (currently only hand-derived linear models have been used to test the PDO method), 3D nonlinear models, such as those developed in TruckSim, may be applied to examine the proposed method; 2) with the resulting optimal designs based on the PDO method, develop the physical prototype of the active safety systems, including active trailer steering system; and 3) test the prototype using Driver-Hardware/Software-in-the-Loop real-time simulations.

References

[1] J. Ackermann, D. Odenthal, and T. Bűnte. Advantages of Active Steering for Vehicle Dynamics Control. pages 263–270, 1999.

[2] J. Ackermann and W. Sienel. Robust Yaw Damping of Cars with Front and Rear Wheel Steering. *Control Systems Technology, IEEE Transactions on*, 1(1):15–20, March, 1993.

[3] Foreign Affairs and International Trade. Invest in Canada - Automotive 2012. `http://publications.gc.ca/pub?id=423609&sl=0`, 2012.

[4] R. Allen, T. Rosenthal, and H. Szostak. Steady State and Transient Analysis of Ground Vehicle Handling. *SAE Technical Paper 87049*, 1987, doi:10.4271/870495.

[5] C. Altafini. Path following with reduced off-tracking for multibody wheeled vehicles. *Control Systems Technology, IEEE Transactions on*, 11(4):598–605, July, 2003.

[6] R. J. Anderson and E. F. Kurtz Jr. Handling-Characteristics Simulations of Car-Trailer Systems. In *SAE Spec Publ SP-463*, pages 81–97, Recreation Vehicle Dynamic, Congr and Expo, Detroit, Michigan, 1980.

[7] InfiniBand Trade Association. Infiniband Architecture Specification, October 24, 2000.

[8] J. Aurell and S. Edlund. The Influence of Steered Axles on the Dynamic Stability of Heavy Vehicles. *SAE Paper No. 892498*, pages 612–629, 1989.

[9] J. R. Billing and C. P. Lam. Development of regulatory principles for multi-axle semitrailers. In *Second International Symposium on Heavy Vehicle Weights and Dimensions*, Kelowna, British Columbia, June 18-22, 1989.

[10] F. Braghin, F. Cheli, R. Corradi, G. Tomasini, and E. Sabbioni. Active Anti-Rollover System for Heavy-Duty Road Vehicles. *Vehicle System Dynamics*, 46(sup1):653–668, 2008.

[11] A. Bryson and Y. Ho. *Applied Optimal Control, Optimization, Estimation and Control*. Wiley, 1975.

[12] G. Burgio and P. Zegelaar. Integrated Vehicle Control using Steering and Brakes. *International Journal of Control*, 79(5):534–541, 2006.

[13] B-C. Chen and H. Peng. Differential-Braking-Based Rollover Prevention for Sport Utility Vehicles with Human-in-the-Loop Evaluations. *Vehicle System Dynamics*, 36(4-5):359–389, 2001.

[14] L. K. Chen and J. Y. Hsu. Investigation of Jack-Knife prevention in an Articulated Scaled Vehicle. *Vehicle System Dynamics*, 46(sup1):765–777, 2008.

[15] C. Cheng and D. Cebon. Improving Roll Stability of Articulated Heavy Vehicles using Active Semi-Trailer Tteering. *Vehicle System Dynamics*, 46(sup1):373–388, 2008.

[16] C. Cheng, R. Roebuck, A. Odhams, and D. Cebon. High-Speed Optimal Steering of a Tractor-Semitrailer. *Vehicle System Dynamics*, 49(4):561–593, 2011.

[17] E. Dahlberg and A. Stensson. The Dynamic Rollover Threshold - a Heavy Truck Sensitivity Study. *Int. J. of Vehicle Design*, 40(1/2/3):228 – 250, 2006.

[18] A. Dunwoody and S. Froese. Active Roll Control of a Semi-Trailer. *SAE Technical Paper 933045*, 1993, doi:10.4271/933045.

[19] J. Edgar. Development of Performance Standards for Australia Heavy Vehicles. In *Proceedings of the 8th International Symposium on Heavy Vehicle Weights and Dimensions*.

[20] D. D. Eisele and H. Peng. Vehicle Dynamics Control with Rollover Prevention for Articulated Heavy Trucks. In *Proceedings of the 5th International Symposium on Advanced Vehicle Control*, Ann Arbor, Michigan, August 2000.

[21] M. El-Gindy, M. Mrad, and X. Tong. Sensitivity of Rearward Amplification Control of a Tractor/Full Trailer to Tyre Cornering Stiffness Variations. *Proc. IMechE, Pard D: J. Automobile Engineering*, 215(5):579–588, 2001.

[22] M. El-Gindy, L. Tong, and B. Tabarrok. Frequency Response Analysis of Canadian Logging Trucks. *Vehicle System Dynamics*, 23(1):325–349, 1994.

[23] M. El-Gindy and J. Y. Wong. A Comparison of Various Computer Simulation Models for Predicting the Directional Responses of Articulated Vehicles. *Vehicle System Dynamics*, 16(5-6):249–268, 1987.

[24] P. Fancher and C. Winkler. Directional Performance Issues in Evaluation and Design of Articulated Heavy Vehicles. *Vehicle System Dynamics*, 45(7-8):607–647, 2007.

[25] P. Fancher, C. Winkler, R. Ervin, and H. Zhang. Using Braking to Control the Lateral Motions of Full Trailers. *Vehicle System Dynamics*, 29(sup1):462–478, 1998.

[26] P. S. Fancher. The Static Stability of Articulated Commercial Vehicles. *Vehicle System Dynamics*, 14(4-6):201–227, 1985.

[27] J. Gertsch and O. Eichelhard. Simulation of Dynamic Rollover Threshold for Heavy Trucks. *SAE Technical Paper 2003-01-3385*, 2003, doi:10.4271/2003-01-3385.

[28] D. Goldberg. *Genetic Algorithms in search, Optimization, and Machine Learning*. Addision-Wesley, Reading, MA, 1989.

[29] A. Goodarzi, M. Behmadi, and E. Esmailzadeh. An Optimised Braking Force Distribution Strategy for Articulated Vehicles. *Vehicle System Dynamics*, 46(sup1):849–856, 2008.

[30] T. Gordon, M. Howell, and F. Brandao. Integrated Control Methodologies for Road Vehicles. *Vehicle System Dynamics*, 40(1-3):157–190, 2003.

[31] K. Guo and H. Guan. Modelling of Driver/Vehicle Directional Control System. *Vehicle System Dynamics*, 22(3-4):141–184, 1993.

[32] M. M. He, Y.and Islam and D. Oberoi. An Design Synthesis Method for Multi-Trailer Articulated Heavy Vehicles. *Int. J. of Vehicle Performance*, (IJVP38727-ref461), in-press.

[33] Y. He and M. M. Islam. An Automated Design Method for Active Trailer Steering Systems of Articulated Heavy Vehicles. *ASME Journal of Mechanical Design*, 134(4):041002, 15 pages, 2012.

[34] Y. He, M. M. Islam, and T. D. Webster. An Integrated Design Method for Articulated Heavy Vehicles with Active Trailer Steering Systems. *SAE Int. J. of Passenger Cars-Mech. Sys.*, 3(1):158–174, 2010.

[35] Y. He and J. McPhee. A Design Methodology for Mechatronic Vehicles: Application of Multidisciplinary Optimization, Multibody and Generic Algorithms. *Vehicle System Dynamics*, 43(10):697–733, 2005.

[36] B. Hendrickson and T. G. Kolda. Graph Partitioning Models for Parallel Computing. *Parallel Computing*, 26(12):1519 – 1534, 2000. <ce:title>Graph Partitioning and Parallel Computing</ce:title>.

[37] D. Hyun and R. Langari. Modeling to Predict Rollover Threat of Tractor-Semitrailers. *Vehicle System Dynamics*, 39(6):401–414, 2003.

[38] M. M. Islam. Design Synthesis of Articulated Heavy Vehicles with Active Trailer Steering Systems. MASc thesis, University of Ontario Institute of Technology (UOIT), Oshawa, ON, Canada, April 2010.

[39] M. M. Islam, X. Ding, and Y. He. A Closed-Loop Dynamic Simulation-Based Design Method for Articulated Heavy Vehicles with Active Trailer Steering Systems. *Vehicle System Dynamics*, iFirst:1–23, 2011.

[40] M. M. Islam and Y. He. A Parallel Design Optimisation Method for Articulated Heavy Vehicles with Active Safety Systems. *to appear in Int. J. Heavy Vehicle Systems*.

[41] M. M. Islam and Y. He. Stability Optimization of Articulated Frame Steer Vehicles. In *Proceedings of 2nd CIRP Conference on Assembly Technologies and Systems (CD)*, page 11 pages, Toronto, Canada, 2008.

[42] M. M. Islam and Y. He. Design Synthesis of Heavy Articulated Vehicles with Rearward Amplification Control. In *Proceedings of the 22nd Canadian Congress of Applied Mechanics*, pages 131–132, Dalhousie University, Halifax, Canada, 2009.

[43] M. M. Islam and Y. He. An Optimal Preview Controller for Active Trailer Steering Systems of Articulated Heavy Vehicles. *SAE Technical Paper 2011-01-0983*, doi:10.4271/2011-01-0983, 2011.

[44] M. M. Islam and Y. He. Design of Articulated Heavy Vehicles with Active Safety Systems. In *International Conference on Advanced Vehicle Technologies and Integration (VTI 2012)*, Changchun, China, July 16 -19, 2012.

[45] M. M. Islam and Y. He. Design Synthesis of Articulated Heavy Vehicles with Active Safety Systems Using a Parallel Computation Technique. In *Proceedings of the CSME International Congress 2012*, Winnipeg, Manitoba, Canada, June 4-6, 2012.

[46] M. M. Islam and Y. He. Parallel Design Optimisation of Articulated Heavy Vehicles with Active Safety Systems. In *FISITA 2012 World Automotive Congress*, Beijing, China, 2012, (accepted) Manuscript ID: F2012-E13-015.

[47] M. M. Islam and Y. He. A Design Optimization Method for Multi-Trailer Articulated Heavy Vehicles with Active Safety Systems. In *23rd International Symposium on Dynamics of Vehicles on Roads and Tracks, IAVSD*, Qingdao, China, 2013, (Accepted).

[48] M. M. Islam, Y. He, and T. D. Webster. Automated Design Synthesis of Articulated Heavy Vehicles with Active Trailer Steering Systems. volume 2010, pages 29–38. ASME, 2010.

[49] M. M. Islam, Y. He, and T. D. Webster. A Compound Lateral Position Deviation Preview Controller for Active Trailer Steering Systems of Articulated Heavy Vehicles. In *Proceedings of CSME Forum 2010 (CD)*, Victoria, Birtish Columbia, Canada, 2010.

[50] W. Jianyong, T. Houjun, L. Shaoyuan, and F. Wan. Improvement of Vehicle Handling and Stability by Integrated Control of Four Wheel Steering and Direct Yaw Moment. In *Control Conference, 2007. CCC 2007. Chinese*, pages 730–735, June 26-31, 2007.

[51] B. Jujnovich and D. Cebon. Comparative Performance of Semi-Trailer Steering Systems. In *Proceedings of the 7th International Symposium on Heavy Vehicle Weights and Dimensions*, Delft, The Natherlands, June 16-20, 2002.

[52] V. Kacani, A. Stribersky, and H. Troger. Maneuverability of a Truck-Trailer Combination after Loss of Lateral Stability. *Vehicle System Dynamics*, 17(sup1):186–198, 1988.

[53] R. Karbalaei, A. Ghaffari, R. Kazemi, and S. H. Tabatabaei. Design of an Integrated AFS/DYC Based on Fuzzy Logic Control. In *Vehicular Electronics and Safety, 2007. ICVES. IEEE International Conference on*, pages 1–6, December 2007.

[54] S. Kharrazi, M. Lidberg, R. Roebuck, J. Fredriksson, and A. Odhams. Implementation of Active Steering on Longer Combination Vehicles for Enhanced Lateral Performance. *Vehicle System Dynamics*, 50(12):1949–1970, 2012.

[55] N. Kim and D. J. Cole. A Model of Driver Steering Control Incorporating the Driver's Sensing of Steering Torque. *Vehicle System Dynamics*, 49(10):1575–1596, 2011.

[56] W. Kortűm. Review of Multibody Computer, Codes for Vehicle System Dynamics. *Vehicle System Dynamics*, 22(sup1):3–31, 1993.

[57] J-H Lee, W. Chung, M. Kim, and J-B Song. A Passive Multiple Trailer System with Off-Axle Hitching. *International Journal of Control, Automation, and Systems*, 2(3):289–297, September, 2004.

[58] Z. Lozia. Rollover Thresholds of the Biaxial Truck during Motion on an Even Road. *Vehicle System Dynamics*, 29(sup1):735–740, 1998.

[59] W-H. Ma and H. Peng. Worst-Case Vehicle Evaluation Methodology— Examples on Truck Rollover/Jackknifing and Active Yaw Control Systems. *Vehicle System Dynamics*, 32:389–408, 1999.

[60] C. C. MacAdam. Application of an Optimal Preview Control for Simulation of Closed-Loop Automobile Driving. *Systems, Man and Cybernetics, IEEE Transactions on*, 11(6):393–399, June, 1981.

[61] G. Mastinu, E. Babbel, P. Lugner, D. Margolis, P. Mittermayr, and B. Richter. Integrated Controls of Lateral Vehicle Dynamics. *Vehicle System Dynamics*, 23(sup1):358–377, 1994.

[62] A. J. P. Miege and D. Cebon. Optimal Roll Control of an Articulated Vehicle: Theory and Model Validation. *Vehicle System Dynamics*, 43(12):867–884, 2005.

[63] E. Mikulcik. The Dynamics of Tractor-Semitrailer Vehicles: The Jackknifing Problem. *SAE Technical Paper 710045*, 1971, doi:10.4271/710045.

[64] B. P. Minaker and R. J. Rieveley. Automatic Generation of the Non-Holonomic Equations of Motion for Vehicle Stability Analysis. *Vehicle System Dynamics*, 48(9):1043–1063, 2010.

[65] V. K. Naik, S. K. Setia, and M. S. Squillante. Processor Allocation in Multiprogrammed Distributed-Memory Parallel Computer Systems. *Journal of Parallel and Distributed Computing*, 46(1):28 – 47, 1997.

[66] D. Oberoi, M. M. Islam, and Y. He. Dsign Optimization of Articulated Heavy Vehicles using Genetic Algorithms and Multibody Vehicle Models. In *Proceedings of 23rd Canadian Congress of Applied Mechanics*, Vancouver, BC, Canada, 2011.

[67] A. M. C. Odhams, R. L. Roebuck, D. Cebon, and C. B. Winkler. Dynamic Safety of Active Trailer Steering Systems. *Proc. IMechE, Pard E: J. of Multi-body Dynamics*, 222(4):367–380, 2008.

[68] Society of Automotive Engineers. *A Test for Evaluating the Rearward Amplification of Multi-Articulated Vehicles*. Number SAE Recommended Practice J2179. Warrendale, USA, 1994.

[69] Society of Automotive Engineers. *Road vehicles - Heavy commercial vehicle combinations and articulated buses - Lateral stability test methods*. Number ISO 14791:2000-04 (E). 2000.

[70] Traffic Injury Research Foundation of Canada. 43rd Annual Report. `http://http://www.tirf.ca/publications/PDF_publications/annual_report_05.pdf`, 2005.

[71] Ministry of Transportation The Govt. of Ontario. Ontario Long Combination Vehicle (LCV) Program. `http://www.mto.gov.on.ca/english/trucks/lcv/program-conditions/general-permit-conditions.shtml`, March 10, 2010.

[72] L. Palkovics and M. El-Gindy. Design of an Active Unilateral Brake Control System for Five-Axle Tractor-Semitrailer Based on Sensitivity Analysis. *Vehicle System Dynamics*, 24(10):725–758, 1995.

[73] A. J. Pick and D. J. Cole. Neuromuscular Dynamics in the Driver-Vehicle System. *Vehicle System Dynamics*, 44(sup1):624–631, 2006.

[74] M. Plöchl and J. Edelmann. Driver Models in Automobile Dynamics Application. *Vehicle System Dynamics*, 45(7):699–741, 2007.

[75] H. Prem, E. Ramsay, J. Pont, J. McLean, and J. Woodrooffe. Comparison of Modelling Systems for Performance-Based Assesments of Heavy Vehicles (Performance Based Standards-NRTC/Austroads Project A3 and A4). Technical report, The National Road Transport Commission (NRTC), Melbourne, October 2001.

[76] S. Rakheja. Estimation of Rollover Threshold of Partially Filled Tank Trucks. *Proceedings of the Institution of Mechanical Engineers, Part D: Journal of Automobile Engineering*, 205(1):69–71, 1991.

[77] K. Rangavajhula and H-S Tsao. Active Steering Control of an Articulated System with a Tractor and Three Full Trailers for Tractor-Track Following. *International Journal of Heavy Vehicle Systems*, 14(3):271–293, 2007.

[78] K. Rangavajhula and H-S Tsao. Command Steering of Trailers and Command-Steering-Based Optimal Control of an Articulated System for Tractor-Track Following. *Proc. IMechE, Part D: Journal of Automobile Engineering*, 222:935–954, 2008.

[79] G. Reymond, A. Kemeny, J. Droulez, and A. Berthoz. Role of Lateral Acceleration in Curve Driving: Driver Model and Experiments on a Real Vehicle and a Driving Simulator. *Human Factors: The Journal of the Human Factors and Ergonomics Society*, 43(3):483–495, Fall 2001.

[80] R. Rieveley, B. Minaker, M. Maurini, I. Shallvari, and J. Laport. Development of an Advanced Driver Model and Simulation Environment for Automotive Racing. *SAE Int. J. Passeng. Cars - Mech. Syst.*, 2(1):636–644, 2009.

[81] D. J. M. Sampson and D. Cebon. Achievable Roll Stability of Heavy Road Vehicles. *Proc. Instn Mech. Engrs. Part D: J. Automobile Engineering*, 217(2003):269–287.

[82] D. J. M. Sampson and D. Cebon. Achievable Roll Stability of Heavy Road Vehicles. *J. of Automob. Eng.*, 217(4):269–287, 2003.

[83] E. N. Sanchez, L. J. Ricalde, R. Langari, and D. Shahmirzadi. Rollover Prediction and Control in Heavy Vehicles Via Recurrent High Order Neural Networks. *Intelligent Automation & Soft Computing*, 17(1):95–107, 2011.

[84] M. W. Sayers and D. Han. A Generic Multibody Vehcile Model for Simulating Handling and Braking. *Vehicle System Dynamics*, 25(sup1):599–613, 1996.

[85] J. F. Schulman. Heavy Truck Weight and Dimension Limits in Canada. Technical report, The Railway Associaltion of Canada, 2003.

[86] R. Shamim, M. M. Islam, and Y. He. A Comparative Study of Active Control Strategies for Improving Lateral Stability of Car-Trailer Systems. *SAE Technical Paper 2011-01-0959*, doi:10.4271/2011-01-0959, 2011.

[87] D. E. Smith and J. M. Starkey. Effects of Model Complexity on the Performance of Automated Vehicle Steering Controllers: Controller Development and Evaluation. *Vehicle System Dynamics*, 23(1):627–645, 1994.

[88] D. E. Smith and J. M. Starkey. Effects of Model Complexity on the Performance of Automated Vehicle Steering Controllers: Model Development, Validation and Comparison. *Vehicle System Dynamics*, 24(2):163–181, 1995.

[89] S. Tousi, A. K. Bajaj, and W. Soedel. Closed-Loop Directional Stability of Car-Trailer Combinations in Straight-Line Motion. *Vehicle System Dynamics*, 21(1):333–360, 1992.

[90] A. Y. Ungoren and H. Peng. An Adaptive Lateral Preview Driver Model. *Vehicle System Dynamics*, 43(4):245–259, 2005.

[91] C. Winkler. Rollover of Heavy Commercial Vehicles. *UMTRI Research Review*, 31:1–17, 2000.

APPENDIX A

System Matrices of the STAHV Models

In equation (3.2.3), the system matrices $\mathbf{A} = -\mathbf{M}^{-1}\mathbf{N}$ and $\mathbf{B} = -\mathbf{M}^{-1}\mathbf{T}$. The control matrix $\mathbf{B}_u$, where $u = 1, 2, \ldots, 7$ is dependent on the active safety systems designed in Chapter 6. The control matrix $\mathbf{B_7} = -\mathbf{M}^{-1}\mathbf{P}$. The other control matrices $\mathbf{B_1}$ to $\mathbf{B_6}$ can be determined from removing relevant terms, based on the control strategies mentioned in Chapter 6, of from the matrix $\mathbf{B_7}$ for the integrated ATS, DB, and AR control. The non-zero elements of the matrices are listed below (where, $\mathbf{M}(i, j)$ denotes (i, j)-th element of matrix $\mathbf{M}$ and so on),

$$M(1,2) = m_{s1}h_{r1}l_{c1} - m_{s1}h_{s1}l_{c1} - I_{xz1}$$
$$M(1,3) = m_1 u_1 l_{c1}$$
$$M(1,4) = I_{zz1}$$

$$M(2,2) = 2m_{s1}h_{r1}^2 - 4m_{s1}h_{s1}h_{r1} + I_{xx1} - m_{s1}h_{s1}h_{cr1} + m_{s1}h_{r1}h_{cr1} + 2m_{s1}h_{s1}^2$$
$$M(2,3) = m_1 * u_1 * h_{cr1} - m_{s1}u_1 h_{s1} + m_{s1}u_1 h_{r1}$$
$$M(2,4) = -I_{xz1}$$
$$M(2,9) = -L_{r1} - L_{f1}$$

$$M(3,2) = -m_{s1} * h_{s1} + m_{s1}h_{r1}$$
$$M(3,3) = m_1 u_1$$

$$M(3,6) = m_{s2}h_{r2} - m_{s2}h_{s2}$$
$$M(3,7) = m_2u_2$$

$$M(4,6) = -I_{xz2} + l_{c2}m_{s2}h_{s2} - l_{c2}m_{s2}h_{r2}$$
$$M(4,7) = -l_{c2}m_2u_2$$
$$M(4,8) = I_{zz2}$$

$$M(5,6) = I_{xx2} - 4m_{s2}h_{s2}h_{r2} - h_{cr2}m_{s2}h_{s2} + h_{cr2}m_{s2}h_{r2} + 2m_{s2}h_{r2}^2 + 2 * m_{s2}h_{s2}^2$$
$$M(5,7) = m_{s2}u_2h_{r2} - m_{s2}u_2 * h_{s2} + h_{cr2}m_2u_2$$
$$M(5,8) = -I_{xz2}$$
$$M(5,10) = -L_{r2}$$

$$M(6,2) = -h_{c1}/u_1 + h_{r1}/u_1$$
$$M(6,3) = 1$$
$$M(6,4) = -l_{c1}/u_1$$
$$M(6,6) = h_{c2}/u_2 - h_{r2}/u_2$$
$$M(6,7) = -1$$
$$M(6,8) = -l_{c2}/u_2$$

$$M(7,9) = -L_{r1} - L_{f1}$$

$$M(8,10) = -L_{r2}$$

$$M(9,1) = 1$$

$$M(10,5) = 1$$

$$N(1,3) = -N_{\beta1} - Y_{\beta1}l_{c1}$$
$$N(1,4) = m_1u_1l_{c1} - Y_{r1}l_{c1} - N_{r1}$$

$$N(2,1) = K_{r1} + m_{s1}gh_{r1} - m_{s1}gh_{s1} + K_{f1} + K_{12}$$
$$N(2,2) = L_{f1} + L_{r1}$$
$$N(2,3) = -Y_{\beta 1}h_{cr1}$$
$$N(2,4) = m_1u_1h_{cr1} - Y_{r1}h_{cr1} - m_{s1}u_1h_{s1} + m_{s1}u_1h_{r1}$$
$$N(2,5) = -K_{12}$$
$$N(2,9) = -K_{r1} - K_{f1}$$

$$N(3,3) = -Y_{\beta 1}$$
$$N(3,4) = m_1u_1 - Y_{r1}$$
$$N(3,7) = -Y_{\beta 2}$$
$$N(3,8) = m_2u_2 - Y_{r2}$$

$$N(4,7) = l_{c2}Y_{\beta 2} - N_{\beta 2}$$
$$N(4,8) = -l_{c2}m_2u_2 - N_{r2} + l_{c2}Y_{r2}$$

$$N(5,1) = -K_{12}$$
$$N(5,5) = m_{s2}gh_{r2} - m_{s2}gh_{s2} + K_{12} + K_{r2}$$
$$N(5,6) = L_{r2}$$
$$N(5,7) = -h_{cr2}Y_{\beta 2}$$
$$N(5,8) = m_{s2}u_2h_{r2} + h_{cr2}m_2u_2 - h_{cr2}Y_{r2} - m_{s2}u_2h_{s2}$$
$$N(5,10) = -K_{r2}$$

$$N(6,4) = 1$$
$$N(6,8) = -1$$

$$N(7,1) = K_{f1} + K_{r1}$$
$$N(7,2) = L_{f1} + L_{r1}$$
$$N(7,9) = -K_{f1} - K_{tr1} - K_{r1} - K_{tf1}$$

$$N(8,5) = K_{r2}$$

$N(8,6) = L_{r2}$
$N(8,10) = -K_{r2} - K_{tr2}$

$N(9,2) = -1$

$N(10,6) = -1$

$P(1,1) = -1$

$P(2,3) = -1$

$P(3,5) = -Y_{\delta 2f}$
$P(3,6) = -Y_{\delta 2r}$

$P(4,2) = -1$
$P(4,5) = -N_{\delta 2f} + l_{c2} * Y_{\delta 2f}$
$P(4,6) = -N_{\delta 2r} + l_{c2} * Y_{\delta 2r}$

$P(5,4) = -1$
$P(5,5) = -h_{cr2} * Y_{\delta 2f}$
$P(5,6) = -h_{cr2} * Y_{delta2r}$

$P(7,3) = -1$

$P(8,4) = -1$

$T(1,1) = -Y_{\delta 1f} l_{c1} - N_{\delta 1f}$

$T(2,1) = -Y_{\delta 1f} h_{cr1}$

$T(3,1) = -Y_{\delta 1 f}$

APPENDIX B

System Matrices of the MTAHV models

In equation (3.3.1), the system matrices $\mathbf{A} = -\mathbf{M}^{-1}\mathbf{N}$ and $\mathbf{B} = -\mathbf{M}^{-1}\mathbf{T}$. The control matrix $\mathbf{B}_u$, where $u = 1, 2, \ldots, 7$ is dependent on the active safety systems designed in Chapter 6. The control matrix $\mathbf{B_7} = -\mathbf{M}^{-1}\mathbf{P}$. The other control matrices $\mathbf{B_1}$ to $\mathbf{B_6}$ can be determined from removing relevant terms, based on the control strategies mentioned in Chapter 6, of from the matrix $\mathbf{B_7}$ for the integrated ATS, DB, and AR control. The non-zero elements of the matrices are listed below (where, $\mathbf{M}(i, j)$ denotes (i, j)-th element of matrix $\mathbf{M}$ and so on),

$M(1,2) = m_{s1} * h_{r1} * l_{c1} - m_{s1} * h_{s1} * l_{c1} - I_{xz1}$
$M(1,3) = m_1 * u_1 * l_{c1}$
$M(1,4) = I_{zz1}$

$M(2,2) = 2 * m_{s1} * h_{s1}^2 + I_{xx1} + m_{s1} * h_{r1} * h_{cr1} + 2 * m_{s1} * h_{r1}^2 - 4 * m_{s1} * h_{s1} * h_{r1} - m_{s1} * h_{s1} * h_{cr1}$
$M(2,3) = m_1 * u_1 * h_{cr1} - m_{s1} * u_1 * h_{s1} + m_{s1} * u_1 * h_{r1}$
$M(2,4) = -I_{xz1}$
$M(2,13) = -L_{f1} - L_{r1}$

$M(3,2) = -m_{s1} * h_{s1} + m_{s1} * h_{r1}$

$M(3,3) = m_1 * u_1$
$M(3,6) = -m_{s2} * h_{s2} + m_{s2} * h_{r2}$
$M(3,7) = m_2 * u_2$
$M(3,10) = -m_{s3} * h_{s3} + m_{s3} * h_{r3}$
$M(3,11) = m_3 * u_3$

$M(4,6) = -l_{c21} * m_{s2} * h_{s2} + I_{xz2} + l_{c21} * m_{s2} * h_{r2}$
$M(4,7) = l_{c21} * m_2 * u_2$
$M(4,8) = -I_{zz2}$
$M(4,10) = -l_{c21} * m_{s3} * h_{s3} + l_{c21} * m_{s3} * h_{r3} - l_{c22} * m_{s3} * h_{s3} + l_{c22} * m_{s3} * h_{r3}$
$M(4,11) = l_{c22} * m_3 * u_3 + l_{c21} * m_3 * u_3$

$M(5,6) = I_{xx2} - h_{cr2} * m_{s2} * h_{s2} + h_{cr2} * m_{s2} * h_{r2} + 2 * m_{s2} * h_{r2}^2 + 2 * m_{s2} * h_{s2}^2 - 4 * m_{s2} * h_{s2} * h_{r2}$
$M(5,7) = -m_{s2} * u_2 * h_{s2} + m_{s2} * u_2 * h_{r2} + h_{cr2} * m_2 * u_2$
$M(5,8) = -I_{xz2}$
$M(5,10) = -h_{cr2} * m_{s3} * h_{s3} + h_{cr2} * m_{s3} * h_{r3}$
$M(5,11) = h_{cr2} * m_3 * u_3$
$M(5,14) = -L_{r2}$

$M(6,10) = I_{oxz3} - m_{s3} * h_{s3} * l_{c3} + m_{s3} * h_{r3} * l_{c3}$
$M(6,11) = m_3 * u_3 * l_{c3}$
$M(6,12) = -I_{zz3}$

$M(7,9) = l_{c3} * L_{r3}$
$M(7,10) = -4 * l_{c3} * m_{s3} * h_{s3} * h_{r3} + l_{c3} * I_{xx3} - I_{xz3} * h_{cr3} + 2 * l_{c3} * m_{s3} * h_{r3}^2 + 2 * l_{c3} * m_{s3} * h_{s3}^2$
$M(7,11) = -l_{c3} * m_{s3} * u_3 * h_{s3} + l_{c3} * m_{s3} * u_3 * h_{r3}$
$M(7,12) = -l_{c3} * I_{xz3} + I_{zz3} * h_{cr3}$
$M(7,15) = -l_{c3} * L_{r3}$

$M(8,2) = -u_2 * h_{c1} + u_2 * h_{r1}$
$M(8,3) = u_1 * u_2$
$M(8,4) = -u_2 * l_{c1}$
$M(8,6) = u_1 * h_{c2} - u_1 * h_{r2}$
$M(8,7) = -u_1 * u_2$
$M(8,8) = -u_1 * l_{c21}$

$M(9,6) = -u_3 * h_{c2} + u_3 * h_{r2}$
$M(9,7) = u_2 * u_3$
$M(9,8) = -u_3 * l_{c22}$
$M(9,10) = u_2 * h_{c3} - u_2 * h_{r3}$
$M(9,11) = -u_2 * u_3$
$M(9,12) = -u_2 * l_{c3}$

$M(10,13) = -L_{f1} - L_{r1}$

$M(11,14) = -L_{r2}$

$M(12,9) = L_{r3}$
$M(12,15) = -L_{r3}$

$M(13,1) = 1$

$M(14,5) = 1$

$M(15,9) = 1$

$N(1,3) = -N_{\beta 1} - Y_{\beta 1} * l_{c1}$
$N(1,4) = m_1 * u_1 * l_{c1} - Y_{r1} * l_{c1} - N_{r1}$

$$N(2,1) = K_{12} + K_{f1} - m_{s1} * g * h_{s1} + m_{s1} * g * h_{r1} + K_{r1}$$
$$N(2,3) = -Y_{\beta 1} * h_{cr1}$$
$$N(2,4) = -Y_{r1} * h_{cr1} - m_{s1} * u_1 * h_{s1} + m_1 * u_1 * h_{cr1} + m_{s1} * u_1 * h_{r1}$$
$$N(2,5) = -K_{12}$$
$$N(2,13) = -K_{r1} - K_{f1}$$

$$N(3,3) = -Y_{\beta 1}$$
$$N(3,4) = m_1 * u_1 - Y_{r1}$$
$$N(3,7) = -Y_{\beta 2}$$
$$N(3,8) = -Y_{r2} + m_2 * u_2$$
$$N(3,11) = -Y_{\beta 3}$$
$$N(3,12) = m_3 * u_3 - Y_{r3}$$

$$N(4,7) = -Y_{\beta 2} * l_{c21} + N_{\beta 2}$$
$$N(4,8) = N_{r2} - Y_{r2} * l_{c21} + l_{c21} * m_2 * u_2$$
$$N(4,11) = -l_{c21} * Y_{\beta 3} - l_{c22} * Y_{\beta 3}$$
$$N(4,12) = -l_{c22} * Y_{r3} - l_{c21} * Y_{r3} + l_{c22} * m_3 * u_3 + l_{c21} * m_3 * u_3$$

$$N(5,1) = -K_{12}$$
$$N(5,5) = K_{23} + m_{s2} * g * h_{r2} - m_{s2} * g * h_{s2} + K_{12} + K_{r2}$$
$$N(5,7) = -Y_{\beta 2} * h_{cr2}$$
$$N(5,8) = -m_{s2} * u_2 * h_{s2} + h_{cr2} * m_2 * u_2 - Y_{r2} * h_{cr2} + m_{s2} * u_2 * h_{r2}$$
$$N(5,9) = -K_{23}$$
$$N(5,11) = -h_{cr2} * Y_{\beta 3}$$
$$N(5,12) = h_{cr2} * m_3 * u_3 - h_{cr2} * Y_{r3}$$
$$N(5,14) = -K_{r2}$$

$$N(6,11) = -Y_{\beta 3} * l_{c3} + N_{\beta 3}$$
$$N(6,12) = m_3 * u_3 * l_{c3} - Y_{r3} * l_{c3} + Nr3$$

$$N(7,5) = -l_{c3} * K_{23}$$

$$N(7,9) = -l_{c3} * m_{s3} * g * h_{s3} + l_{c3} * K_{r3} + l_{c3} * m_{s3} * g * h_{r3} + l_{c3} * K_{23}$$
$$N(7,11) = -N_{\beta 3} * h_{cr3}$$
$$N(7,12) = -l_{c3} * m_{s3} * u_3 * h_{s3} + l_{c3} * m_{s3} * u_3 * h_{r3} - N_{r3} * h_{cr3}$$
$$N(7,15) = -l_{c3} * K_{r3}$$

$$N(8,4) = u_1 * u_2$$
$$N(8,8) = -u_1 * u_2$$

$$N(9,8) = u_2 * u_3$$
$$N(9,12) = -u_2 * u_3$$

$$N(10,1) = K_{f1} + K_{r1}$$
$$N(10,13) = -K_{f1} - K_{tr1} - K_{r1} - K_{tf1}$$

$$N(11,5) = K_{r2}$$
$$N(11,14) = -K_{r2} - K_{tr2}$$

$$N(12,9) = K_{r3}$$
$$N(12,15) = -K_{r3} - K_{tr3}$$

$$N(13,2) = -1$$

$$N(14,6) = -1$$

$$N(15,10) = -1$$

$$P(1,1) = -1$$

$$P(2,4) = -1$$

$$P(3,7) = -Y_{\delta 2f}$$
$$P(3,8) = -Y_{\delta 2m}$$
$$P(3,9) = -Y_{\delta 2r}$$
$$P(3,10) = -Y_{\delta 3f}$$
$$P(3,11) = -Y_{\delta 3m}$$
$$P(3,12) = -Y_{\delta 3r}$$

$$P(4,2) = 1$$
$$P(4,7) = -Y_{\delta 2f} * l_{c21} + N_{\delta 2f}$$
$$P(4,8) = -Y_{\delta 2m} * l_{c21} + N_{\delta 2m}$$
$$P(4,9) = -Y_{delta2r} * l_{c21} + N_{\delta 2r}$$
$$P(4,10) = -l_{c22} * Y_{\delta 3f} - l_{c21} * Y_{\delta 3f}$$
$$P(4,11) = -l_{c22} * Y_{\delta 3m} - l_{c21} * Y_{\delta 3m}$$
$$P(4,12) = -l_{c22} * Y_{\delta 3r} - l_{c21} * Y_{\delta 3r}$$

$$P(5,5) = -1$$
$$P(5,7) = -Y_{\delta 2f} * h_{cr2}$$
$$P(5,8) = -Y_{\delta 2m} * h_{cr2}$$
$$P(5,9) = -Y_{\delta 2r} * h_{cr2}$$
$$P(5,10) = -h_{cr2} * Y_{\delta 3f}$$
$$P(5,11) = -h_{cr2} * Y_{\delta 3m}$$
$$P(5,12) = -h_{cr2} * Y_{\delta 3r}$$

$$P(6,3) = 1$$
$$P(6,10) = -Y_{\delta 3f} * l_{c3} + N_{\delta 3f}$$
$$P(6,11) = N_{\delta 3m} - Y_{\delta 3m} * l_{c3}$$
$$P(6,12) = -Y_{\delta 3r} * l_{c3} + N_{\delta 3r}$$

$$P(7,3) = -h_{cr3}$$
$$P(7,6) = -l_{c3}$$

$P(7,10) = -N_{\delta 3f} * h_{cr3}$
$P(7,11) = -N_{\delta 3m} * h_{cr3}$
$P(7,12) = -N\delta 3r * h_{cr3}$

$P(10,4) = -1$

$P(11,5) = -1$

$P(12,6) = -1$

$T(1,1) = -Y_{\delta 1f} * l_{c1} - N_{\delta 1f}$

$T(2,1) = -Y_{\delta 1f} * h_{cr1}$

$T(3,1) = -Y_{\delta 1f}$

APPENDIX C

The STAHV Parameters

1. Total mass of tractor = 6769 kg
2. Total mass of semitrailer = 32151 kg
3. Sprung mass of tractor = 4819 kg
4. Sprung mass of semitrailer = 30821 kg
5. Roll moment of inertia of tractor sprung mass, measured from the CG of tractor sprung mass = 4348.41 kgm^2
6. Roll/yaw product of inertia of tractor sprung mass, measured from the CG of tractor sprung mass = 2175.5 kgm^2
7. Yaw moment of inertia of whole mass of tractor = 20606.07 kgm^2
8. Roll moment of inertia of semitrailer sprung mass, measured from the CG of tractor sprung mass = 42025.2 kgm^2
9. Roll/yaw product of inertia of semitrailer sprung mass, measured from the CG of semitrailer sprung mass= 18497.43 kgm^2
10. Yaw moment of inertia of whole mass of semitrailer=226271.79 kgm^2
11. Height of roll center of tractor sprung mass, measured upwards from ground = 0.558 m

12. Height of roll center of semitrailer sprung mass, measured upwards from ground = 0.723 m
13. Height of CG of tractor sprung mass, measured upwards from ground = 1.058 m
14. Height of CG of semitrailer sprung mass, measured upwards from ground = 0.9 m
15. Height of coupling point on tractor, measured upwards from ground = 1.100 m
16. Height of coupling point on semitrailer, measured upwards from ground = 1.100 m
17. Distance between the whole mass CG of tractor and coupling point = 1.959 m
18. Distance between the whole mass CG of semitrailer and coupling point = 5.853 m
19. Distance between the whole sprung mass CG of tractor and front axle = 1.115 m
20. Distance between the whole sprung mass CG of tractor and rear axle set = 1.9590 m
21. Distance between the whole sprung mass CG of semitrailer and rear axle set = 1.1470 m
22. Distance between each axle of tractor = 1.27 m
23. Distance between each axle of semitrailer = 1.31 m
24. Roll stiffness of front suspension of tractor adjusted with tire vertical stiffness = 974030 Nm/rad
25. Roll stiffness of rear suspension of tractor adjusted with tire vertical stiffness = 974030 Nm/rad

26. Roll stiffness of rear suspension of semitrailer adjusted with tire vertical stiffness = 515660 Nm/rad
27. Roll damping coefficient of front suspension of tractor =160000 Nms/rad
28. Roll damping coefficient of rear suspension of tractor =160000 Nms/rad
29. Roll damping coefficient of rear suspension of semitrailer =270000 Nms/rad
30. Roll stiffness of coupling point of tractor and semitrailer = 114590 Nm/rad
31. Tire roll stiffness of front suspension of tractor =5000000 Nm/rad
32. Tire roll stiffness of rear suspension of tractor =2000000 Nm/rad
33. Tire roll stiffness of rear suspension of semitrailer =2000000 Nm/rad
34. Tire cornering coefficient of front axle of tractor = - 277200 N/rad
35. Tire cornering coefficient of rear axle set of tractor = - 740280 N/rad
36. Tire cornering coefficient of rear axle set of semitrailer = - 2646000 N/rad

APPENDIX D

The MTAHV Parameters

1. Total mass of tractor = 8258 kg
2. Total mass of first semitrailer = 17997 kg
3. Total mass of second semitrailer = 17997 kg
4. Sprung mass of tractor = 6308 kg
5. Sprung mass of first semitrailer = 15927 kg
6. Sprung mass of 2nd semitrailer = 15927 kg
7. Roll moment of inertia of tractor sprung mass, measured from the CG of tractor sprung mass = 6879 kgm^2
8. Roll/yaw product of inertia of tractor sprung mass, measured from the CG of tractor sprung mass = 130 kgm^2
9. Yaw moment of inertia of whole mass of tractor = 19665 kgm^2
10. Roll moment of inertia of first semitrailer sprung mass, measured from the CG of tractor sprung mass = 30416 kgm^2
11. Roll/yaw product of inertia of first semitrailer sprung mass, measured from the CG of semitrailer sprung mass = 0 kgm^2
12. Yaw moment of inertia of whole mass of lead semitrailer = 439992 kgm^2

13. Roll moment of inertia of second semitrailer sprung mass, measured from the CG of tractor sprung mass = 30416 kgm^2
14. Roll/yaw product of inertia of second semitrailer sprung mass, measured from the CG of semitrailer sprung mass = 0 kgm^2
15. Yaw moment of inertia of whole mass of 2nd semitrailer = 439992 kgm^2
16. Height of roll center of tractor sprung mass, measured upwards from ground = 0.5315 m
17. Height of roll center of first semitrailer sprung mass, measured upwards from ground = 0.7050 m
18. Height of roll center of 2nd semitrailer sprung mass, measured upwards from ground = 0.7050 m
19. Height of CG of tractor sprung mass, measured upwards from ground = 1.019 m
20. Height of CG of first semitrailer sprung mass, measured upwards from ground = 1.22 m
21. Height of CG of 2nd semitrailer sprung mass, measured upwards from ground = 1.22 m
22. Height of coupling point on first semitrailer, measured upwards from ground = 1.1 m
23. Height of coupling point on tractor, measured upwards from ground = 1.1 m
24. Height of coupling point on second semitrailer, measured upwards from ground = 1.1 m
25. Roll stiffness of front suspension of tractor adjusted with tire vertical stiffness = 1145900 Nm/rad
26. Roll stiffness of rear suspension of tractor adjusted with tire vertical stiffness = 859440 Nm/rad

27. Roll stiffness of rear suspension of first semitrailer adjusted with tire vertical stiffness = 859440 Nm/rad
28. Roll stiffness of rear suspension of second semitrailer adjusted with tire vertical stiffness = 1718900 Nm/rad
29. Roll stiffness of coupling point of tractor and first semitrailer = 154700 Nm/rad
30. Roll stiffness of coupling point of tractor and second semitrailer = 154700 Nm/rad
31. Roll damping of front suspension of tractor = 6000 Nms/rad
32. Roll damping of rear suspension of tractor = 6000 Nms/rad
33. Roll damping of rear suspension of lead semitrailer = 8000 Nms/rad
34. Roll damping of rear suspension of 2nd semitrailer = 9000 Nms/rad
35. Tire roll stiffness of front axle of tractor = 8000000 Nm/rad
36. Tire roll stiffness of rear axle set of tractor = 1000000 Nm/rad
37. Tire roll stiffness of rear axle set of lead semitrailer = 6000000 Nm/rad
38. Tire roll stiffness of rear axle set of 2nd semitrailer = 5000000 Nm/rad
39. Cornering coefficient of tractor front axle = - 451200 N/rad
40. Cornering coefficient of tractor rear axle set = - 728000 N/rad
41. Cornering coefficient of lead semitrailer rear axle set = - 1380000 N/rad
42. Cornering coefficient of 2nd semitrailer rear axle set = - 1260000 N/rad
43. Distance between tractor sprung mass CG and front axle = 1.384 m
44. Distance between tractor sprung mass CG and rear axle set = 3.616 m
45. Distance between each axle of rear axle set of tractor = 1.27 m
46. Distance between each axle of rear axle set of lead semitrailer = 1.270 m

47. Distance between each axle of rear axle set of 2nd semitrailer = 1.270 m
48. Distance between 1st articulation joint of lead semitrailer and sprung mass CG = 6.385 m
49. Distance between sprung mass CG and rear axle set of lead semitrailer = 5.1150 m
50. Distance between 2nd articulation joint of vehicle (articulation joint of 2nd semitrailer) and sprung mass CG of 2nd semitrailer = 6.385 m
51. Distance between sprung mass CG and rear axle set of 2nd semitrailer = 5.1150 m
52. Distance between the whole mass CG of tractor and coupling point = 4.2510 m
53. Distance between the whole mass CG of lead semitrailer and first coupling point = 6.385 m
54. Distance between the whole mass CG of lead semitrailer and second coupling point = 6.1850 m
55. Distance between the whole mass CG of 2nd semitrailer and coupling point = 6.385 m